MULTISCALE MECHANICS MODELING OF THE EFFECT OF INTERFACE TOPOGRAPHY BETWEEN THE FIBER AND MATRIX

by

Michael A. Minnicino II

A dissertation submitted to the Faculty of the University of Delaware in partial fulfillment of the requirements for the degree of Doctor of Philosophy in Mechanical Engineering

Fall 2015

MULTISCALE MECHANICS MODELING OF THE EFFECT OF INTERFACE TOPOGRAPHY BETWEEN THE FIBER AND MATRIX

by

Michael A. Minnicino II

Approved: _____
Suresh G. Advani, Ph.D.
Chair of the Department of Mechanical Engineering

Approved: _____
Babatunde A. Ogunnaike, Ph.D.
Dean of the College of Engineering

Approved: _____
Ann L. Ardis, Ph.D.
Interim Vice Provost for Graduate and Professional Education

I certify that I have read this dissertation and that in my opinion it meets the academic and professional standard required by the University as a dissertation for the degree of Doctor of Philosophy.

Signed: _____

Michael H. Santare, Ph.D.
Professor in charge of dissertation

I certify that I have read this dissertation and that in my opinion it meets the academic and professional standard required by the University as a dissertation for the degree of Doctor of Philosophy.

Signed: _____

Travis A. Bogetti, Ph.D.
Member of dissertation committee

I certify that I have read this dissertation and that in my opinion it meets the academic and professional standard required by the University as a dissertation for the degree of Doctor of Philosophy.

Signed: _____

David L. Burris, Ph.D.
Member of dissertation committee

I certify that I have read this dissertation and that in my opinion it meets the academic and professional standard required by the University as a dissertation for the degree of Doctor of Philosophy.

Signed: _____

Peter B. Monk, Ph.D.
Member of dissertation committee

ACKNOWLEDGMENTS

This degree has only been possible with the support of my friends and family and the guidance of my committee members. I gratefully thank my advisor Dr. Michael Santare for his guidance, flexibility, and seemingly infinite patience during my completion of this degree. I also thank my committee for their guidance and feedback. I sincerely thank my work colleagues for their continuous support and mentorship over the years. Lastly, I thank my wife, Lori, for her emotional support, patience, and love which gave me the strength to finish this challenge. I thank my parents for their faith in me and support of my pursuit of this dream.

TABLE OF CONTENTS

LIST OF TABLES

LIST OF FIGURES

ABSTRACT

Recent experimental efforts using glass fiber/epoxy microdroplet test specimens have shown that increased fiber surface roughness can simultaneously increase strength and energy absorption, i.e. material toughness, through mechanical interlocking. This research employs finite element (FE) modeling techniques to investigate the effect of fiber topography on the structural response of the microdroplet test. The characteristic length of the fiber topography is on the order of nanometers and the characteristic length of the microdroplet specimen is on the order of micrometers. Consequently, a multiscale numerical method is constructed to translate the effective nanoscale structural behavior to the microscale in order to simulate its effect on the microdroplet test. These numerical techniques are validated by comparing the simulated responses to published experimental data.

The multiscale translation process effectively maps the nanoscale modeling results into a set of cohesive contact parameters that control the progressive failure of the fiber-droplet interface during the microdroplet simulation. The nanoscale simulations show that the both the interphase thickness and elastic modulus have a notable effect on the effective microdroplet structural behavior. In the presence of increased surface roughness fibers, the shear strength and toughness is increased only when the characteristic protrusion length of the fiber topography is greater than the interphase

thickness. Comparison of the microdroplet simulation results with experimental data indicates that that the multiscale translation process shows good performance up to peak load, which is often the primary metric used to rate structural performance. However, the multiscale process is less accurate in predicting the post-failure response because the nanoscale model does not accurately simulate failure of the interphase.

Chapter 1

INTRODUCTION

1.1 Motivation and Research Objectives

The structural performance of fiber-reinforced composites (FRC) is influenced by the load transfer efficiency between the matrix and its fiber reinforcement. A key component of this load transfer is the interphase, a finite thickness material region at the fiber-matrix interface that has elastic properties that are distinct from the fiber and bulk matrix and it arises due to fiber sizing, coupling agents and chemical reaction gradients between the fiber and matrix during fabrication [1-4]. The interphase thickness can vary from 100-1000 nm depending on the specific chemistry, materials and processing conditions [5-6].

Structural characterization of the interphase is often given in terms of the effective adhesion and is typically quantified by the interfacial shear strength (IFSS), which is therefore considered one of the most important parameters used to evaluate FRC interfaces. The IFSS can be influenced by selective combination of the fiber, matrix, fiber sizing, fiber surface modification, and processing [7-9]. Characterization of the load transfer behavior between these constituents is desirable for many reasons including for the purpose of selecting appropriate fiber sizings and other fiber treatments to tailor

the IFSS and fracture toughness and thereby optimize the composite's structural performance [7-12].

Realizing the importance of the bonding between the fiber and the matrix, researchers have developed many test methods that at least qualitatively and at best quantitatively assess the fiber-matrix bond strength. A conceptually simple and potentially useful method is the microdroplet test where a single, cured resin droplet is sheared from a fiber using a set of opposing blades, i.e. a microvise, resulting in a load-displacement curve which is used to assess the interfacial load transfer [4, 13-17]. A schematic of the microdroplet test setup, with important dimensions labeled, is shown in Fig. 1.1(a) and a representative load-displacement curve (F-δ curve) obtained from the microdroplet test is shown in Fig. 1.1(b). The typical curve has three distinct regions: undamaged, damaged, and failed. The slope of the curve in the undamaged region is nearly constant for systems comprised of linear elastic materials. The curve begins to diverge from its initial linear trend at the "debond force" F_d, which marks the end of the undamaged region and the beginning of the damaged region of the F-δ curve. The debond force marks the initiation of crack development. The load continues to increase beyond F_d, as does the crack length and damage until the maximum load F_{max} is achieved. At load F_{max}, the fiber completely debonds from the matrix causing the measured force to fall to F_f, which corresponds to the frictional pull-out force.

Most research has focused on tailoring interphase adhesion by controlling the degree of chemical bonding between the fiber and matrix. The IFSS has been shown to increase by as much as 40% through modified chemical surface bonding [18-20].

Although increased IFSS is desirable for applications that require superior strength, increased IFSS typically results in reduced fracture toughness. The tradeoff between IFSS and fracture toughness for fiber reinforced composites through modification of chemical bonding between the fiber, matrix, and the resulting interphase is well known [21-24]. Because of this performance tradeoff, material fabricators have sought an approach that enables simultaneous increases in both IFSS and fracture toughness; or better yet to be able to control the IFSS and fracture toughness independently. Toward this goal, composite materials researchers looked to other material systems and fields for inspiration and found rebar reinforced concrete. The surface roughness of the rebar (topography) when encased in concrete provides a mechanical interlocked interface which greatly improves both the pull-out strength (which is correlated to the IFSS) and energy absorption through frictional sliding. The researchers realized that mechanical

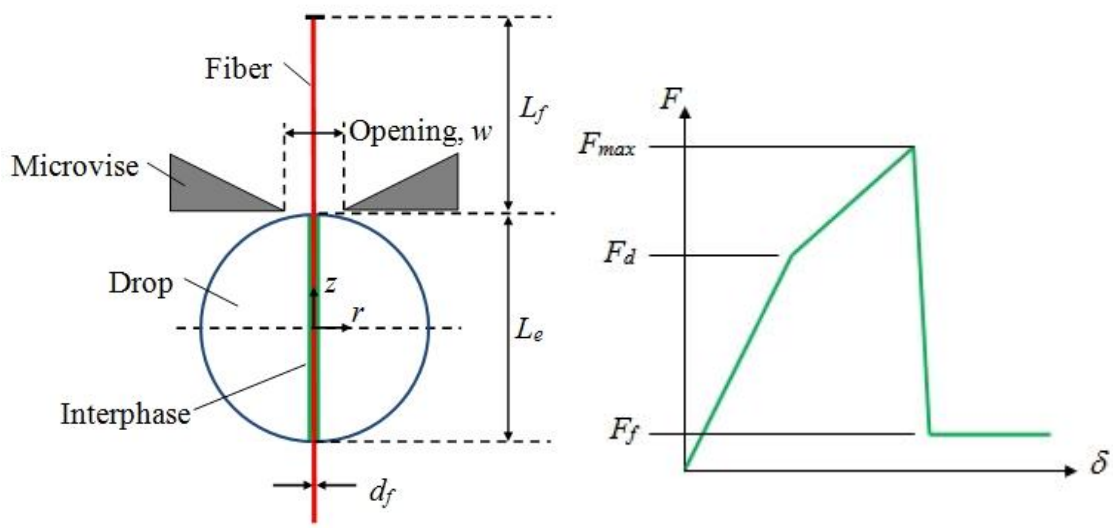

(a) (b)

Fig. 1.1. Microdroplet test (a) setup and (b) generic force-displacement response.

interlocking had the potential to increase the frictional sliding energy absorption while preserving the IFSS resulting from chemical bonding. The experimental results of Gao et al. [10-12] showed that mechanical interlocking increased the IFSS and the specific debond energy absorption, as shown in Fig. 1.2, in addition to increasing the energy dissipated by frictional sliding.

The research of Jensen and McKnight [9] and Gao et al. [10-12] are the primary efforts that experimentally explore the effect of increased surface roughness in glass fiber reinforced epoxy composites. Jensen and McKnight increased the surface roughness of glass fibers using fiber sizings consisting of blends of epoxy-compatible (GPS) and epoxy-incompatible (PTMO) coupling agents of different chemical structure and reaction activity to induce phase separation and *in situ* texture formation on the fiber. A coupling agent is compatible with the matrix if it forms a strong covalent bond with the matrix; an incompatible coupling agent does not form a covalent bond with the matrix. Additionally, silica nanoparticles were incorporated into the fiber sizing as a method to increase the fiber surface roughness. These fiber sizings were applied to rovings, i.e. a bundled group ($\sim 10^3$-10^4) of individual fibers, that were subsequently processed to fabricate pultruded composite rods that were used to make specimens for short beam shear testing and tensile testing. Additionally, these fiber sizings were applied to rovings that were woven into fabrics and made into composite plates for flexural strength testing and drop tower (impact) testing. The macroscale testing revealed that the increased fiber surface roughness composite material produced concurrent increases in IFSS and fracture toughness.

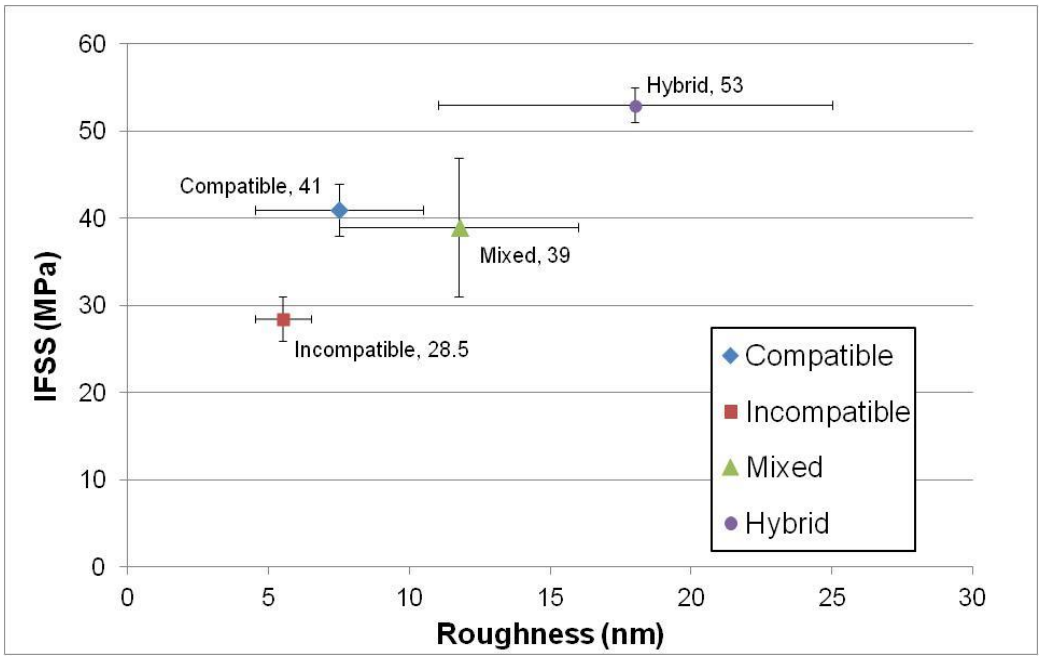

(a)

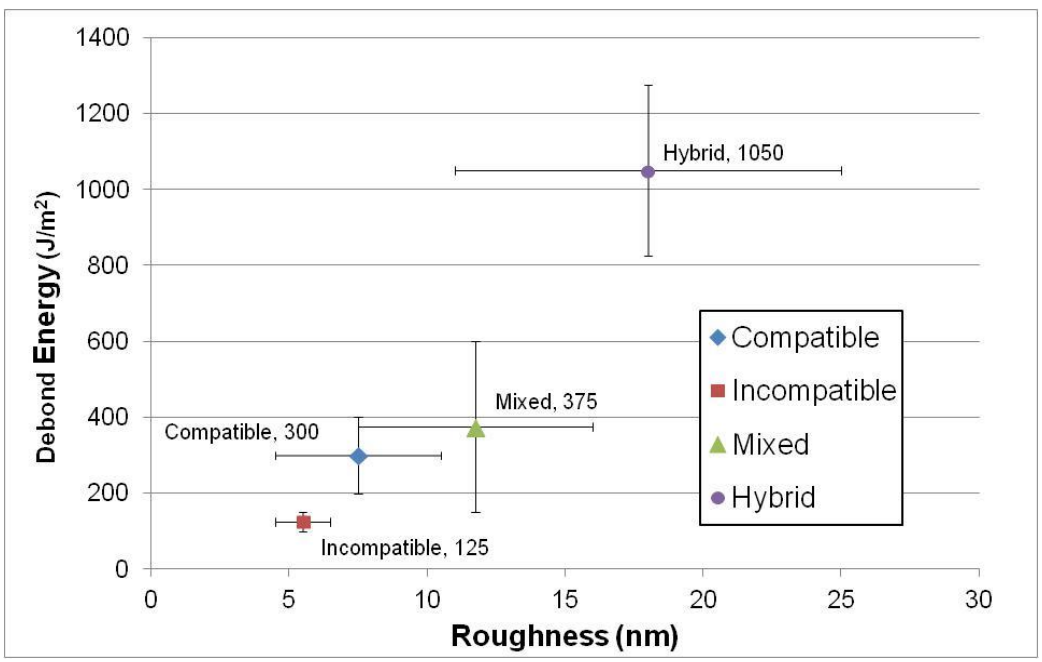

(b)

Fig.1.2. IFSS and specific debond energy as a function of fiber surface roughness reported in [11].

Gao et al. [10-12] also used two different methods to produce increased surface roughness fibers. The first method [10, 12] is the same used by Jensen and McKnight [9] where the increased fiber sizing roughness is created by blending silane coupling agents, in this case GPS and TEOS, both of which are epoxy-compatible, but have different chemical structure and reaction activity to induce phase separation and *in situ* texture formation on the fiber surface while also being compatible to both the fiber and matrix. The TEOS is chosen to induce phase separation due to its rapid condensation rate and as a silica precursor, it has the potential when mixed with GPS to precipitate silica-rich particulates that create texture. These blended sizings produced greatly increased fiber surface roughness values compared to the conventionally GPS sized glass fibers (GT11 mean fiber surface roughness is six times larger than the GPS mean surface roughness). These increased surface roughness fibers were used to create microdroplet specimens and microdroplet testing determined that, generally, the increased fiber surface roughness results in increased IFSS and fracture toughness. The exception being the low IFSS and fracture toughness of GT13 fiber sizing which is believed to be due to its interphase being relatively more stiff and brittle due to the increased number of functional groups of TEOS compared to GPS, i.e. the greater number of functional groups results in greater cross-linking which produces a more rigid interphase.

The second method used by Gao et al. [11-12] was also explored by Jensen and McKnight [9] and isolates the effect of surface roughness and chemical bonding by evaluating the microdroplet response of different custom fiber sizings. The four fiber sizings considered in that investigation included compatible GPS, incompatible PTMO,

mixed GPS-PTMO, and embedding colloidal silica nanoparticles into mixed GPS-PTMO fiber sizings. Microdroplet testing determined that the chemical bonds formed with compatible fiber sizings increase the IFSS while the increased fiber surface roughness increases the energy absorption, particularly the fiber pull-out energy. Additionally, fiber sizings containing nanoparticle silica and GPS were found to outperform the conventional and custom "designed" fiber sizings in terms of IFSS and specific absorption energy, i.e. absorbed energy divided by the fiber-droplet interface area, indicating that further tailoring of these hybrid nanoparticle-compatible fiber sizings could produce custom composite structural properties where IFSS and fracture energy can be independently controlled.

The microdroplet testing data reported by Gao et al. [10-12] is the most direct evaluation of increased surface roughness fibers on structural properties available in the literature. Therefore these experimental results serve as the starting point for the current research effort to understand and predict the effect of nanoscale fiber surface roughness on the effective macroscale mechanical response of the microdroplet test using computational mechanics.

1.2 Methodology

The goal of this research is to develop a fundamental understanding of, and the ability to predict, the effect of fiber surface roughness on the IFSS and fracture energy through computational simulation. The experimental data used for simulation validation was obtained from microdroplet testing; therefore we begin this effort by studying the

mechanics of the microdroplet test. The mechanics of the microdroplet test are studied with a three dimensional (3D) structural finite element (FE) model of the test setup as shown in Fig. 1.3 as well as an axisymmetric FE model shown in Fig. 1.4. The gradual cleaving of the droplet from the fiber by the microvise during the test necessitated that the model be capable of simulating progressive damage and eventual failure of the fiber-droplet interface. Most of the microdroplet test modeling efforts reported in the literature only loaded the microdroplet specimen to initial failure, i.e. crack initiation [14-16, 25-27]. Few researchers attempted to model the progressive failure of the fiber-droplet interface; when doing so they typically employed the virtual crack closure technique, which requires an initial crack in order to propagate [14]. In this research, surface based cohesive contact is used to model the progressive failure of the fiber-droplet interface. The advantages cohesive contact has over other numerical modeling techniques include its ability to be defined in a flexible manner, its solution efficiency, and that in it, a preexisting crack is not required to propagate damage, i.e. perfect bonding can be used initially. To our knowledge, this research is the first to use cohesive based contact to model the progressive failure of the fiber-droplet interface during the microdroplet test; there have been subsequent efforts using this approach [28-29].

The structural effect of the fiber sizing surface roughness are also studied at the nanoscale by using FE models representing a segment of the fiber sizing-interphase interface that possesses the characteristic features of the fiber/sizing/interphase/matrix system. An example nanoscale interface FE model is shown in Fig. 1.5. In contrast to the microdroplet FE models of Fig. 1.3 and Fig. 1.4, the fiber sizing surface roughness and

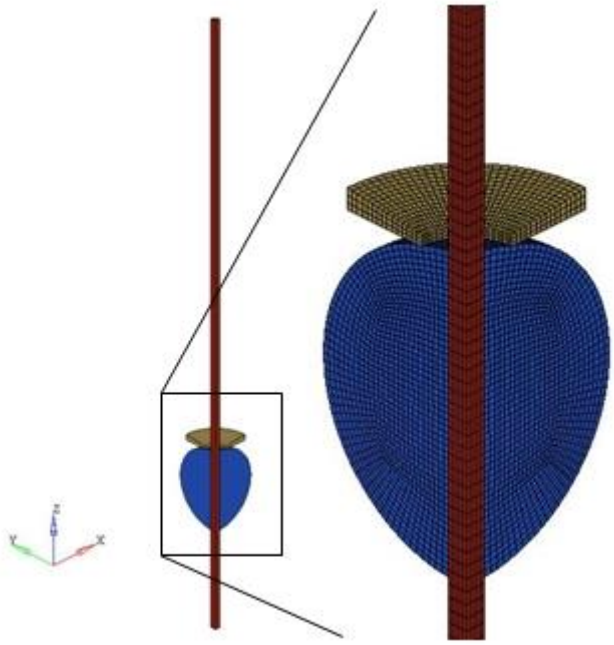

Fig. 1.3. Quarter-symmetric 3D structural FE model of the microdroplet test.

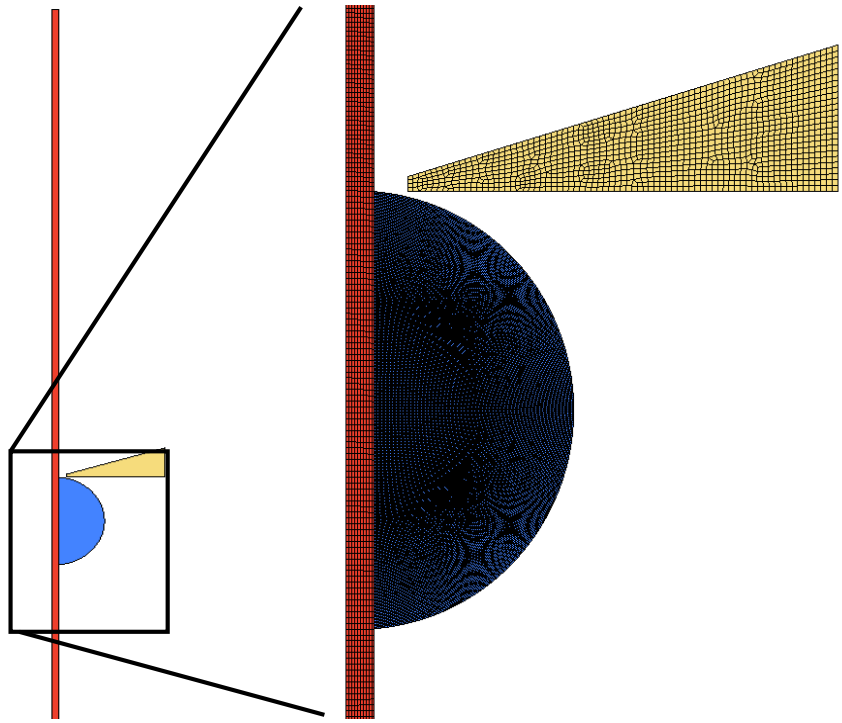

Fig. 1.4. Axisymmetric structural FE model of microdroplet test.

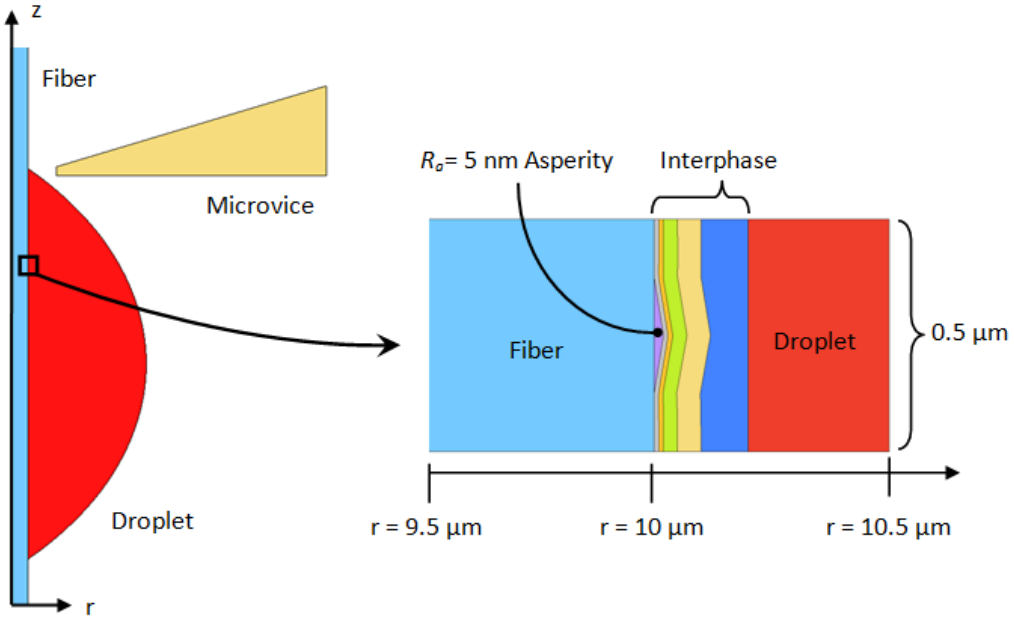

(a) (b)

Fig. 1.5. Axisymmetric (a) microdroplet FE model and (b) nanoscale interface FE model with 5 nm fiber surface roughness created using triangular asperity.

interphase are explicitly represented in the nanoscale "interface "model and therefore their structural effects can be determined mechanistically. However, the results of these nanoscale interface models are themselves not adequate for understanding the effect of fiber sizing surface roughness on the overall behavior of advanced composites. Consequently, we develop a nanoscale to microscale translation process that translates the nanoscale interface model results into the parameters used to define the cohesive contact behavior used in the microdroplet FE model. The multiscale translation process provides a bridge between the nanoscale fiber sizing surface roughness and its effect on the microdroplet force-displacement response.

Experimental data needed for simulation validation and verification is limited or is reported in a summarized manner in the literature making it less useful than it would be in its raw form, i.e. raw force-displacement response. However, the simulations presented here lay the essential groundwork for continued research in textured fiber/sizings for advanced structural composite materials.

1.3 Dissertation Outline

This dissertation is divided into six chapters and is organized as follows:

Chapter 1 describes the motivation for this work and defines the objective of this research. The methodology used in this effort is presented and the unique contributions of the research are discussed.

Chapter 2 is the literature review which begins with a short discussion of the fiber sizing and interphase components and their structural effects on fiber reinforced composites. This chapter also reviews single fiber testing methods commonly employed to evaluate and characterize the interphase and/or fiber sizing. Prior research in creating mechanical interlocking and structural characterization thereof, in composite materials is also presented. The most relevant experimental work forming the basis of this effort is reported by Gao et al. [10-12] and is reviewed in detail.

Chapter 3 reviews the mechanics of the microdroplet test using FE models. This chapter details the 3D and axisymmetric FE models created to investigate the microdroplet test. Two parametric studies are presented; the first examines the influence of test setup parameters (e.g. fiber free length, microvise opening, etc.) and specimen

material parameters (droplet elastic modulus and fiber elastic modulus) on the microdroplet force-displacement response and the second parametric study examines the influence of the cohesive parameters on the microdroplet force-displacement response.

Chapter 4 presents the nanoscale interface FE model and introduces the nanoscale-to-microscale translation process used to convert the nanoscale force-displacement results into cohesive contact parameters used to define the cohesive behavior in the microdroplet FE model.

In Chapter 5, the nanoscale-to-microscale translation process is assessed by comparing a simulated microdroplet force-displacement response to experimental data. Specifically, the microdroplet simulation uses a surface based cohesive behavior that is derived from the nanoscale interface model using the nanoscale-to-microscale translation process where the nanoscale interface model represents the average experimental fiber surface roughness.

Chapter 6 summarizes the research findings, discusses research contributions, and proposes suggestions for future work.

REFERENCES

1 Maligno AR, Warrior NA, Long AC. Effects of interphase material properties in unidirectional fibre reinforced composites. Compos Sci Technol (2010) 70:36-44.

2 Wang J, Crouch SL, and Mogilevskaya SG. Numerical modeling of the elastic behavior of fiber-reinforced composites with inhomogeneous interphases. Compos Sci Technol (2006) 66:1-18.

3 Yang F and Pitchumani R. Effects of interphase formation on the modulus and stress concentration factor of fiber-reinforced thermosetting-matrix composites. Compos Sci Technol (2004) 64:1437-1452.

4 Zhandarov S, Mader E. Characterization of fiber/matrix interface strength: applicability of different tests, approaches and parameters. Compos Sci Technol (2005) 65:149-160.

5 Jancar J. Review of the role of the interphase in the control of composite performance on micro- and nano-length scales. J Mater Sci (2008) 43:6747-6757.

6 Dharan CKH and Lin CL. Longitudinal Compressive Strength of Continuous Fiber Composites. J. Compos Mats (2007) 41(11):1389-17.

7 Moon CK. Study on the interfacial properties of three-dimensionally arranged glass fiber/epoxy resin model composites. J. Appl. Polym Sci. (2010) 116:1483-1490.

8 DiBenedetto AT. Tailoring of interphases in glass fiber reinforced polymer composites: a review. Mats Sci. and Engineering A (2007) 302:74-82.

9 Jensen RE and McKnight SH. Inorganic-organic fiber sizings for enhanced energy absorption in glass fiber-reinforced composites intended for structural applications, Compos Sci and Technol (2006) 66: 509-21.

10 Gao X, Jensen RE, Li W, Deitzel J, McKnight SH, and Gillespie Jr JW. Effect of fiber surface texture created from island blends on the strength and energy absorption of the glass fiber/epoxy interphase. J. Compos Mats (2008) 42(5):513-22.

11 Gao X, Jensen RE, McKnight SH, and Gillespie Jr JW. Effect of colloidal silica on the strength and energy absorption of glass fiber/epoxy interphases, Composites: Part A (2011) 42: 1738-47.

12 Gao X. Tailored Interphase Structure for Improved Strength and Energy Absorption, Ph.D. Dissertation, University of Delaware, 2006.

13 Pisanova E, Zhandarov S, and Mader E. How can adhesion be determined from micromechanical tests? Composites: Part A (2001) 32:425-34.

14 Liu CH and Nairn JA. Analytical and experimental methods for a fracture mechanics interpretation of the microbond test including the effects of friction and thermal stresses. Intl. J. of Adhesion & Adhesives (1999) 19:59-70.

15 Day RJ and Rodrigez JV. Investigation of the micromechanics of the microbond test. Compos Sci Technol (1998) 58:907-914.

16 Kang SK, Lee DB, Choi NS. Fiber/epoxy interfacial shear strength measured by the microdroplet test. Compos Sci Technol (2009) 69:245-251.

17 Miller B, Muri P, Rebenfeld L. A microbond method for determination of the shear strength of a fiber resin interface. Compos Sci Technol (1987) 28: 17-32.

18 Chou S and L-S Lin. Effect of colloidal silica on adhesion of glass fiber topolypropylene. Polymers & Polymer Composites (2001) 9(3): 175-183.

19 Chou S, L-S Lin, and J-T Yeh. Effect of surface treatment of glass fibers on adhesion to polypropylene resin. Polymers & Polymer Composites (2000) 8(2): 131-138.

20 Chou S, L-S Lin, and J-T. Yeh. Effect of surface treatment of glass fiber on adhesion to phenolic resin. Polymers & Polymer Composites, 1999; **7**(1); 21-31.

21 Feih S, Wei J, Kingshott P, and Sorensen BF. The influence of fibre sizing on the strength and fracture toughness of glass fibre composites. Composites Part A: Applied Science and Manufacturing (2005) 36(2): 245-255.

22 Bagwell RM and Wetherhold RC. Improvement in fracture toughness of an epoxy/copper composite through the use of various end shaped fibers.Materials Science and Engineering A (2003) 361(1-2): 294-301.

23 Piggott MR. Why interface testing by single-fibre methods can be misleading. Composites Science and Technology (1997) 57(8): 965-974.

24 Wright WW. The carbon fiber/epoxy resin interphase - A Review - Part I. Composite Polymers, (1990) 3(4): 231-257.

25 Ash JT, Cross WM, Svalstad D, Kellar JJ, and Kjerengtroen L. Finite element evaluation of the microbond test:meniscus effect, interphase region, and vise angle. Compos Sci Technol 2003; 63:641-651.

26 Park JM, Kim DS, Kong JW, Kim M., Kim W., Park IS. Interfacial adhesion and microfailure modes of electrodeposited carbon fiber/epoxy-PEI composites by microdroplet and surface wetability tests. J. Colloid and Interface Sci 2002; 249:62-77.

27 Pandey G, Kareliya CH, Singh RP. A study of the effect of experimental test parameters on data scatter in microbond testing. J Composite Materials, 2012; 46:275-284.

28 Hao Jian-wei, Zhao Yan; Luo Yun-feng, Wang Yan, and Chen Da. Experiments and finite element simulation of interfacial properties for monofilament composites. New Carbon Materials (2014) 29(3): 176-85.

29 Sockalingam S., Dey M, Gillespie Jr JW, Keefe M., Finite element analysis of the microdroplet test method using cohesive zone model of the fiber/matrix interface. Composites: Part A., 2014; 56:239-247.

Chapter 2

LITERATURE REVIEW

This chapter outlines research relevant to interphase characterization and modeling of the microdroplet test. First the concept of the interphase, its location between the fiber and the matrix, its formation, and its properties are discussed. Additionally, different methods used to characterize the interphase's mechanical properties are presented. Next, research on mechanical interlocking is briefly reviewed. Finally, the experimental work focusing on different fiber sizings for increased interphase strength and toughness provides the basis for this effort; consequently the effort detailed in [1-3] are summarized.

2.1 Fiber Sizing

A coating referred to as a "sizing" is applied to the fibers as they are manufactured [4]. The sizing serves multiple purposes including improving ease of handling, storage, and processing, as well as enhancing compatibility with the matrix resin to improve the effective mechanical strength. Glass fiber sizings are usually applied to the fiber as an aqueous emulsion with solid fractions of film former, surfactant, and a silane coupling agent [5-12]. The film former helps protect the fiber and promote wetting of the fiber by the resin matrix during processing and is typically a low molecular weight

polymer identical to or compatible with one of the resin matrix components [5, 12-13]. Many assert that the silane coupling agent is the key component in the fiber sizing as it promotes adhesion between the fiber sizing and the resin matrix [2, 5]. The silane coupling agent contains one to three alkoxy functional groups [3]. The greater the number of alkoxy functional groups the greater the ability of the silane coupling agent to react with the glass fiber as well as itself to form a multilayer network bound to the glass fiber surface [5,13]. The silane coupling agent also has a functional group on its organic tail; the functional group is usually designed to react with the matrix resin [5, 13]. Silanes that react and form covalent bonds with the matrix are termed "compatible" and those that do not react "incompatible." Plueddemann et al. [11] have studied numerous silane coupling agents in polyester and epoxy composites and reported that the chemical reactivity of the silane with the resin is a significant factor in determining the degree of coupling between the polymer and the fiber. This observation is also noted by [5, 8, 13-14].

2.2 Interphase

Generally, the interphase is a phase of material that forms between two different material systems due to chemical reaction, adsorption, diffusion, or a combination of thereof [15-18]. The interphase in reinforced polymer composites forms by the adsorption of the polymer on the surface of the inclusion in particulate filled polymer and by interdiffusion of the components in blends or by various chemical reactions on fibers [15]. The chemical reactions on the fibers are strongly influenced by the composition of

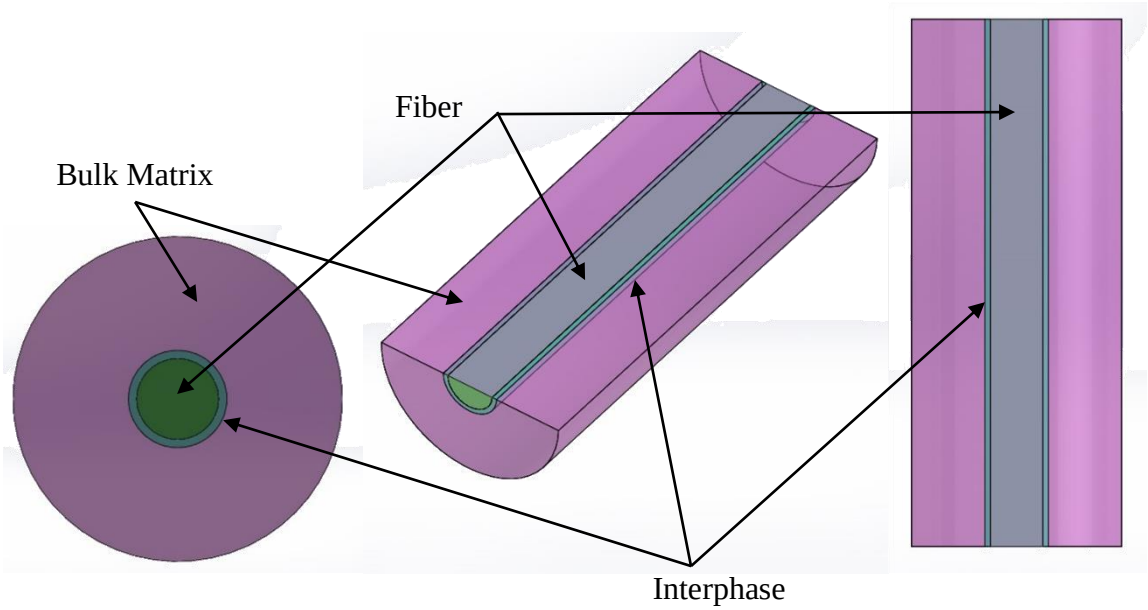

Fig. 2.1. Illustration showing the interphase disposed between the fiber and bulk matrix.

the sizing [15]. The notional interphase of a fiber-reinforce polymer is shown in Fig. 2.1. The concept of the interphase was first developed researching the failure of adhesive joints as Bikerman was the probably the first to describe the concept of an interphase as a "weak boundary layer" when describing its effect on the behavior of adhesive joints [19]. Sharpe furthered the concept of weak boundary layers as "interphases" between the adhesives and adherends in an adhesive joint [20].

Researchers have investigated different glass fiber sizings to gain further understanding of their role on the formation of interphase and overall composite mechanical properties [14]. Research has shown that wetting of the glass fiber/sizing by the resin matrix results in a fraction of the sizing dissolving into the matrix while the remainder remains bound to the glass fiber surface [5, 14]. The formation of the

interphase between a sized glass fiber and epoxy resin is explained in detail by Tanoglu et al. [5] and is summarized graphically Fig. 2.2 [5]. Additionally, it has been shown that the unbound sizing that diffuses into the matrix in the region around the fiber results in properties that are significantly different than the bulk matrix [14, 21]. Thomason [14] suggested that due to the localization of the soluble sizing around the fiber, the interphase properties are therefore primarily influenced by the soluble portion of the sizing. Using an acetone-based extraction technique to remove the unbound sizing of commercial glass fiber sizings, Thomason found that up to 75% of the sizing is soluble. Note that Thomason's implicit assumption is that the unbound sizing that is acetone soluble is equivalent to the unbound sizing that is soluble, i.e., diffusible, in the matrix. Further, Thomason showed that the soluble, i.e., unbound, portion of the sizing consisted of the surfactant (~30%) and film former (~70%) and no detectable amount of silane.

Tanoglu et al. studied the structure and properties of the interpenetrating network that forms from the bound, functionalized silane-based glass fiber sizing and the epoxy resin matrix [5]. It was found that up to 83% of the sizing may be soluble and that the soluble portion of the sizing consisted of surfactant (~19%) and film former (~81%) with no detectable silane. Additionally, they determined the composition of the bound sizing to be surfactant (~13%) and silane (~87%). These results are comparable to those of Thomason [14]. Using these findings, Tanoglu et al. developed model interphases and used dynamic mechanical analysis (DMA) to estimate the (average) interphase elastic modulus as 1.35 GPa, which is about half of the reported bulk matrix elastic modulus

(2.35 GPa). Further, the silane-phase of the interphase, i.e., the silane-rich fiber sizing, was estimated to have an effective elastic modulus of 1.35 GPa [5].

However, it should be noted that a silane-based fiber sizing is a necessary but not sufficient condition for strong adhesion strength between the fiber and matrix. This observation is emphasized by Mader and Pisanova [22] in their research of glass fiber/polypropylene microbond specimens. The microbond specimens used glass fibers with a silane-based fiber sizing and were embedded in either a neat polypropylene (PP) matrix or a modified PP (MPP) matrix. PP is a "non-polar" polymer meaning that it cannot form acid-base bonds with the fiber sizing; the MPP is designed to have polar functional groups that are able to react with the silane coupling agent and create acid-base bonds. Although all glass fibers had a silane fiber sizing, low interfacial shear stress (IFSS) was observed when embedded in the PP matrix and is attributable to the lack of strong interfacial bonding. Not surprisingly, it was found that the silane sized glass fiber/MPP systems exhibited the highest average IFSS due to the chemical reactivity between the fiber sizing and the polarized functional group in the MPP matrix. Consequently, control over the interfacial interaction is only possible if both the fiber and the matrix are compatible or modified so that they react with each other.

As stated above, the major component in the unbound portion of the fiber sizing that diffuses into the resin matrix is film former comprising 70-81% of the soluble sizing. Therefore, it should not be surprising that the resulting interphase properties are said to be significantly affected by the film former. The influence of the film former on the interphase properties was studied by Mader et al. [23] and Mader and Pisanova [24] in

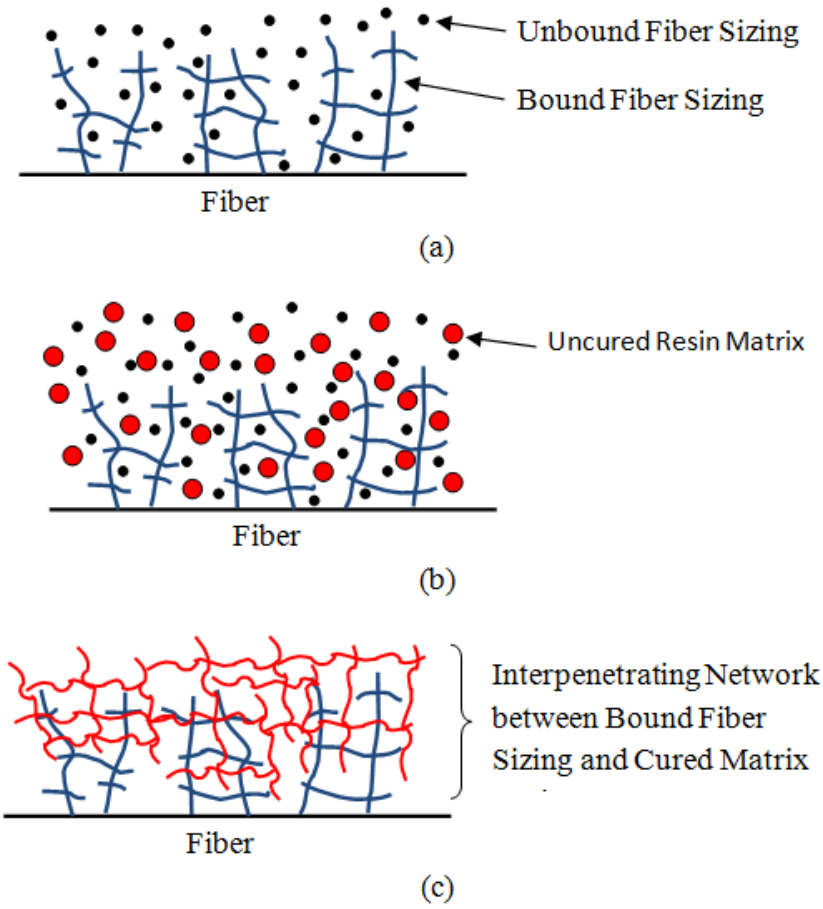

Fig. 2.2. Schematic illustrating the formation of the interphase on a (a) glass fiber with bound and unbound sizing, (b) diffusion of unbound sizing due to application of resin matrix, and (c) curing of the matrix resulting in interphase formation characterized by an interpenetrating network.

their study of glass fiber/polypropylene systems. Their fiber sizing consisted of polyurethane (PU) or PP film former and a silane coupling agent. The resin matrix was either PP or MPP, as described previously. They found that the fiber sizing with PP film former resulted in superior mechanical properties compared to both PU film former fiber sizing and silane-only fiber sizings in both PP and MPP resin matrices. It was concluded that the superior mechanical properties were the result of greater interdiffusion of the

interphase into the fiber sizing network, i.e. the interpenetrating network described by Tanoglu et al. [5]. Additionally, the fiber sizing with PP film former was reported to result in the creation of a transcrystalline interphase between the fiber and bulk matrix possessing greater stiffness and strength than the interphase formed with PU film former [25-26].

A brief overview of the existence and formation of the interphase as well as its dependence on the fiber sizing has been presented; interphase formation and evaluation of its properties is a broad and active area of research. However, in this current research, the mechanical properties of the interphase are of interest because accurate modeling of the highly textured fiber sizing requires accurate approximation of the material properties involved. The importance of interfaces and interphases is now recognized by many involved in the study of heterogeneous multiphase materials. The effect of the interphase on the properties of a multicomponent material depends on the volume fraction of the interphase and its mechanical properties [15]. This is evident in that many researchers claim the interactions between the fiber/fiber sizing and the resin matrix during fabrication determine the overall properties of the composite, others neglect these interfacial interactions and simply assume good adhesion of the phases, particularly in advanced, high performance composites [15]. It is reported that the interphase thickness in high performance composites, e.g. carbon/epoxy, is significantly smaller than in other fiber/matrix systems, e.g., glass/epoxy [29]. The argument is that the interphase volume fraction is much lower in these high performance systems and therefore has a minimal effect on the macroscale behavior. This argument leads researchers to omit the effect of

the interphase on the high performance composite properties and simply assume a strong, perfectly bonded fiber-matrix interface. However, other experimental data suggests that the presence of interphase volumes in these high performance composite systems significantly affect the longitudinal compressive strength of continuous fiber composites and should not be ignored [33].

Pukanszky claims that the properties of the interphase are still under debate because some researchers claim a compliant interphase is formed and others claim a stiff interphase [15]. The presence of a more compliant interphase between the fiber and the matrix has been established by several researchers [5, 19, 26, 30-32]. The reality may be that the interphase may either be stiff or compliant; the degree of which is dependent on the interactions between the fiber, fiber sizing, matrix, and processing. Further, the developed interphase models tend to assume an interphase of uniform thickness and homogeneous properties [18, 30, 33-35]. Some interphase models with uniform thickness were developed with varying mechanical properties as a function of distance from the reinforcement-interphase interface based on experimental data that indicated that near the fiber surface, the interphase elastic modulus is greater than the matrix elastic modulus and it decreases asymptotically to the matrix elastic modulus as a function of distance from the fiber surface [25, 13, 36]. A few of the possible variations in elastic modulus with distance from the fiber surface are shown conceptually in Fig. 2.3. The effects of the continuously varying or average interphase properties, need to be accounted for during the estimation of the overall mechanical properties of the composite. The difficulty in determining the significance of the interphase is due to the fact that the type,

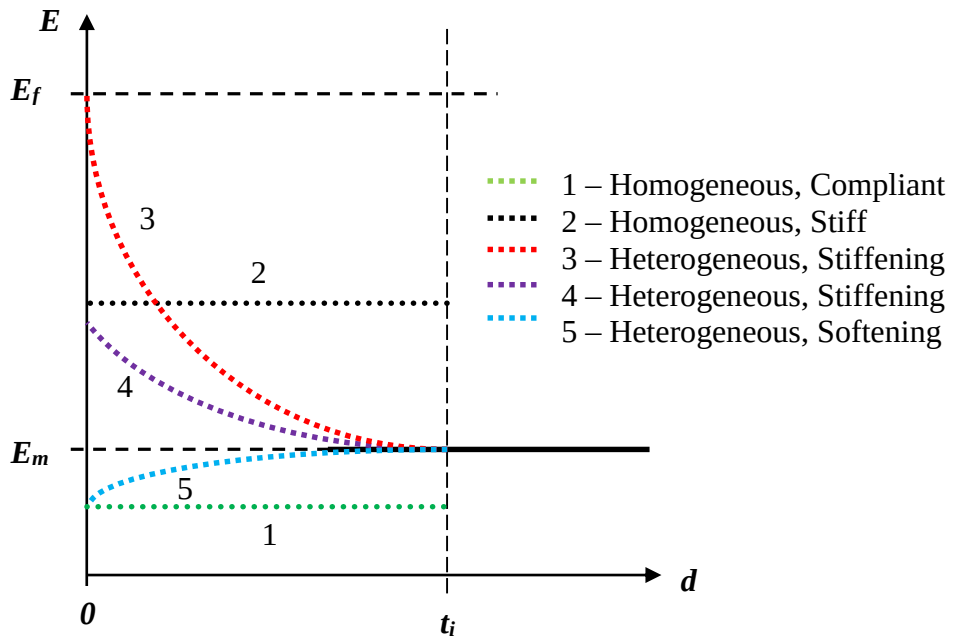

Fig. 2.3. Illustration showing proposed interphase elastic modulus variation over its thickness t_i as a function of distance from fiber surface ($d=0$).

mechanism, and strength of the interaction between the phases varies with the range of component materials, surface treatment, and processing [15].

As an example of the influence of the interphase on the macrocomposite behavior, consider the unidirectional composite microbuckling model developed by Dharan and Lin [33] where they incorporate both the thickness and mechanical properties of the interphase to develop their "three-phase" (fiber, matrix, interphase) buckling model and compare their model predictions to both experimental data and the classical microbuckling model developed by Dow and Rosen [37] to estimate the compressive strength of continuous fiber reinforced composites. The Dow and Rosen model treats the fiber as a beam on an elastic foundation, the matrix, and predicts the strength of the composite material dependent only on the matrix modulus, independent of the fiber

properties for fiber volume fractions greater than 40%. Consequently, all composites with the same matrix and fiber volume fraction are predicted to have the same compressive strength using the Dow and Rosen model. The Dow and Rosen model also significantly overestimates the compressive strength. Dharan and Lin's improved three phase microbuckling model includes the effect of the interphase. Through comparison of their model's prediction with published experimental data, Dharan and Lin's model demonstrated that the interphase plays a significant role in the compressive strength continuous fiber reinforced composites. The interphase thicknesses used in their study were estimated to be 100-250 nm for high strength carbon fiber/epoxy and 100-200 nm for glass fiber/epoxy. Additionally, using a value of 25 as the estimated ratio of the interphase shear modulus to the matrix shear modulus as determined by a FE simulated fiber pullout test by Tsai et al. [38], Dharan and Lin were able to fit their model's prediction of compressive strength due to fiber microbuckling depends on the moduli ratio between of the interphase and the matrix as well as the interphase and fiber volume fraction.

2.3 Testing Methods Used to Characterize the Interphase

The characterization of the interphase is achieved through various mechanical testing methods. The mechanical testing methods are classically grouped into two categories: macromechanical and micromechanical. Macromechanical tests assess the effective properties of the composite material and therefore the characterization of the interphase due to these tests are difficult, and perhaps more importantly, indirect.

Micromechanical tests often characterize a single fiber/matrix system and therefore offer a more direct process of characterizing the interphase. These single fiber/matrix systems may not accurately characterize real composite systems due to their low fiber volume fraction; consequently, the single fiber/matrix specimen is often termed a model test system [39]. Other micromechanical tests may be used on either model systems or specimens made from macrocomposites; the later tests measure in-situ composite properties. Micromechanical tests may evaluate the mechanical behavior at the nanoscale using nanoindentation and atomic force microscopes [26, 40-41]. The potential drawback of micromechanical test methods is that the trends observed may not translate to the macromechanical tests. Several micromechanical tests have been developed to measure the interphase properties and each one has its advantages and disadvantages. The most commonly used micromechanical tests are summarized below. The different micromechanical tests produce results that do not correlate with one test method to the other and is believed to be a consequence of the differences in the specimen geometries, loading conditions, and developed stress states between the test methods. Consequently, the characterization of the interphase cannot be compared directly [39].

2.3.1 Single Fiber Fragmentation Test

The single fiber fragmentation test was developed by Kelly and Tyson [42] and is used to characterize the IFSS of the fiber-matrix system. Typically, a single fiber is positioned along the centerline of a dogbone-shaped tensile specimen comprised of the matrix and subsequently cured. The single fiber fragmentation specimen is shown in Fig.

2.4. As the post-cured specimen is loaded, the tensile load is transferred to the fiber through shear traction at the fiber/matrix interface. The tensile load in the fiber progressively increases up to the fiber critical stress, at which point the fiber fractures. Progression of the test results in increasing load in the fractured fiber segments until these segments in turn fracture. The process continues until the fiber segment lengths are small enough so that the shear transferred along their length cannot cause fracture. The maximum fiber segment length is called the critical length and is used to calculate the IFSS. The nature of this test requires that the matrix possess significantly higher strain to failure than the fiber. Additionally, this test method requires the accurate measurement of the critical fiber fragment length and the estimation of the critical fiber stress, which is usually obtained through linear extrapolation of the experimental data of single-fiber extrapolation tests at longer gage length [39, 43]. The critical fiber stress may also be estimated using statistical methods commonly using the Weibull distribution; in this case the total number of fragments needs to be counted rather than measuring the critical fragment length. However, this statistical method requires estimation of the Weibull scale and shape parameters. Lastly, the properties of glass fibers are known to be affected by the applied fiber sizing [43]; therefore different in-situ fiber sizings may yield different in-situ critical fiber stresses during the fiber fragmentation test.

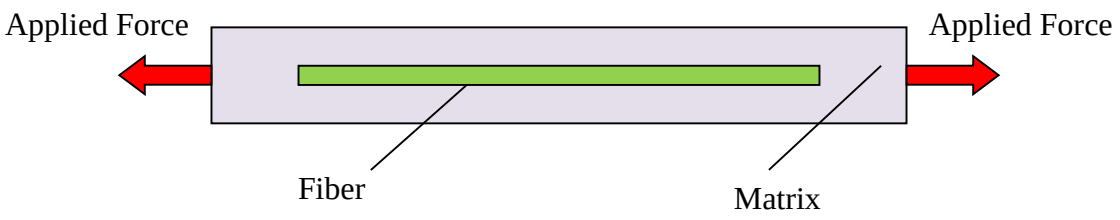

Fig. 2.4. Notional single fiber fragmentation test specimen

2.3.2 Fiber Push-Out Test

The fiber push-out test was used initially to characterize the strength of the interphase [39, 44] but has since been used to characterize other mechanical interphase properties such as energy absorption during fiber push-out [40-41]. In the fiber push-out test, single fibers perpendicular to a cut and polished surface are loaded and pushed out of the matrix as shown in Fig. 2.5. During the test, the displacement and load of an indenter tip is measured as it pushes a fiber. This test method can be used to characterize model and high volume fraction composites, i.e., *in-situ* composite, and therefore has the benefit of measuring actual composites processing effects. For relatively thick specimens, the recorded data is used in combination with FE simulations to calculate the IFSS [39]. As the specimen thickness is decreased to 8-20 fiber diameters, the IFSS can reasonably be estimated from the fiber push-out data alone by assuming a constant interfacial shear stress [39-41]. Further, some researchers have

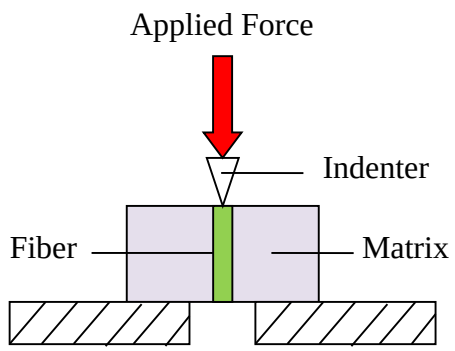

Fig. 2.5. Notional fiber push-out test specimen

adapted this test method to measure IFSS and energy absorption (energy absorption via both debonding and friction) over a range of deformation rates [40-41, 45-46]. Disadvantages of this method include fiber fracture which is commonly reported for organic fibers [39, 46], reliance on FE simulations to accurately characterize the interphase, and the introduction of defects and modified residual stress conditions at the free surface due to polishing [39].

2.3.3 Fiber Pull-Out Test

The fiber pull-out test is used to characterize the strength of the interphase. A single fiber is partially embedded in a block of matrix such that the fiber's longitudinal axis is perpendicular to the free surface of the matrix. During the test, the load and extension is recorded as the fiber is pulled from the matrix. The fiber pull-out test setup is shown in Fig. 2.6. The IFSS is calculated from the load data and the embedded fiber surface area; the embedded fiber's axial surface area omitted in this calculation. A difficulty with this test method is controlling the embedded fiber orientation and length;

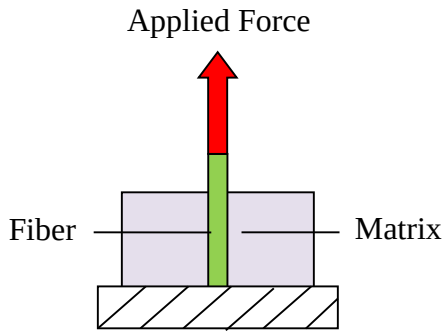

Fig. 2.6. Notional fiber pull-out test specimen

the latter of which is controlled by the fiber strength and is usually 50-100 µm [39]. Another difficulty is the dependence of the debonding force on the embedded fiber length which, depending on the fiber critical stress, may require extremely small fiber embedded lengths. By inspection of the pull-out process, another difficulty is the characterization of the energy absorption during sliding because the contact area decreases as the fiber is pulled out from the matrix.

2.3.4 Microdroplet Test

The microdroplet test is used to characterize the strength and energy absorption of the interphase and was developed by Miller [47]. The microdroplet test setup is shown in Fig. 2.7. The microdroplet is considered to be a variation of the fiber pull-out test where the embedded fiber length and orientation is controlled by controlling the size of the droplet of matrix. The microdroplet test specimen is created by forming small droplets (droplet diameter on the order of a 100-400 micron) of matrix on the fiber and curing the matrix. During the test, one of the fiber free ends of the microdroplet specimen is

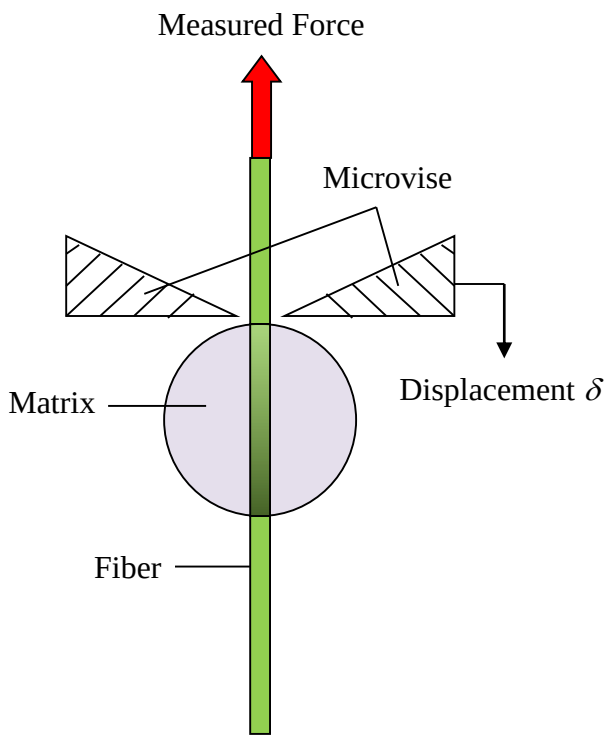

Fig. 2.7. Notional fiber microdroplet specimen.

attached to a scale for the purpose of measuring force. The droplet is positioned underneath a set of blades, also commonly called a microvise, that allow the fiber to pass through unimpeded to the scale. The microvise opening, the distance between the edges, is variable and precise control is used to manipulate the microvise opening so that the microvise edges are "close" to the fiber. The microvice translates downward at a controlled rate during the test to shear the matrix droplet from the fiber. The experimental microvise geometry is usually prismatic resulting in a non-axisymmetric stress state in the microdroplet specimen [48-51]; however, annular geometries have also been used [52-53]. Yet, the majority of modeling efforts utilize axisymmetric microvise

geometries [10, 48-49, 54-58]. Pandey et al. [54] has modeled a quarter-symmetric portion of the microdroplet test with prismatic microvise geometry and showed that the stress state is significantly dependent on the polar angle relative to the mircovise. Difficulties of this test include the formation of small enough droplets to ensure that the embedded fiber length is less than the critical length so that fiber fracture does not occur. Also, the size of the droplet determines its contact point with the microvise and therefore effectively determines the microvise opening. Varying the microvise opening is reported to result in differences in the interfacial stress profiles along the embedded fiber length and therefore produce variation in experimental data [39]. In addition to the size of the droplet, the droplet's meniscus, formed by the matrix at the point of contact with the fiber, is shown to have a significant effect on the interfacial stress profile along the length of the embedded fiber [39]. However, it has been shown that the meniscus has a decreasing effect as the droplet diameter increases [49]. The biggest advantage of this test method is that it allows for complete debonding followed by large scale sliding enabling the measurement of absorbed energy due to both debonding and frictional sliding.

2.4 Adhesion Theory and Mechanical Interlocking

The total adhesion between the fiber and the resin matrix is due the cumulative effects of chemical adhesion, physical adhesion, and mechanical adhesion. Chemical adhesion is realized when fiber sizings react with resin and form covalent bonds between the fiber sizing and the resin, i.e. the fiber sizing is compatible with the resin matrix. The

theories governing physical adhesion and its dependence on surface roughness are overviewed by Packham [59]. Packham describes fracture energy of practical adhesion, i.e. the fracture energy measured during mechanical testing, as being bi-modal since it is a function of the work of adhesion, W_a, or the work of cohesion, W_c, as well as other energy absorbing processes such as plastic deformation characterized by the function ψ [59]. The work of adhesion and work of cohesion are related to the work required to fail a material and create new surfaces and depends on the failure mode. The fracture energy of practical adhesion G is

$$G = G_0 + \psi = \begin{cases} W_a + \psi & \textit{Adhesive Failure Mode} \\ W_c + \psi & \textit{Cohesive Failure Mode} \end{cases} \tag{2.1}$$

where G_0 represents "surface excess energy per unit area." Usually $\psi >> G_0$; however, small increases in G_0 produce large increases of adhesion because G_0 and ψ are coupled [59]. It is explained that for a mechanically simple adhesive joined system, stronger bonds (increased G_0) lead to greater increases in fracture energy because they allow for more bulk energy dissipation (increased ψ) during fracture.

The surface energy term G_0 of the surface may also be expressed as

$$G_0 = \frac{\Delta G}{A}. \tag{2.2}$$

Packham states that practical adhesion can be increased by increasing ΔG which can be accomplished through surface modification of the substrate and roughening of the substrate surface. Surface modification results in the formation of stronger bonds. The roughening results in increased ΔG because atoms near an "asperity peak or a fine fractal feature will clearly have a much greater atomic surface energy than a chemically similar atom in a plane crystal surface." The area A in Eq. (2.2) refers to the nominal area; the roughened surface true area will always be greater. Greater true surface areas more likely have more atoms with higher atomic surface energy leading to even greater values of G_o [59]. Additionally, the asperities in high roughness surfaces may be able to alter the stress distribution at the interface resulting in the deformation of larger volume of material during fracture, effectively increasing ψ. Further, the strengthening of adhesion due to redistribution of the stress may result in a change of the mode of failure from a less energetic mode to a more energetic mode, i.e. adhesive to cohesive [59]. The interface strength of mechanically interlocked interfaces is termed mechanical adhesion. There are few studies that focus on the creation of mechanical interlocking between the fiber and matrix in polymer matrix composites [1-3, 7, 63]. The deliberate creation of mechanically interlocking fibers has been demonstrated using two approaches: 1) modification of the shape of the fiber free-end and 2) development of high surface roughness fibers.

2.4.1 Modification of Fiber End-Shape

Bagwell et al. [60] reported improvement in the composite material fracture toughness using short fibers with shaped-ends. The study focused on dumbbell-like short copper fibers. The shaped-ends of the short fibers effectively increased the amount of volume of matrix material involved in the plastic deformation during fiber pull-out. Bagwell et al. [60] determined that the fracture toughness of a composite material comprised of short fibers with shaped-ends can be increased by 40% for a flat-end shaped fiber compared to uniform, straight fibers. Not surprisingly, Tsai et al. [61] determined that the geometry of the fiber end-shape affects the interface strength during fiber pull-out using finite element simulations. The significant drawback to using fiber end-shapes to increase fracture toughness and interface strength is that this method is limited to short fiber reinforced composites and is not applicable to continuously reinforced fiber composites.

2.4.2 Increased Surface Roughness Fibers

Most of the published work on using surface roughness to increase the mechanical interlocking between fiber and matrix is concentrated in the rebar-concrete industry. The surface topography of the rebar is modified to achieve increased pull-out strength of the rebar from the concrete and different rebar topographies are found to significantly affect the strength [62]. Chou and Lin [63], Jensen and McKnight [7], and Gao et al. [1-3] have applied the rebar-concrete analogy to the microscale by developing fibers with large surface roughness values. Chou and Lin incorporated silica nanoparticles to glass fibers

and subsequently applied a silane sizing to the glass fiber-silica nanoparticle system. The fibers were embedded into polypropylene, a thermoplastic matrix (no reactive bonding). Macroscale testing showed a 70% increase in tensile strength of the composite material using the high roughness fibers/sizing compared to unsized, neat fibers. Jensen and McKnight mixed compatible and incompatible silane coupling agents to produce fiber surface roughness *in situ* [7]. Jensen and McKnight determined that strength and energy absorption could be increased using textured fiber surfaced fabricated from either silane blends or direct integration of silica nanoparticles into the fiber sizing. Further, Jensen and McKnight [7] found that the damaged zone was greatly influenced by the sizing; the sizing with greatest energy absorption capability limited the volume of the composite's damaged zone during drop tower impact testing. In many ways, the efforts of Jensen and McKnight [7] serve as the starting point for the research of Gao et al. [1-3]. Gao et al. investigated fiber sizings with various levels of chemical bonding and fiber texture in a systematic method to isolate the effect of chemical bonding and fiber topology on the IFSS and energy absorption using silane sizings and silica nanoparticles. The research of Gao et al. is the motivation for much of this research and will be discussed in detail in the next section.

2.5 Review of Experimental Results of Textured Fibers

This section summarizes the experimental efforts presented in [1-3]. The research detailed in [1-3] used the microdroplet test to quantify the effect of the fiber surface roughness and interphase properties using glass fibers and epoxy resin. Fiber texture is

created by one of two methods. The first method used blends of 3-glycidoxypropyltrimethoxy silane (GPS) and tetrethoxy silane (TEOS) in different ratios to produce in-situ topographic "islands" of different texture in the fiber sizing. The fiber sizing roughness was characterized using Atomic Force Microscopy (AFM). The AFM fiber sizing surface and reported (absolute) roughness for blended silanes are shown in Fig. 2.8. The blend designation used is GTXY where XY denotes the stoichiometric ratio of GPS to TEOS, e.g., GT13 is produced from a silane blend of one part GPS to three parts TEOS, and the total weight percent of coupling agents in the fiber sizing is held constant at 1%. The composition and surface roughness for these fiber sizing formulations are summarized in Table 2.1.

The second method to produce enhanced fiber surface roughness used blends of coupling agents in addition to direct integration of silica nanoparticles (Ludox TMA, 22nm diameter) in the fiber sizing formulation. However, the second route uses GPS and propyltrimethoxysilane (PTMO); this is the same fiber sizing Jensen and McKnight explored in their macrocomposite investigation [7]. GPS is compatible with the epoxy matrix and PTMO is incompatible with the epoxy matrix and was chosen to isolate the effects of chemical bonding and surface roughness in order to identify their effect on the microdroplet force-displacement response. Four fiber sizing formulations were developed including sizings containing GPS-only coupling agent (i.e. "Compatible"), PTMO-only coupling agent (i.e. "Incompatible"), both GPS and PTMO coupling agents (i.e. "Mixed"), and blended GPS-PTMO with silica nanoparticles (i.e. "Hybrid"). The hybrid sizing contained 1% (weight fraction) colloidal silica nanoparticles and was added

directly to the sizing mixture before application to the glass fiber [1, 3]. Through acetone extraction experiments, no presence of colloidal silica was detected in the soluble portion of the sizing and it was concluded that the silica nanoparticles are embedded in the sizing and are strongly bonded to the glass fiber [1, 3]. This work serves as the motivation for this current effort. The fiber sizing surfaces and reported absolute roughness values for the compatible, incompatible, mixed, and hybrid fiber sizings measured using AFM is shown in Fig. 2.9. The composition and surface roughness values are summarized in Table 2.1.

Table 2.1. Summary of fiber sizing naming, composition, and reported surface roughness

Fiber Sizing	Components	Roughening Agent	Surface Roughness Ra (nm)
USGF (ref [1,2])	none	None	5.2±1.5
GPS (ref [1,2])	1.0% wt. GPS	None	6.4±2
GT13 (ref [1,2])	1:3 molar ratio GPS:TEOS 1% total wt.	None	21.4±21
GT11 (ref [1,2])	1:1 molar ratio GPS:TEOS 1% total wt.	None	38.6±29
GT31 (ref [1,2])	3:1 molar ratio GPS:TEOS 1% total wt.	None	26.5±26
Hybrid (ref [1,3])	0.5% wt. GPS 0.5% wt. PTMO	1% Colloidal silica	18.01±6.86
Compatible (ref [1,3])	0.5% wt. GPS	None	7.89±3.49
Mixed (ref [1,3])	0.5% wt. GPS 0.5% wt. PTMO	None	11.74±3.91
Incompatible (ref [1,3])	0.5% wt. PTMO	None	5.48±1.28

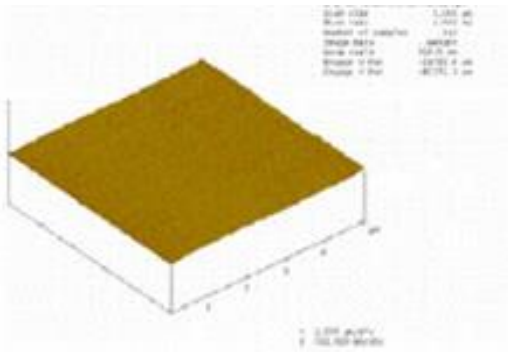

(a) Unsized (R_a = 5.2 nm)

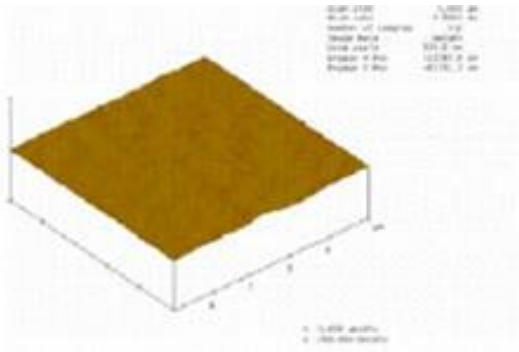

(b) 1% GPS (R_a = 6.4 nm)

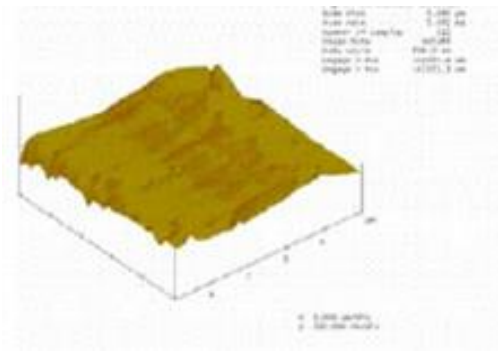

(c) 1% GT31 (R_a = 26.5 nm)

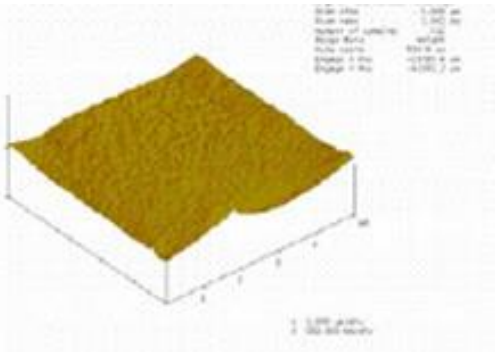

(d) 1% GT13 (R_a = 21.4 nm)

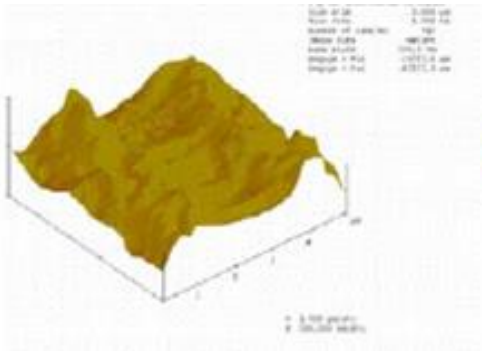

(e) 1% GT11 (R_a = 38.6 nm)

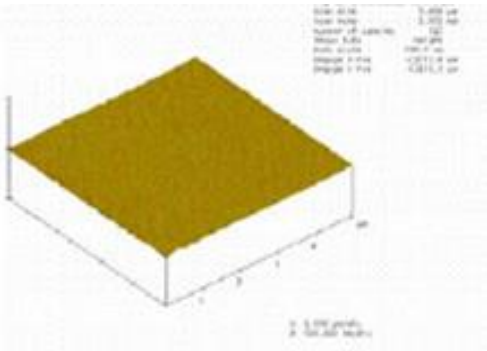

(f) 1% TEOS (R_a = 5.8 nm)

Fig. 2.8. AFM surface roughnesses of fibers sizings formed in-situ from blends of compatible silane coupling agents GPS and TEOS . Roughnesses in parenthesis are not explicitly reported and are estimated from figures. (images copied with permission [3])

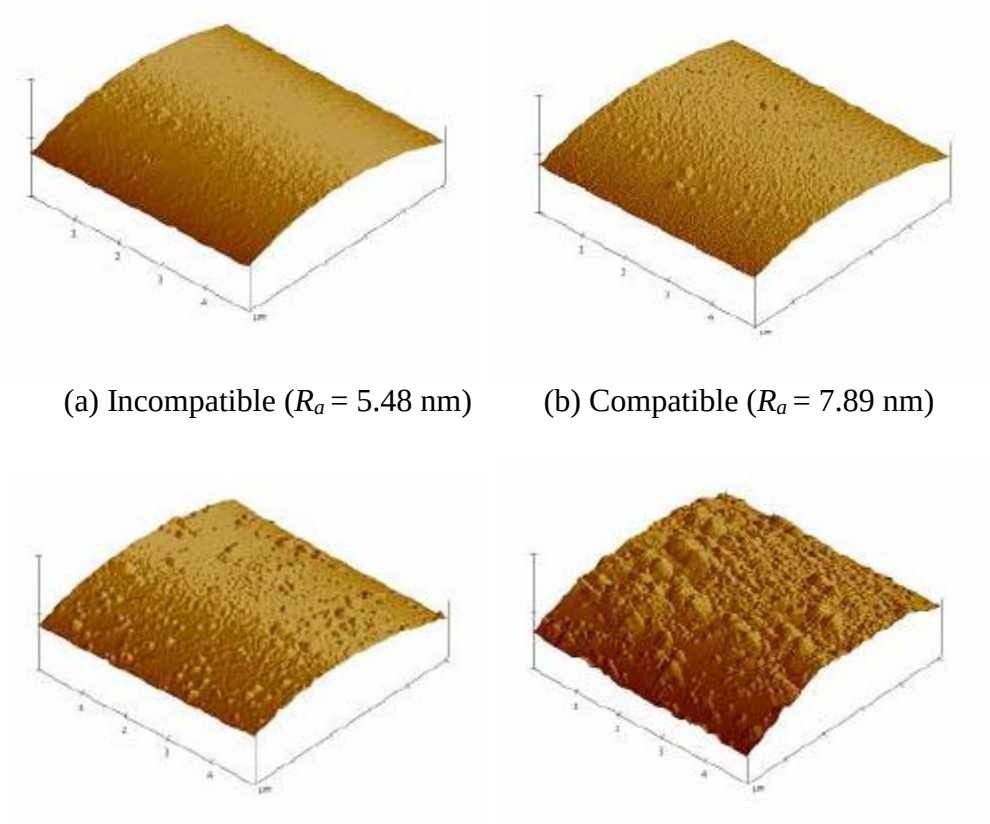

(a) Incompatible (R_a = 5.48 nm) (b) Compatible (R_a = 7.89 nm)

(c) Mixed (R_a = 11.74 nm) (d) Hybrid (R_a = 18.01 nm)

Fig. 2.9. AFM surface roughnesses of fibers sizings formed in-situ from custom fiber sizings (a) PTMO-only, (b) GPS-only, (c) GPS-PTMO, and (d) GPS-PTMO/Silica Nanoparticle (images copied with permission [3]).

2.5.1 Decomposition of Microdroplet Test Force-Displacement Curve

The microdroplet specimens are produced by applying small droplets of epoxy resin to the various fiber sizings. The microvise is positioned above the resin droplet and the microvise opening is ideally adjusted such that the blades “almost” touch the fiber [3]. The microvise moves downward at a constant velocity of 0.001 mm/sec to shear the resin droplet from the glass fiber. During the test, displacement of the microvice and the reaction force of the fiber are recorded. A typical force-displacement curve is shown in

Fig. 2.10. The force-displacement curve is commonly used to infer the interfacial shear strength (IFSS). Gao et al. [1-3] developed a data reduction method that uses the force-displacement curve to estimate the debonding energy and the energy absorbed due to frictional sliding. The reduction method requires the removal of the testing apparatus compliance in order to calculate energy quantities using the "corrected displacement" as well as the partitioning of the force-displacement curve into three non-overlapping regions. These regions are shown in Fig. 2.10 and are associated with different phenomena as described as below.

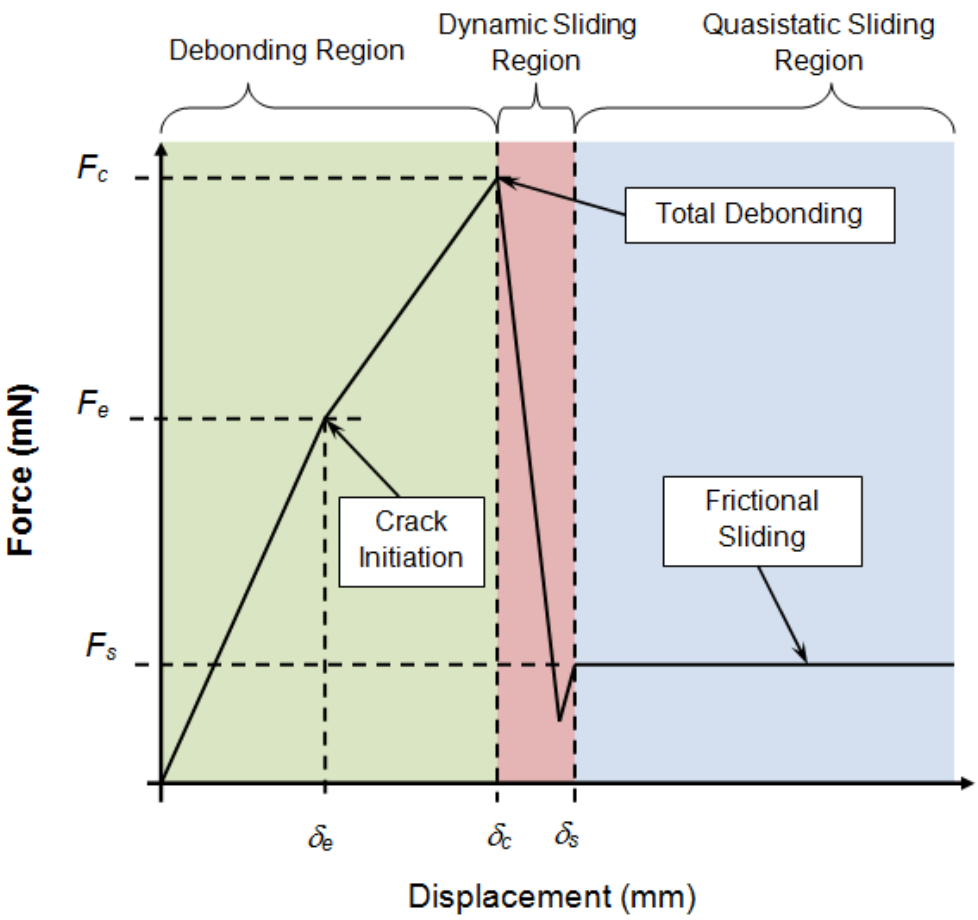

Fig. 2.10. Notional microdroplet test raw force-displacement curve with the key force values and regions identified.

Region 1- Debonding ($0 \leq \delta \leq \delta_c$)

This region of the force-corrected displacement curve contains both the elastic loading and the permanent accumulation of interfacial damage in the microdroplet test. In the beginning of this region, the load increases linearly up to the elastic limit δ_e, at which debonding begins. The linear slope is characterized by the elastic stiffness K_e. As the microvice continues to shear the microdroplet from the fiber; the load increases and debonding continues up to displacement δ_c, corresponding to the maximum load F_c, marking the point of complete debonding. Loads greater than F_e are a combination of adhesion load of the intact portion of the interface and the frictional load for the debonded portion of the interface.

Region 2 - Dynamic Sliding ($\delta_c \leq \delta \leq \delta_s$)

This region of the force-displacement curve contains the sudden load drop following the complete debonding of the droplet from the fiber. This region begins at displacement δ_c, corresponding to complete debonding of the microdroplet. The stretched fiber is elastically unloaded causing it to spring-back to its unloaded geometry. This sudden release of elastic energy causes the fiber to traverse upward through the debonded droplet, which is forced downward by the microvise. Gao asserts that the magnitude of the force in this region is determined by the magnitude of the elastic energy released and the frictional energy dissipated by the fiber when pulled through the droplet [3]. The end of this region is defined by the beginning of the plateau in the force-displacement curve exhibited by many mircrodroplet tests.

Region 3 - Quasistatic Sliding($\delta_s \leq \delta$)

This region of the force-corrected displacement curve contains the quasistatic resistance to sliding of the debonded droplet along the fiber. This beginning of the region is somewhat subjective and usually defined as the beginning of the post-failure plateau in the force-displacement curve. It is reasonable to conclude that higher degrees of fiber texture should increase the average frictional load along the sliding interface during this region.

2.5.2 Overview of Reduction Method

Gao et al. [1-3] developed the following data reduction method. The method begins by recognizing that the measured displacement, δ_{raw}, in the microdroplet test is the superposition of three individual displacements: droplet displacement δ_d, fiber stretching δ_f, and test apparatus deformation δ_m.

$$\delta_{raw} = \delta_d + \delta_f + \delta_m \tag{2.3}$$

It should be emphasized that the droplet displacement δ_d is the combined displacement of the droplet and the embedded fiber and not the displacement of the matrix due to interaction with the microvise. Accurate estimates of energy quantities for the fiber/interphase/matrix system require the displacements based on the fiber and matrix. Consequently, Gao removed the apparatus deformation by estimating the test apparatus' compliance C_m which is reported to be 0.0314± 0.0081 mm/N [2-3]. Therefore the apparatus deformation may be expressed as

$$\delta_m = C_m F \tag{2.4}$$

where F is the force magnitude. Consequently, the "corrected" displacement used by Gao is expressed as

$$\delta = \delta_d + \delta_f = \delta_{raw} - \delta_m = \delta_{raw} - C_m F \tag{2.5}$$

Note that the "corrected" displacement includes contributions from both the droplet δ_d and fiber stretching δ_f. Gao et al. [1-3] divides the force-corrected displacement curve into three regions each of which corresponds to distinct process: debonding, dynamic sliding, and quasistatic sliding. These distinct processes are used to compute the average interfacial shear strength (i.e. IFSS), debonding energy, dynamic sliding energy, and quasistatic sliding energy.

Average interfacial shear strength:

Many studies in the literature simply assume the shear stress is uniform along the fiber-droplet interface and therefore Eq. (2.6) is a reasonably accurate measure of the interfacial shear strength (IFSS) [3].

$$IFSS = \bar{\tau} = \frac{F_{peak}}{\pi d_f l_e} \tag{2.6}$$

where $\bar{\tau}$ is the IFSS, F_c is the critical load measure during the microdroplet test, d_f is the fiber diameter, and l_e is the embedded fiber length in the droplet. However, there is a stress concentration along the circumferential edges of the microdroplet resin where the fiber enters and exits the droplet. Consequently, the measured force-displacement data can only estimate the *average* interfacial shear strength via Eq. (2.6).

Absorbed energy:

Energy absorption is an important property of a composite, particularly during impact loading where fibers fail, debond, and pull-out from the matrix. The process Gao et al. [1-3] uses to calculate the energy absorbed during the debonding region is presented below.

The total work added to the microdroplet system during the debonding region is found by integrating the force-displacement curve between the limits of the region, i.e.

$$W_t = \int_0^{\delta_c} F(\delta) d\delta \,. \tag{2.7}$$

The elastic energy is computed as a function of the displacement using the method developed by Gama and Gillespie [64]. This method assumes that the slope of the unloading and reloading curve $K(\delta)$ is displacement-dependent and is bounded by K_e and K_{nl}, i.e. $K_{nl} \le K(\delta) \le K_e$, where K_{nl} is the average slope of the softened force-displacement response. The displacement-dependent stiffness is expressed as

$$\begin{aligned} K(\delta) &= K_e \quad \delta \le \delta_e \\ K(\delta) &= K_e - \alpha \frac{(\delta - \delta_e)}{\delta}(K_e - K_{nl}) \quad \delta > \delta_e \end{aligned} \tag{2.8}$$

where α is a fitting parameter [64]. This method was originally developed to calculate the elastic energy from the force-displacement data recorded during a punch shear test of a thick composite specimen [64]. The fitting parameter α=0.75 is selected based on the stiffness observed during the loading-unloading testing of a thick macroscale composite

panel (and by neglecting hysteresis). Gao et al. uses the same value for α in [1-3]. The elastic energy from the force-displacement data is calculated by

$$E_e = \frac{F(\delta)*F(\delta)}{2K(\delta)} \tag{2.9}$$

where $F(\delta)$ is the measured force and $K(\delta)$ is the displacement-dependent slope of the force-corrected displacement curve. This method is subjective due to the selection of the fitting parameter α and the average nonlinear stiffness K_{nl}.

A more robust method to estimate the elastic energy is needed. Obviously, all work put into the system up to δ_e is elastic and finite element simulations conducted in the course of this research indicate that the majority of the microdroplet stiffness results from the glass fiber stiffness (over 90% of the system stiffness, K_e). Consequently, it is reasonable to assume that the slope of the force-displacement curve during unloading is approximately the fiber stiffness K_f. Therefore, it is proposed that the elastic energy be computed using an expression having the same form as Eq. (2.9) but the displacement-dependent stiffness is approximated as the constant fiber stiffness K_f, i.e. $K(\delta) \approx K_f$. Note that the fiber stiffness is approximately constant and that it decreases slightly as fiber free length increases due to the debonded fiber-droplet interface length increasing as the microdroplet test progresses. The elastic energy for these assumptions is

$$E_e = \int_0^d F d\delta = \frac{F(d)F(d)}{2K_f}. \tag{2.10}$$

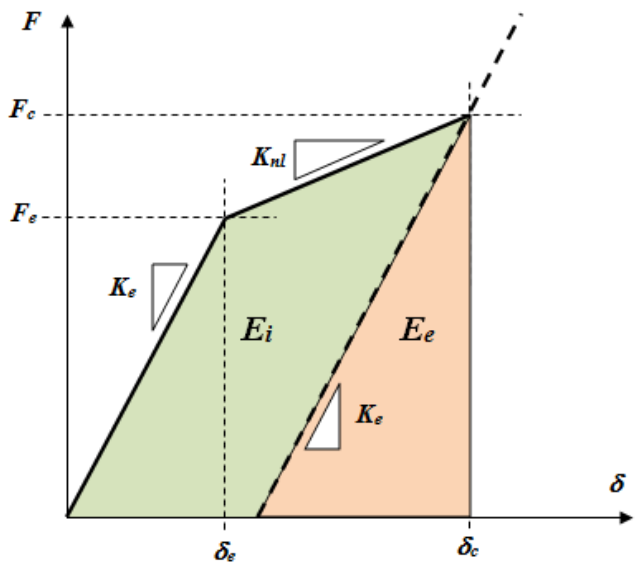

Fig. 2.11. Partitioning of the total energy into the elastic energy E_e and the absorbed energy E_i.

Finally, the energy absorbed by the interphase E_i is calculated by subtracting the elastic energy absorption E_e, calculated by (2.9) or (2.10), from the total energy E_t, i.e.

$$E_i(\delta) = E_t(\delta) - E_e(\delta). \tag{2.11}$$

The idealized partitioning of the energy for the debond region is shown in Fig. 2.11. Similarly, the dynamic sliding E_{ds} and quasistatic E_{qs} energies are the total energies for those regions. The specific energy values can be calculated on a per unit area basis as

$$E_{db}^{sp} = \frac{E_i}{A} \tag{2.12}$$

$$E_{ds}^{sp} = \frac{E_{ds}}{A(\Delta l_f + \Delta\delta)} \tag{2.13}$$

$$E_{qs}^{sp} = \frac{E_{qs}}{Al_e} \tag{2.14}$$

where $A=\pi d_f l_e$ is the surface area of the nominal fiber-droplet interface where d_f is the nominal fiber diameter, l_e is the fiber embedded length, Δl_f is the change in the fiber stretched length as the load drops from F_c to F_s in the dynamic sliding region, $\Delta\delta=\delta_s-\delta_c$ is the distance that the microvise moves during dynamic sliding, and the superscript "*sp*" denotes specific energy.

2.5.3 Summary of Results

Gao et al. [1-3] used the formulas detailed in Section 2.5.2 to assess the behavior of different fiber sizings using the microdroplet test method for a glass fiber-epoxy system. Both chemical composition and topology of the sizing was investigated to assess the IFSS and fracture toughness (measured as specific energy absorption during the debond phase of the microdroplet test) of the resulting formed interphase.

The IFSS and fracture toughness results for the blended GPS-TEOS fiber sizing formulations are shown as a function of the developed fiber surface roughness in Fig. 2.12. The standard deviation of the *in situ* developed fiber surface is considerable. However, the standard deviation of the IFSS for a given fiber sizing formulation is relative small and it can be concluded that the IFSS is a stronger function of chemical bonding than fiber surface roughness. Conversely, the standard deviation of the fracture toughness, i.e. energy absorption, is large and indicates that it is a strongly influenced by fiber surface roughness. Lastly, it is shown that both IFSS and fracture energy generally increase as fiber surface roughness increases.

Gao et al. isolated the effects of chemical bonding and texture using the custom GPS-PTMO and GPS-PTMO-Nanosilica fiber sizing systems. The experimental results indicate that the chemical bonding promotes increased IFSS while increasing texture increases the specific debonding energy compared to the unsized fiber. The experimental results show that the IFSS and fracture energy increases with increasing fiber surface roughness as shown in Fig. 2.13. The combination of chemical bonding and texture of the hybrid custom sizing enabled progressive debonding that resulted in slightly increased IFSS and significantly increased debonding energy while also absorbing more energy post failure during the sliding portion of the microdroplet test.

Lastly, Gao et al. [1-3] inspected the failed surfaces of the microdroplet tests using scanning electron microscopy (SEM) for the Compatible and Hybrid sizing sized microdroplet specimens. SEM indicated that the fiber surface roughness affects the interfacial failure process where a predominantly adhesive failure mode is noted for the low surface roughness fiber system (Compatible fiber sizing) and a predominantly cohesive failure mode is noted for the high surface roughness fiber system (Hybrid fiber sizing). Additionally, although adhesive failure is the predominant failure mode for the low surface roughness fiber (Compatible fiber sizing), cohesive failure is noted in the bulk matrix. Conversely, the cohesive failure associated with the high surface roughness fiber (Hybrid fiber sizing) is reported to be located in the interphase. It is surmised this observation is due to the presence of silica nanoparticles in the interphase dramatically increasing the fracture toughness. It is also surmised that for microdroplet specimens created using the high surface roughness fiber (Hybrid fiber sizing) that the developed

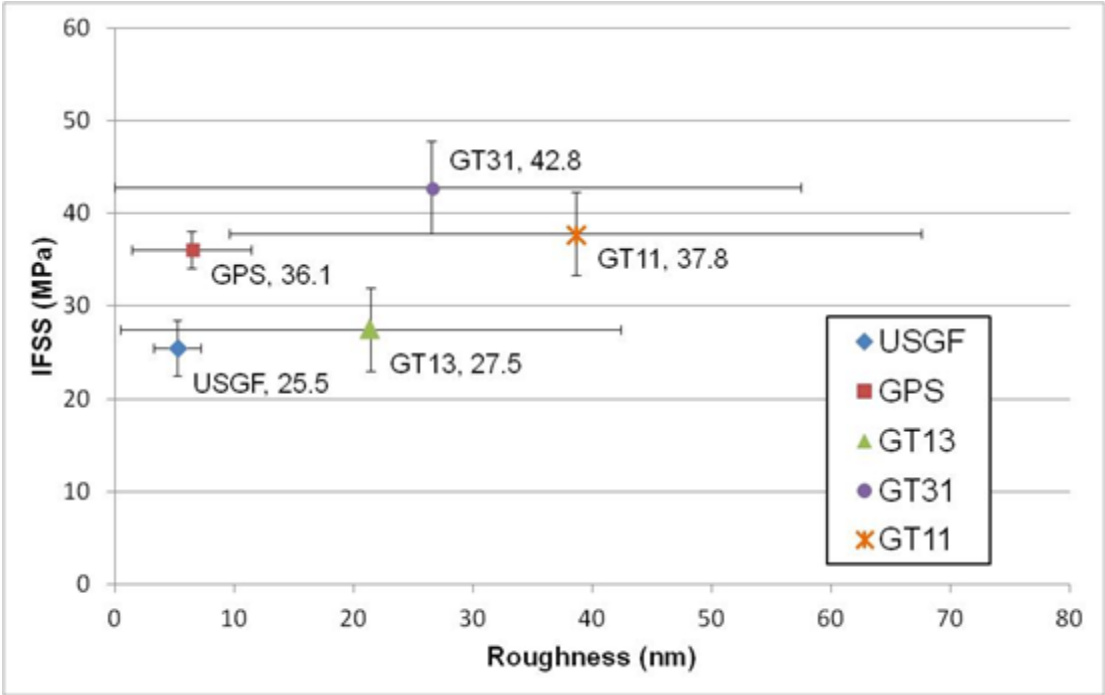

(a)

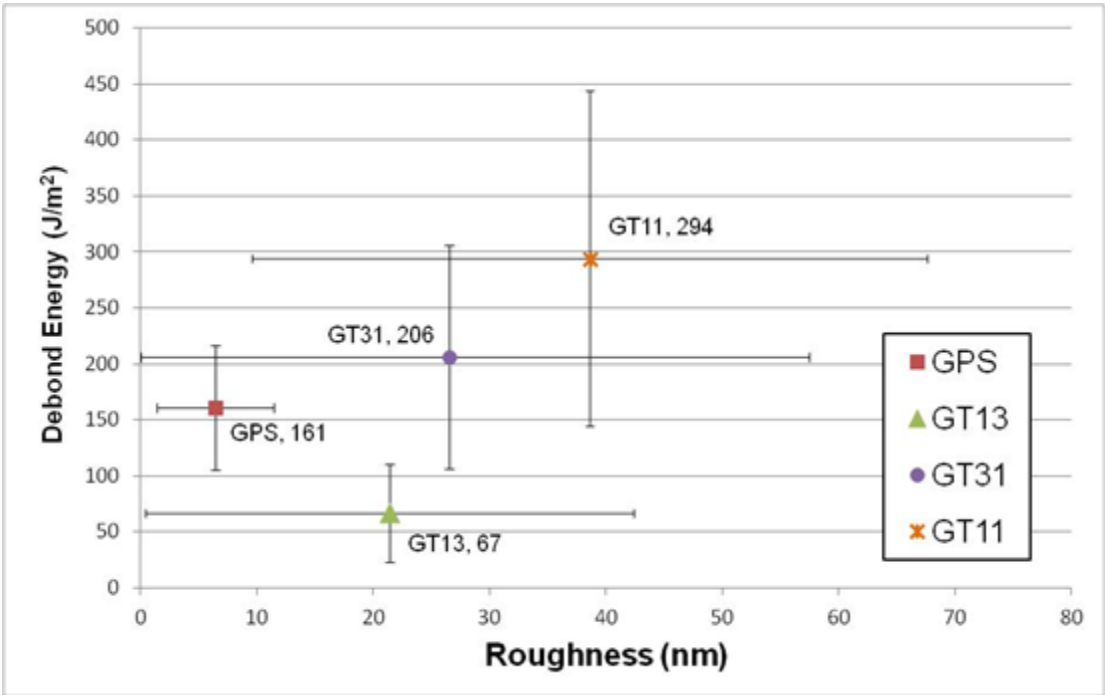

(b)

Fig. 2.12. Summary of (a) IFSS and (b) specific debonding energy results [2,3] for glass/epoxy microdroplet specimens with different fiber sizings (debond energy for unsized glass fiber (USGF) not reported).

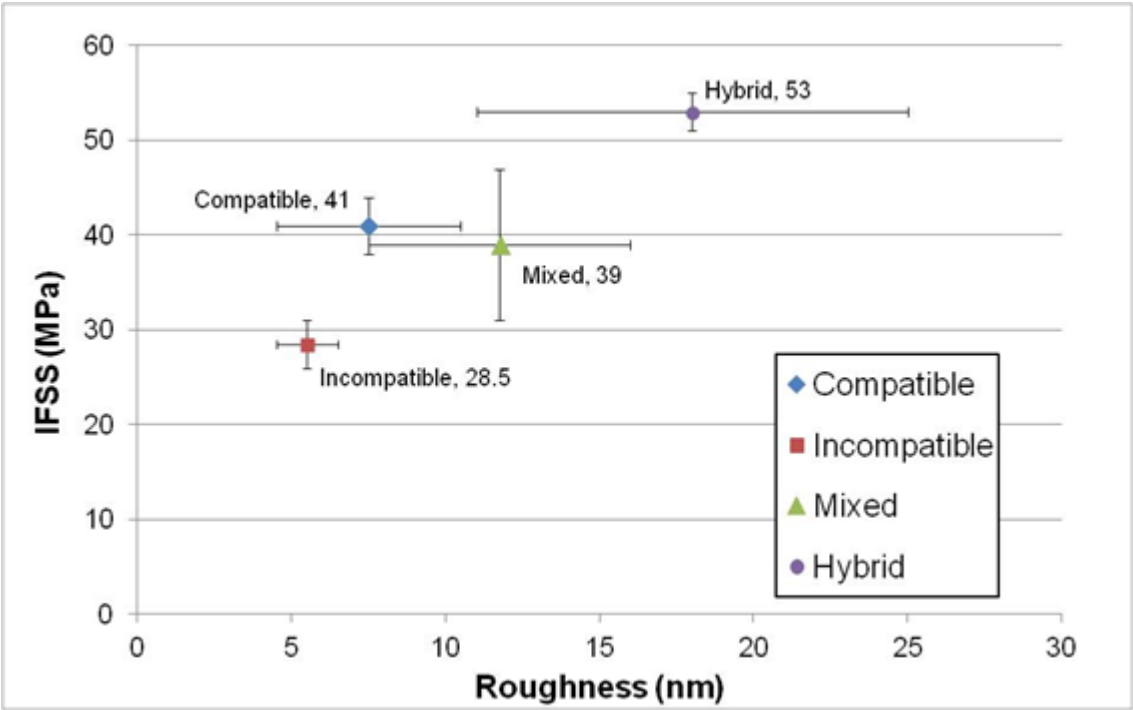

(a)

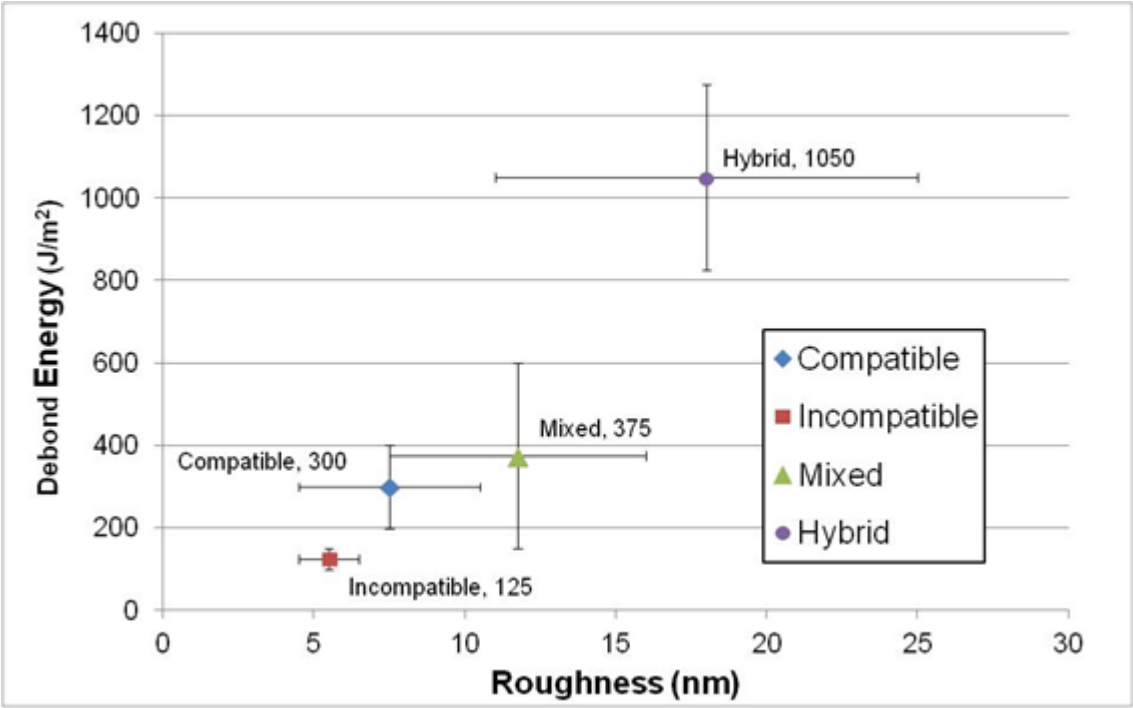

(b)

Fig. 2.13. Summary of (a) IFSS and (b) specific debonding energy results [1, 3] for glass/epoxy microdroplet specimens with different fiber sizings.

crack path is more tortuous due to the presence of the fiber sizing asperities (created by the silica nanoparticles) and therefore "changes the stress distribution at the fiber/resin interface which involves the plastic deformation of a larger volume of material during fracture as seen from the bumpy failure surface" [3]. Finally, Gao et al. [1, 3] note that the predominant cohesive failure mode is observed in composites with high shear strengths, as reported in [59].

2.6 Summary

The fiber sizing is shown to react with the matrix resin during the processing of the composite material to produce a finite thickness region with distinct material properties surrounding the fiber that is commonly referred to as the interphase region. The interphase, being located between the fiber and the bulk matrix, governs the load transfer from the bulk matrix to the fiber and is therefore an important feature of composite materials. Common standard testing methods for characterizing the mechanical behavior of the interphase are introduced with an emphasis on the microdroplet test. Lastly, the experimental research of Gao et al. [1-3] is summarized; the experimental data indicates that the mechanical interlocking provided by the highly textured fibers allows for simultaneous increases in strength and toughness.

REFERENCES

1. Gao X, Jensen RE, McKnight SH, and Gillespie Jr. JW, "Effect of colloidal silica on the strength and energy absorption of glass fiber/epoxy interphases," Composites: Part A (2011) A42: 1738-1747.

2. Gao X, Jensen RE, Li W, Deitzel J, McKnight SH, and Gillespie Jr. JW, "Effect of Fiber Surface Texture Created from Silane Blends on the Strength and Energy Absorption of the Glass Fiber/Epoxy Interphase," J. Compos. Mats (2008) 42: 513-533.

3. Gao X, "Tailored interphase structure for improved strength and energy absorption of composites," Ph.D. Dissertation, University of Delaware, 2006.

4. Thomason JL and Dwight DW, "The use of XPS for characterization of glass fibre coatings," Composites Part A (1999) 30: 1401-1413.

5. Tanoglu M, Ziaee S, McKnight SH, Palmese GR, and Gillespie Jr. JW, "Investigation of properties of fiber/matrix interphase formed due to the glass fiber sizing," J. of Mat. Sci. (2001) 36: 3041-3053.

6. Tanoglu M, McKnight SH, Palmese GR, and Gillespie Jr. JW, "A new technique to characterize the fiber/matrix interphase properties under high strain rates," Composites Part A (2000) 31: 1127-1138.

7. Jensen RE and McKnight SH, "Inorganic-organic fiber sizings for enhanced energy absorption in glass fiber-reinforced composites intended for structural applications," Compos. Sci. and Tech. (2006) 66: 509-521.

8. Thomason JL and Adzima LJ, "Sizing up the interphase: an insider's guide to the science of sizing", Composites Part A (2001) 32: 313-321.

9. Gorowara RL, Kosik WE, McKnight SH, and McCullough RL, "Molecular characterization of glass fiber surface coatings for thermosetting polymer matrix/glass fiber composites," Composites Part A (2001) 32: 323-329.

10. Plueddemann EP, "Reminiscing on silane coupling agents," J. of Adhesion Science and Technology (1991) 5: 261-277.

11. Plueddemann EP, *Silane Coupling Agents*, Plenum, NY, 1983.

12. Mader E, Moos E, and Karger-Kocsis J, "Role of film formers in glass fibre reinforced polypropylene – new insighs and relation to mechanical properties," Composites Part A (2001) 32: 631-639.

13. DiBenedetto AT, "Tailoring of interfaces in glass fiber reinforced polymer composites: a review," Mater. Sci. and Engineering (2001) A302: 74-82.

14. Thomason JL, "The interface region in glass fibre-reinforced epoxy resin composites: 1. Sample preparation, void content and interfacial strength," Composites (1995) 32: 425-434.

15. Pukanszky B, "Interfaces and interphases in multicomponent materials: past, present, future," European Polymer Journal (2005) 41: 645-662.

16. Yang F and Pitchumani R, "Effects of interphase formation on the modulus and stress concentration factor of fiber-reinforced thermosetting-matrix composites," Compos. Sci. and Tech. (2004) 64: 1437-1452.

17. Jancar J, "Review of the role of the interphase in the control of composite performance on micro- and na5no-length scales," J. Mater. Sci. (2008) 43: 6747-6757.

18. Jancar J, "The Thickness Dependence of Elastic Modulus of Organosilane Interphases," Polymer Composites (2008) 1372-1377.

19. Bikerman JJ, *The Science of Adhesive Joints*, 2nd ed., Academic Press, NY, 1968.

20. Sharpe LH, "The Interphase in Adhesion," J. Adhesion (1972) 4: 55-64.

21. Berg J and Jones FR,"The role of sizing resins, coupling agents and their blends on the formation of the interphase in glass fiber composites," Composites Part A (1998) 29: 1261-1272.

22. Mader E and Pisanova E, "Characterization and Design of Interphases in Glass Fiber Reinforced Polypropylene," Polymer Composites (2000) 21: 361-368.

23. Mader E, Moos E, and Karger-Kocsis J, “Role of film formers in glass fibre reinforced polypropylene – new insighs and relation to mechanical properties,” Composites Part A (2001) 32: 631-639.

24. Mader E and Pisanova E, “Characterization and Design of Interphases in Glass Fiber Reinforced Polypropylene,” Polymer Composites (2000) 21: 361-368.

25. Pompe G and Mader E, “Experimental detection of a transcrystalline interphase in glass-fibre/polypylene composites,” Compos. Sci. Tech. (2000) 60: 2159-2167.

26. Gao S-L and Mader E, “Characterization of interphase nanoscale property variations in glass fibre reinforced polypropylene and epoxy resin composites,” Composites: Part A (2002) 33: 559-576.

27. Bogetti TA, Wang T, VanLandingham MR, Eduljee RF, McCullough RL, and Gillespie Jr. JW, “Characterization of nanoscale property variations in polymer composite systems. Part 1: experimental results,” Composites A (1999) 30: 75-83.

28. Munz M, Sturm H, Schulz E, and Hinrichsen G, “The scanning force microscope as a tool for the detection of local mechanical properties within the interphase of fibre reinforced polymers,” Composites A (1998) 29: 1251-1259.

29. Mai K, Mader E, and Muhle M, “Interphase characterization in compostes with new non-desstructive methods,” Composites A (1998) 29: 1111-1119.

30. Yang F and Pitchumani R, “Effects of interphase formation on the modulus and stress concentration factor of fiber-reinforced thermosetting-matrix composites,” Compos. Sci. and Tech. (2004) 64: 1437-1452.

31. Wang J, Crouch SL, and Mogilevskaya SG, “Numerical modeling of the elastic behavior of fiber-reinforced composites with inhomogeneous interphases,” Compos. Sci. and Tech. (2006) 66: 1-18.

32. Matzenmiller A and Gerlack S, “Parameter identification of elastic interphase properties in fiber composites,” Composites: Part B (2006) 37: 117-126.

33. Dharan, CKH and Lin C-L, “Longitudinal Compressive Strength of Continuous Fiber Composites,” J. Compos. Mat. (2007) 41: 1389-1405.

34. Hashin Z, “Thin interphase/imperfect interface in elasticity with application to coated fiber composites,” J. of the Mechanics and Physics of Solids (2002) 50: 2509-2537.

35. Maligno AR, Warrior NA, and Long AC, “Effects of interphase material properties in unidirectional fibre reinforced composites,” Compos. Sci. and Tech. (2010) 70: 36-44.

36. Wang Q and Chiang F-P, “Experimental characterization of interphase mechanical properties of composites,” Composites Part B (1996) 27B:123-128.

37. Dow NF and Rosen BW, “Evaluations of filament-reinforced composites for aerospace structural applications,” NASA CR-207, 1965.

38. Tsai HC, Arocho AM, and Gause LW, “Prediction of fiber-matrix properties and their influence on the interface stress, displacement and fracture toughness of composite material,” Mat. Sci. and Engineering (1990) A126: 295-304.

39. Herrera-Franco PJ and Drzal LT, “Comparison of methods for the measurement of fibre/matrix adhesion in composites,” Composites (1992) 23: 2-27.

40. Tanoglu M, McKnight SH, Palmese GR, and Gillespie Jr. JW, “The effects of glass-fiber sizings on the strength and energy absorption of the fiber/matrix interphase under high loading rates,” Compos. Sci. and Tech (2001) 61: 205-220.

41. Tanoglu M, McKnight SH Palmese, GR, and Gillespie Jr. JW, “A new technique to characterize the fiber/matrix interphase properties under high strain rates,” Composites Part A (2000) 31: 1127-1138.

42. Kelly A and Tyson WR, “Tensile properties of fiber-reinforced metals: copper/tungsten and copper/molybdenum,” J. Mech. Phys. Solids (1965) 13: 329-350.

43. Zhao FM, Okabe T, and Takeda N, “The estimation of statistical fiber strength by fragmentation tests of single-fiber composites,” Compos. Sci. Tech (2000) 60: 1965-1974.

44. Zhandarov S and Mader E, “Characterization of fiber/matrix intervace strength: applicability of different tests, approaches, and parameters,” Compos. Sci. Tech. (2005) 65: 140-160.

45. Jensen RE and McKnight SH, “Inorganic-organic fiber sizings for enhanced energy absorption in glass fiber-reinforced composites intended for structural applications,” Compos. Sci. and Tech., 66 (2006) 509-521.

46. Foley ME, Obaid AA, Huang X, Tanoglu M, Bogetti TA, McKnight SH, and Gillespie Jr. JW, “Fiber/matrix interphase characterization using the dynamic interphase loading apparatus,” Composites Part A (2002) 33: 1345-1348.

47. Miller BP, Muri P, and Rebenfeld L, “A microbond method for determination of the shear strength of a fiber/resin interface,” Compos. Sci. Tech. (1987) 28: 17-32.

48. Day RJ and Rodrigez JVC, “Investigation of the micromechanics of the microbond test,” Compos. Sci. and Technol. (1998) 58: 907-914.

49. Kang SK, Lee DB, and Choi NS, ”Fiber/epoxy interfacial shear strength measured by the microdroplet test,” Compos. Sci. Technol. (2009) 69: 245-251.

50. Park JM, Kim DS, Kong JW, Kim M, Kim W, and Park IS, “Interfacial adhesion and microfailure modes of electrodeposited carbon fiber/epoxy-PEI composites by microdroplet and surface wetability tests,” J. Colloid and Interface Sci. (2002) 249:62-77.

51. Park J-M, Wang Z-J, Kwon D-J, Gu G-Y, and Um M-K, “Evaluation of interfacial properties and microfailure mechanisms in single fiber-reinforced epoxy composites at low temperature,” Polymer Composites (2012) 147-157.

52. Liu CH and Nairn JA, “Analytical and experimental methods for a fracture mechanics interpretation of the microbond test including the effects of friction and thermal stresses,” Intl. J. of Adhesion and Adhesives (1999) 19: 59-70.

53. Hodzic A, Kalyanasundaram S, Lowe AE, and Stachurski ZH, “Geometric considerations in the experimental and finite element analyses of the microdroplet test,” Proc. Of the ICCM 12, Paris, France, July 1999.

54. Pandey G, Kareliya CH, and Singh RP, “A study on the effect of experimental test parameters on data scatter in microbond testing,” J. Compos. Materials (2012) 46: 275-284.

55. Pisanova E, Zhandarov S, Mader E, “How can adhesion be determined from micromechanical tests?,” Composites: Part A (2001) 32:425-34.

56. Ash JT, Cross WM, Svalstad D, Kellar JJ, and Kjerengtroen L, “Finite element of the microbond test: meniscus effect, interphase region, and vise angle,” Compos. Sci. and Technol. (2003) 63: 641-651.

57. Scheer RJ and Nairn, JA, “A comparison of several fracture mechanics methods for measuring interfacial toughness with microbond tests,” J. Adhesion (1995) 53: 45-68.

58. Minnicino MA and Santare MH, “Modeling the progressive damage of the microdroplet test using contact surfaces with cohesive behavior,” Compos. Sci. and Technol. (2011) 72: 2024-2031.

59. Packham DE, “Surface energy, surface topography and adhesion,” Intl. J. Adhesion and Adhesives (2003) 23: 437-448.

60. Bagwell RM and Wetherhold RC, “Fiber pullout behavior and impact toughness of short shaped copper fibers in thermoset matrices,” Composites Part A (2005) 36: 683-690.

61. Tsai JH, Patra A, and Wetherhold RC, “Finite element simulation of shaped fiber pullout using a mixed cohesive zone/friction interface model,” Composites Part A (2005) 36: 827-838.

62. Walker PJ and Dobson S, “Pullout tests on deformed and plain rebars in cement-stabilized rammed earth,” J. Mat. In Civ. Engr., (2001) 13: 291-297.

63. Chou S and Lin L-S, “Effect of colloidal silica on adhesion of glass fiber to polypropylene,” Polymers & Polymer Composites (2001) 9: 175-183.

64. Gama B and Gillespie Jr. JW, “Energy absorbing damage mechanisms in quasi-static punch shear of thick-section composites,” Proc. of SAMPE, 2004.

Chapter 3

MODELING THE MICRODROPLET TEST

3.1 The Microdroplet Test

The microdroplet test evolved from a pull-out test originally developed by Miller et al., then called the microbond test, for the purpose of quantifying the interfacial strength between the fiber and matrix in single fiber specimens [1-3]. The microdroplet test is a conceptually simple method that shears a single cured resin droplet from a fiber using a set of opposing blades, i.e. a microvise, resulting in a load-displacement curve which can be used to quantify interfacial strength [1-15]. A schematic of the microdroplet test setup, with important dimensions labeled, is shown in Fig. 3.1(a) and a representative load-displacement curve (F-δ curve) obtained from the microdroplet test is shown in Fig. 3.1(b). The typical curve has three distinct regions: undamaged, damaged, and failed. The slope of the curve in the undamaged region is nearly constant for systems comprised of linear elastic materials. The curve begins to diverge from its initial linear trend at the "debond force" F_d, which marks the end of the undamaged region and the beginning of the damaged region of the F-δ curve. The debond force marks the initiation of crack development. The load continues to increase beyond F_d, as the crack length and damage increase until the maximum load F_{max} is achieved. At load F_{max}, the fiber completely

debonds from the matrix causing the length and damage increase until the measured force to fall to the frictional pull-out force F_f. Microdroplet test failure locations are often modeled [4, 7-9, 18-24] and reported [1-5, 10-15, 22, 24] to be at the fiber-matrix interface. The three possible modes of failure in the microdroplet test are cohesive, adhesive and bulk matrix failure and are shown schematically in Fig. 3.2.

The maximum force measured during the microdroplet test is used to calculate the interfacial shear strength (IFSS) of the fiber-matrix interface using the equation,

$$IFSS = \bar{\tau} = \frac{F_{peak}}{\pi d_f l_e} \tag{3.1}$$

where $\bar{\tau}$ denotes the *average* value of the shear strength, F_{max} is the measured force on the fiber at failure, d_f is the fiber diameter and L_e is the fiber embedded length. An

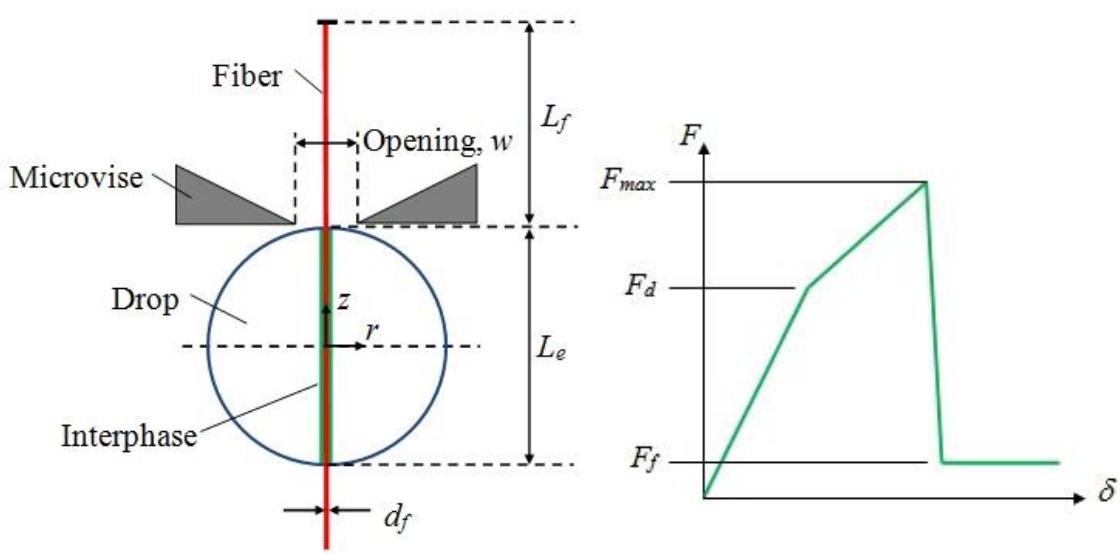

(a) (b)

Fig. 3.1. Microdroplet test (a) setup and (b) notional force-displacement response.

implicit assumption inherent in Eq. (3.1) is that the shear traction τ is nearly uniform along the interface and that failure is due to Mode II fracture. However, Pisanova et al., and Zhandarov and Mader define an "adhesional" pressure parameter to model the initial interfacial failure of microdroplet tests due to surface normal tension, i.e. Mode I fracture [16-17]. The fracture initiation model developed by Pisanova et al. [17] is supported by analytical models discussed in Liu and Nairn [7] which analyzed the interfacial stress state of the microdroplet test and indicated that the shear stress is zero where the fiber enters the matrix while the radial stress is a maximum at this location; this conclusion is further supported by observation of the stress boundary conditions where the fiber enters and exits the droplet. Additionally, we reiterate Zhandarov and Mader's observation that the "adhesional" pressure failure criterion is valid only for crack initiation when the loading is Mode I is significant, since the loading transforms to Mode-II dominant fracture as crack length increases [4]. In light of mixed-mode loading and non-uniform interfacial shear stress, it is seen that Eq. (3.1) may be too simplistic for predicting the load resulting in interface failure.

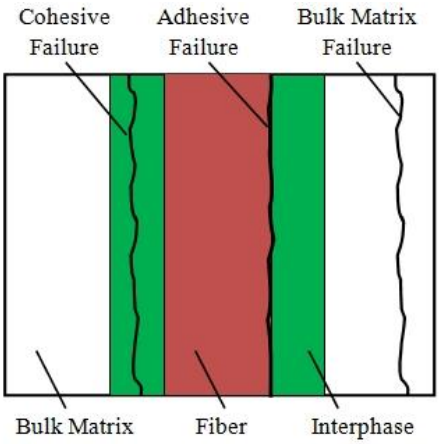

Fig. 3.2. Single fiber test failure modes: cohesive, adhesive, and bulk matrix (cohesive).

Day and Rodrigez [20], Kang et al. [22] and Ash et al. [18] used the finite element (FE) method to simulate the microdroplet test at a constant load without accounting for material damage or the progression of failure. These efforts used 2D axisymmetric FE models. The Day and Rodrigez FE model showed that the "blade" or microvise opening has a marked effect on the fiber strain and consequently the interfacial stress profile. Kang et al. experimentally showed that the IFSS increases with an increase in the embedded fiber length, L_e. Further, they determined that the shear stress profile along the fiber-matrix interface depends on the exterior geometry of the matrix droplet. Ash et al. parametrically studied the stress profiles along the fiber-interphase at a constant load for an interphase material of varying stiffness and found that the interphase stiffness had little effect on the macro-behavior of the system. Ash et al. also showed that the stress profile along the fiber-interphase depends on the size of the microvice opening. Liu and Nairn [7] developed analytical models for the crack propagation between a steel rod and an epoxy cylinder loaded in shear and compared the results to their simulations using a modified virtual crack closure technique (VCCT). They reported good agreement with their analytical predictions provided that the simulated debond tip was located in the center of the specimen. However, they noted poorer agreement between the analytical and numerical results when the debond tip was located near the rod-epoxy interfacial endpoints [7].

Although these studies provide a solid basis for understanding the mechanics of the microdroplet test, most consider a static view of the microdroplet experiment. With the exception of the VCCT FE model [7], the previous studies do not consider the

progression of damage along the interphase. The FE model of Liu and Nairn [7] uses the VCCT method, which includes damage evolution, however its use requires the introduction of an initial flaw. In addition, the authors [7] report that the numerical solution convergence of the method is sensitive to the location of the initial flaw, i.e. debond tip. The current study features an FE model, which allows progressive damage of the interphase between a glass fiber and the epoxy in a microdroplet test using surface-based cohesive behavior. This allows us to model the onset and progression of the adhesive failure of the fiber-droplet interface by using a traction-separation description of the interphase behavior, thereby avoiding the need for interphase continuum elements or the imposition of an initial flaw. Before the microdroplet models are presented, the surface-based cohesive theory used to model the progressive damage of the fiber-droplet interface is briefly discussed.

3.2. Surface-Based Cohesive Behavior

In this research, the Abaqus FE solver is used to simulate the microdroplet experiment. Further, the interphase constitutive relationship is modeled using surface-based contact with cohesive behavior. The cohesive element and contact behavior theory and notation used in Abaqus [25] is nearly identical to that derived by Camanho et al. [26]. In this research, the slave contact elements are defined as the droplet surface elements at the fiber-droplet interface and the master contact elements are defined as the fiber surface. The slave nodes are released from the master surface when the interface stress meets the cohesive contact failure criterion. Interpenetration between the released

slave nodes and the master surface is prevented by contact. Additionally, the failed cohesive contact surfaces may be assigned a friction coefficient.

The undamaged and uncoupled, i.e. off-diagonal stiffness components are zero, linear elastic traction-separation cohesive surface behavior is defined as

$$t = \begin{Bmatrix} t_n \\ t_s \\ t_t \end{Bmatrix} = \begin{bmatrix} K_n & \mathbf{0} & 0 \\ 0 & K_s & 0 \\ 0 & 0 & K_t \end{bmatrix} \begin{Bmatrix} \delta_n \\ \delta_s \\ \delta_t \end{Bmatrix} = K\delta \tag{3.2}$$

where the surface traction, t, is the product of the cohesive stiffness, K, and the contact separations, δ, and the subscripts s, t, and n are the first and second orthogonal in-plane shear and the normal component of the traction vector in the cohesive contact element coordinate system, respectively. The contact separation for a specific slave node at a particular instant is defined as the position vector from the master surface "anchor" point (the location of the slave node projected along the master surface normal onto the master surface at time t_0 - the beginning of the analysis) to the slave node location in the current configuration as shown in Fig. 3.3; the components of the contact separation vector are δ_n, δ_s, and δ_t. In the case of surface-based cohesive contact, tractions are defined as the nodal cohesive force divided by the contact surface area at each contact node [25]. Note that for unit consistency, the cohesive stiffness K has units of stress per length, i.e. MPa/m. A progressive damage traction-separation behavior with linear damage evolution law for scalar damage variable d_i is shown graphically in Fig. 3.4.

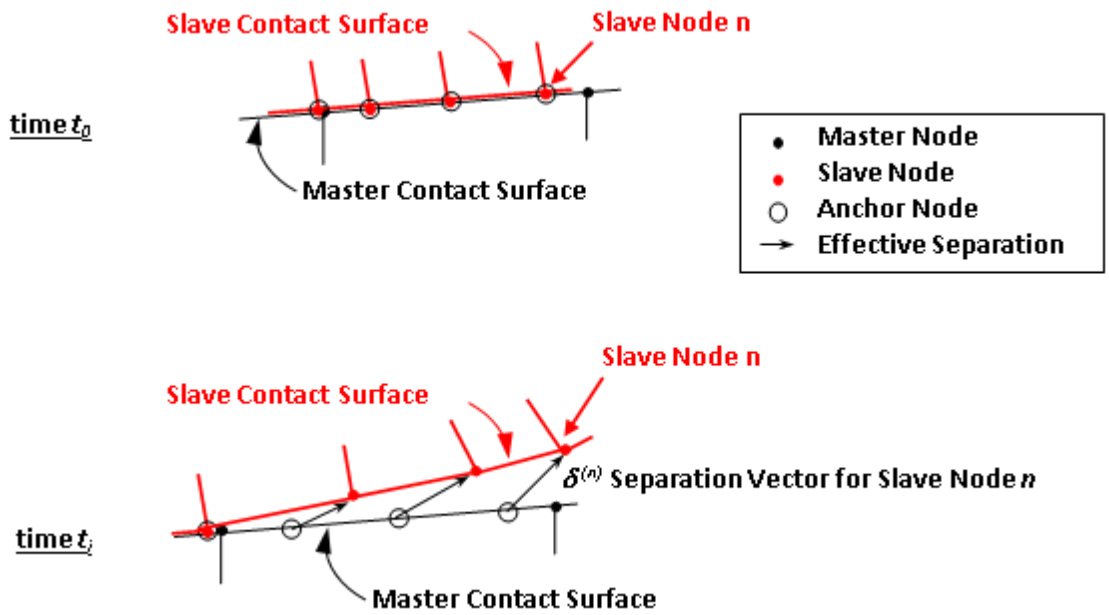

Fig. 3.3. Generic 2D deformation from time t_0 to t_i where the slave nodes displace according the traction-separation law (until complete failure) and the separation vectors are shown for each slave node.

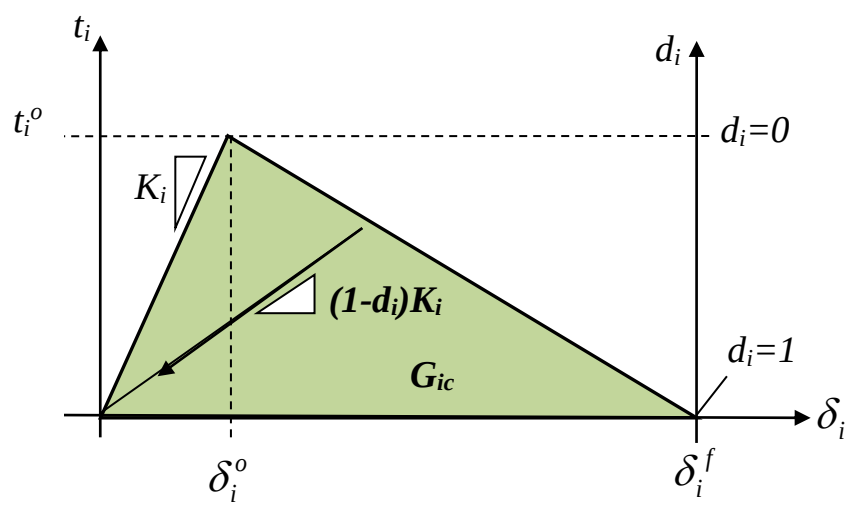

Fig. 3.4. Graphic illustration of the traction-separation behavior for a single mode *i* including progressive damage response.

The onset of cohesive damage is defined by one or more damage initiation criteria. In this research, damage initiation is defined in terms of a maximum stress criterion that is expressed as

$$\max\left\{\frac{<t_n>}{t_n^o}, \frac{t_s}{t_s^o}\frac{t_t}{t_t^o}\right\} = 1 \tag{3.3}$$

where t_i^o for i= n, s, and t are the cohesive normal strength and the two shear strengths at damage initiation, respectively. Additionally, the Macaulay brackets $< x >$ are used to indicate that compressive surface traction normal to the contact surface, does not affect the cohesive behavior of the contact surface. The damage initiation separations δ_i^o are given as

$$\delta_n^o = \frac{t_n^o}{K_n}; \qquad \delta_s^o = \frac{t_s^o}{K_s}; \qquad \delta_t^o = \frac{t_t^o}{K_t}. \tag{3.4}$$

The cohesive behavior undergoes further damage by following a damage evolution law. Generally, multiple damage evolution laws can be simultaneously defined for an interface. A damage variable d_i is defined for each damage evolution law used in the analysis and is zero at the onset of damage ($d_i=0$) and unity at complete failure ($d_i=1$). For multiple damage evolution laws, a scalar damage variable D is needed to represent the overall damage at a slave node due to the multiple defined damage mechanisms; further the individual damage variables may be chosen to combine in a multiplicative sense

$$d_{mult} = 1 - \prod_{i}^{Nmult}(1 - d_i), i \in N_{mult} \tag{3.5}$$

or in a maximum sense

$$d_{\max} = \max(d_j),\ j \in N_{\max} \tag{3.6}$$

where N_{mult} and N_{max} are the set of defined damage evolution laws that combine in multiplicative manner or act in a maximum sense, respectively. The overall scalar damage variable is

$$D = \max(d_{mult}, d_{\max}) \tag{3.7}$$

and is used to soften the traction-separation relation (3.2) via the relation,

$$t = (1-D)\, K\delta. \tag{3.8}$$

The damage evolution law is made up of two parts and may be defined in terms of separation displacement or fracture energy. The first part defines the effective separation distance that results in complete failure and may be expressed in terms of the effective separation distance relative to damage initiation or the total energy dissipated due to fracture, G_c. In this work, the separation distance is defined by specifying the fracture energy G_c. The second part is the relation governing the progressive growth of the damage variables from damage initiation to complete failure. The evolution of the damage variable, commonly referred to as the damage softening relation, can take on any functional relationship (e.g. linear, exponential, or user-defined). In this work, the damage softening is chosen to be linear.

Two evolution laws are used in this research; the individual damage variables act in a maximum sense, i.e. treated as a separate damage variables per Eq. (3.6), in the first evolution law with linear softening. The corresponding damage variable is defined as

$$d_i = \frac{\delta_i^f}{\delta^{\max}} \frac{(\delta_i^{\max} - \delta_i^o)}{(\delta_i^f - \delta_i^o)}; \; d_i \in [0,1] \tag{3.9}$$

where $\delta_i^{\max}$ is the maximum contact separation in the progression of the numerical solution in the ith direction and corresponds to the separation distance at complete failure. It should be noted that the progression of d_i is not linear with δ_i but rather the reduction of traction t_i is linear with the progression of δ_i. In this work, we set $\delta_i^{\max}$ by specifying the in terms of fracture toughness; therefore the resulting contact opening displacements at complete failure are

$$\delta_s^f = \frac{2G_{IIc}}{S}; \quad \delta_t^f = \frac{2G_{IIIc}}{T}; \quad \delta_n^f = \frac{2G_{Ic}}{N} \tag{3.10}$$

where G_{ic} is the cohesive surface fracture toughness and δ_i^f is the contact separation at complete failure in Mode I, Mode II, and Mode III, respectively.

The second evolution law uses the individual damage variables in a multiplicative sense, i.e. the effect of all damage variables are included in the global overall damage variable per Eq. (3.5), with linear softening. The second damage evolution law used in this research uses a power law relationship to define complete failure

$$\left(\frac{G_n}{G_n^C}\right)^n + \left(\frac{G_s}{G_s^C}\right)^n + \left(\frac{G_s}{G_s^C}\right)^n = 1 \tag{3.11}$$

where n=1 is specified in this work. This evolution law captures the reduction in interface strength due to mixed-mode conditions and is expressed in terms of the individual normal and shear (first and second shear directions) fracture toughness values.

3.3 Development of a 3D Finite Element Model

3.3.1 General Model

The three-dimensional (3D), quarter-symmetric, Abaqus/Standard FE model used to investigate the progressive failure of the microdroplet test is shown in Fig. 3.5. Our journal paper [23] associated with this model represents the first published FE model to use cohesive contact to simulate the progressive damage of the fiber-droplet interface during the microdroplet test. To simplify the analysis, an axisymmetric, annular microvise is modeled in place of the prismatic microvise geometry that is commonly used in such tests. However, it is noted that an FE model using a prismatic microvise will produce a more complex stress state in the fiber and droplet, which will have polar angle dependence and is a more accurate representation of the actual test setup as shown in Fig. 3.1(a). The glass fiber has a uniform diameter of 20 μm and its embedded length is

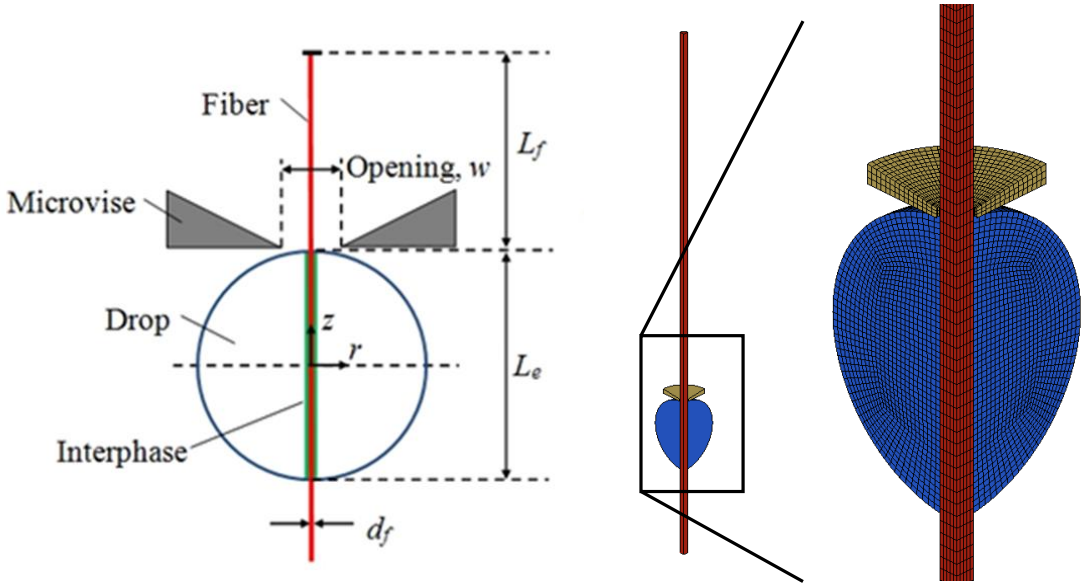

Fig. 3.5. Microdroplet test (a) schematic and (b) quartersymmetric 3D FE model.

150 μm. The microvise is modeled as an axisymmetric rigid structure with opening diameter w of 24 μm. The fiber free length L_f is 0.8 mm. The epoxy droplet is spherical with a diameter of 150 μm and the meniscus of the droplet is not modeled for simplicity. (Kang et al. noted that the meniscus has a diminishing effect as the droplet diameter increases [9].) The model is comprised of 15897 deformable, eight-node, fully integrated, hexahedral elements. A convergence study is conducted using an increasingly refined droplet mesh with three mesh sizes of approximately 3, 2, and 1 μm along the droplet-fiber interface with an element aspect ratio of nearly two. Convergence is achieved in terms of maximum load and maximum initial traction magnitudes along the fiber-droplet interface with maximum differences of results for the meshes being less than 5%. The fiber and droplet meshes at the fiber-droplet interface are non-congruent, i.e. the elements do not share nodes at the interface, and surface-based cohesive contact is defined at the fiber-droplet interface. A displacement boundary condition of $u_z = 0.1$ mm is specified for the top (positive z-direction free-surface) fiber nodes and the microvise is fixed. The linear elastic material properties of the glass fiber and epoxy droplet are shown in Table 3.1. The sensitivity to the microdroplet force-displacement response is examined by varying the cohesive contact definition using the parameters listed in Table 3.2. Lastly, Model E of Table 3.2 is designated as the baseline FE model and its sensitivity to material elastic modulus and geometry variations is studied by creating models with the parameters identified in Table 3.3.

Table 3.1. Material properties used in 3D FE model

Material	Elastic Modulus, E (GPa)	Poisson's Ratio, υ (-)
Glass Fiber	76.0	0.22
Epoxy Droplet	3.2	0.36

Table 3.2. Isotropic cohesive properties used in 3D model

Model	*Strength, σ (MPa)*	*Fracture Toughness, G_c (J/m^2)*	*Friction Coefficient, μ (-)*
A	25	500	0.1
B	25	1000	0.1
C	25	1000	0.3
D	50	500	0.1
E	50	1000	0.1
F	50	1000	0.3
G	100	500	0.1
H	100	1000	0.1
I	100	1000	0.3

Table 3.3. Material and geometric variations to baseline model (Model E of Table 3.2)

Model	E_{fiber} (GPa)	E_{drop} (GPa)	L_f (μm)	d_f (μm)	Opening, w (μm)
Baseline (E)	**76**	**3.2**	**800**	**20**	**24**
E1	38				
E2		1.8			
E3			1000		
E4			1200		
E5				18	
E6					48
E7					72

3.3.2 Quartersymmetric FE Results

3.3.2.1 Cohesive behavior at the macroscale

The simulated microdroplet test load-displacement (F-δ) curves for cohesive behaviors A-I of Table 3.2 are shown Fig. 3.6 along with two experimental curves estimated from figures reported in [5]. The "Gao GPS" curve represents a baseline glass fiber-epoxy matrix microdroplet F-δ curve and the "Gao GT31" curve represents glass

fiber with highly textured sizing for optimized IFSS and toughness. In order to compare the simulated results to the experimental results, the Gao curves shown in Fig. 3.6 are modified from the reference, using the method described by Gao et al. [5, 27] to account for the apparatus compliance.

A careful analysis of the figure shows that the simulated F-δ curves exhibit a slight bilinear nature, (as opposed to the linear response noted in Kang et al. and Park et al. [9, 19]) the change in slope being more pronounced for lower strength and toughness cohesive behaviors. Fig. 3.6 also shows that the lower strength cohesive behaviors behave nearly identically as their higher strength counterparts up to a critical force/displacement. The point on the F-δ curves where the low-strength and high-strength behaviors diverge corresponds to the first released node on the failing contact surface. In other words, the traction-separation cohesive behaviors listed in Table 3.2 do not affect the system macro-behavior until damage is initiated. However, after damage initiation, both the cohesive strength and the cohesive fracture toughness influence both the peak load and maximum displacement before complete failure, as shown in Fig. 3.6. The larger the cohesive strength, the larger the debond force F_d, peak force F_{max} and the corresponding displacements. Similarly, the greater the cohesive fracture toughness the larger the debond force F_d, peak force F_{max} and corresponding displacements.

The simulated F-δ curves agree fairly well with the Gao curves, particularly the baseline curve to the Gao GPS curve, showing that contact with cohesive behavior can simulate the progressive damage encountered during the debonding. It should be noted that the agreement between the simulated and experimental curves does not indicate that

the selected cohesive parameters are the actual stiffness, toughness, etc. of the interface, but rather that they replicate the interface's macro-behavior. Because of the nonlinear nature of the analysis, there may be other parameter combinations that generate equally good agreement. The simulated F-δ curves agree less well with the Gao GT31 curve which was obtained from a highly textured fiber optimized for IFSS and toughness. This is due to mechanical interlocking; the GT31 curve represents much more bulk material failure in and around the interphase than the GPS curve, which is dominated by adhesive failure.

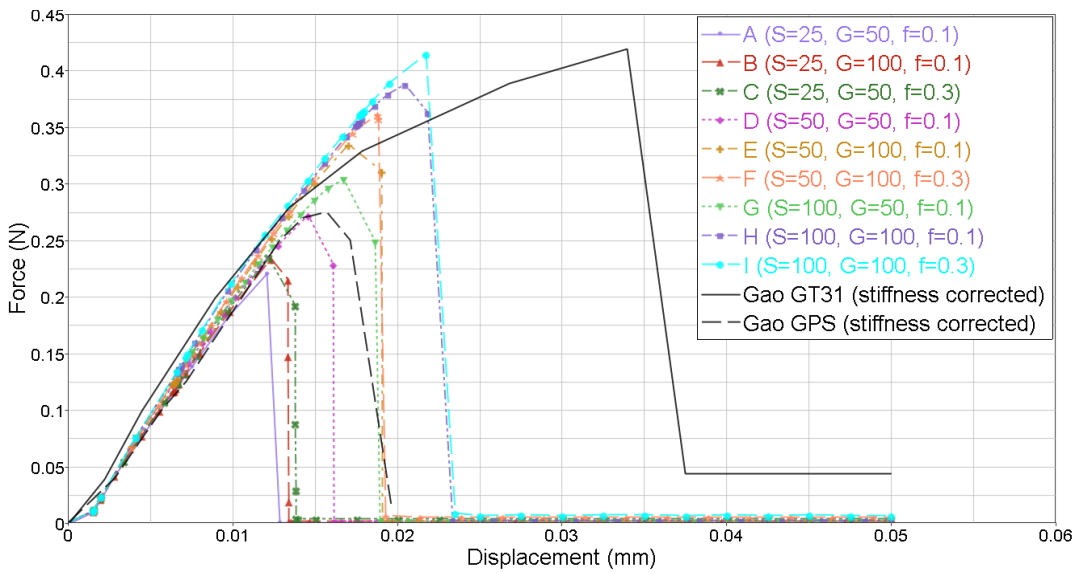

Fig. 3.6. Load-displacement curves of the cohesive models of Table 3.1 and selected experimental data from [5].

3.3.2.2 Cohesive contact surface stress profiles

The normal pressure and shear traction profiles along the normalized length l of the fiber-droplet interface, at the midplane between the two meridional, symmetry planes,

are shown in Fig. 3.7 for the cohesive contact behavior defined by Model E. Figure 3.7(a) shows the shear and pressure profiles before the onset of cohesive damage and Fig. 3.7(b) shows the profiles after damage has progressed. The zero abscissa location *l=0* corresponds to the uppermost point of the fiber-droplet interface. The traction profiles indicate a mixed-mode loading condition in the proximity of *l*=0, the location of damage

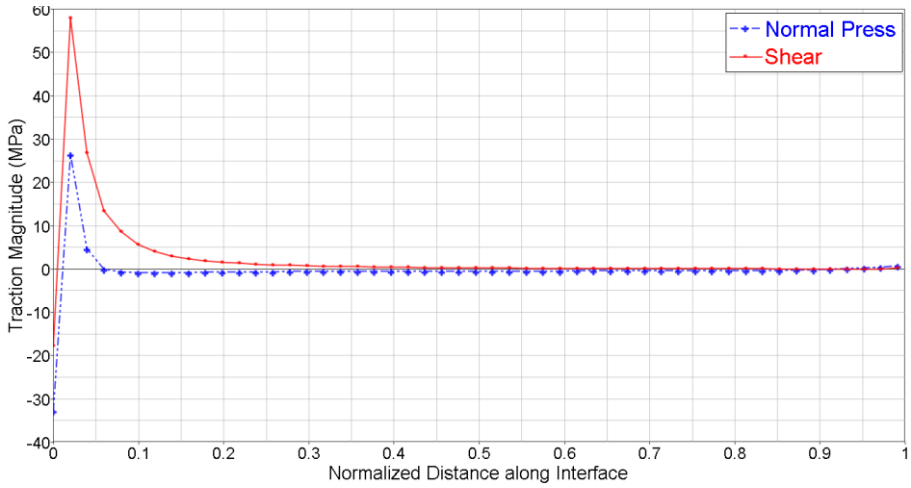

(a)

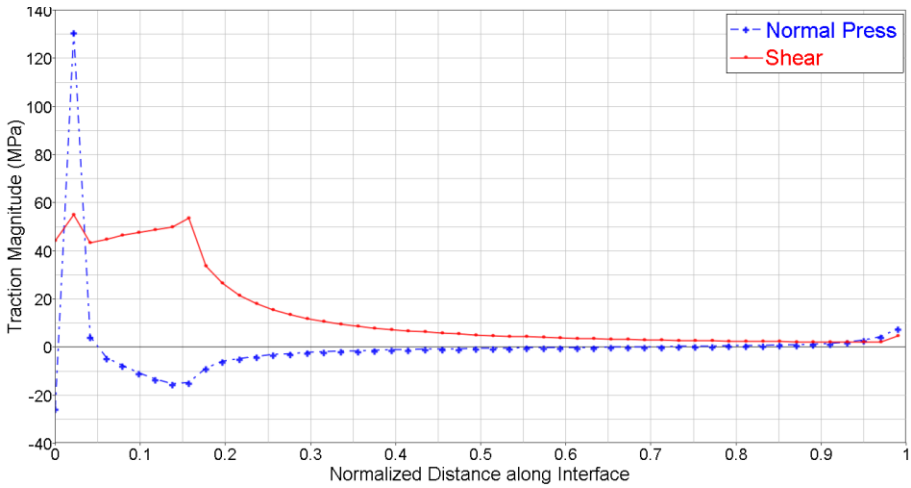

(b)

Fig. 3.7. Interface shear and normal traction profiles (a) before and (b) after damage.

initiation. Before failure begins, the normal and shear traction profiles are non-uniform and are largest in the region $0.0<l<0.02$ corresponding to the approximate axial location of the microvise. After the initiation of damage, the magnitude of the normal pressure along the interface is small compared to the shear magnitude except around the location of the microvise (l=0.01). These results show that at the location l=0.02, the microvise produces a "pinching effect" on the fiber resulting in a large localized pressure and associated frictional shear forces.

3.3.2.3 Modes of failure

We use the nodal interface traction components at the time of failure to define the cohesive mode ratio, η, as

$$\eta = \frac{\tau}{<\sigma> + \tau}; \quad 0 \le \eta \le 1 \tag{3.12}$$

where σ is the normal traction, τ is the shear traction, and the Macaulay brackets indicate that the compressive normal tractions do not contribute to the mode mix ratio as defined by Eq. (3.12) (this equation ignores the circumferential shear traction because it is found to be negligible). Mode ratio η = 0 corresponds to pure Mode I loading, η = 1 corresponds to pure Mode II loading, and values of η between these limits represent Mode I-Mode II mixed mode loading. The damage location, i.e. the location of the crack front, and failure mode as a function of microvise displacement is shown Fig. 3.8. The analysis shows that damage is initiated at a microvise displacement $\delta \approx 0.004$ mm and is located a normalized distance of l=0.02 from the top of the droplet due to Mode II loading as shown in Fig 3.8.

The fracture quickly becomes mixed mode, followed by slow transition back to Mode II at near complete failure of the interface which is characterized by development of two crack fronts: the initial crack front starting at l=0 and the second crack front starting at l=1 as shown in Fig 3.8.

The initial damage location was expected to occur at the uppermost contact point between the fiber and the droplet, i.e. l=0, based on the theories advanced in the literature [4, 6-7]. However, the simulations show that the initial damage location is at around l=0.02, likely due to the differences between the actual loading from the microvise and the idealized pure shear loading in the analytical models. (It should be noted that the specific location of the damage initiation point depends on the material parameters used in the simulation). Examining the pre-damaged results for locations l=0, where the fiber enters the droplet, shows that damage is initiated by mixed mode loading (η ~ 0.37) and fails due to mixed mode loading (η ~ 0.30), as shown in Fig. 3.9(a). A mode mix ratio of η = 0.38 is subsequently reported by Sockalingam et al. [24] and confirms this finding. Conversely, the results show that at location l=0.02 that damage is initiated and fails by pure Mode II loading, as shown in Fig. 3.9(b). As discussed in the next section, the volume of material under mixed-mode loading is affected by the size of the microvise opening.

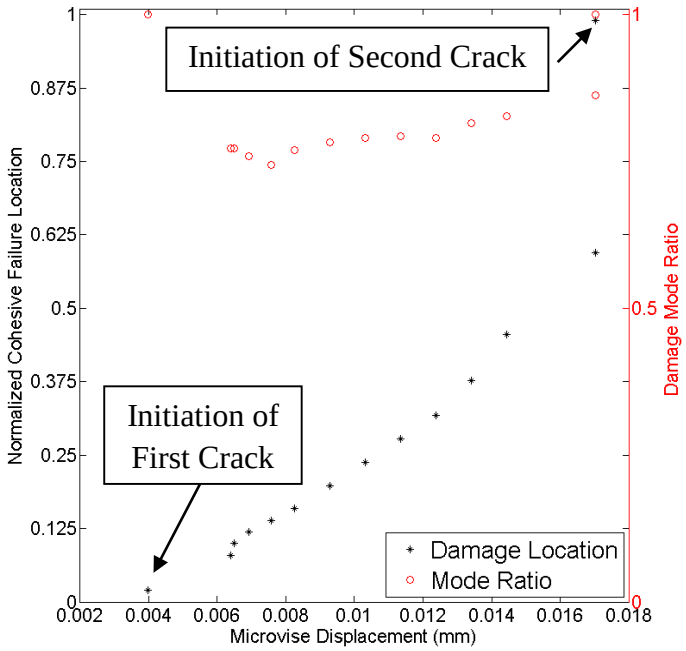

Fig. 3.8. Adhesive failure location-displacement history plotted with damage mode for the microdroplet test with Model E cohesive properties.

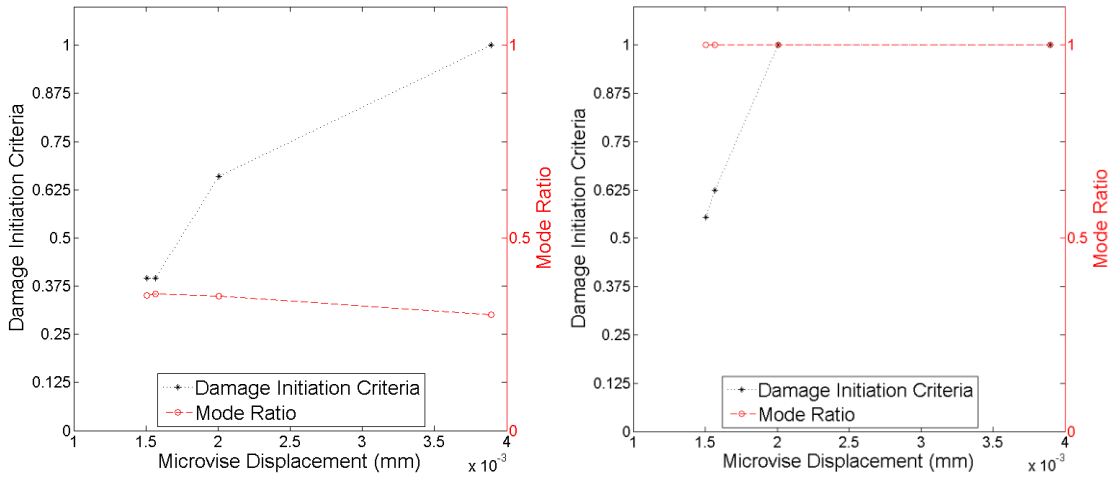

(a) (b)

Fig. 3.9. The maximum stress criterion and mode-mix ratio for the normalized location (a) l=0 and (b) the initial damage location l=0.02.

3.3.2.4 Sensitivity of the Microdroplet Test

Fig. 3.10(a) indicates that the overall displacement in the microdroplet test is dominated by the fiber elastic modulus and that a less stiff fiber enables larger test displacements due to stretching of the fiber. Additionally, Fig. 3.10(a) shows that the droplet elastic modulus has a secondary effect on the test displacement since the undamaged region of the F-δ curve is similar to the baseline curve. Fig. 3.10(b) shows that as the fiber free length L increases, the system stiffness K decreases; a 25% increase in fiber free length results in a force-displacement response stiffness decrease of 15.4%. Further, a 50% increase in fiber free length results in a stiffness decrease of 26%. Additionally, a 10% decrease in fiber diameter results in a stiffness decrease of 14.5% as shown in Fig.3.10(c). In addition to the fiber and droplet material parameters, the microvise opening was varied to assess its effect on the microdroplet F-δ curve and the results are shown in Fig. 3.10(d). This figure shows that overall stiffness of the system is relatively insensitive to the microvise opening diameter since the slopes are the same in the undamaged region of the F-δ curves. However, the simulation results indicate that the microvise opening affects the onset of damage with decreasing onset loads associated with decreasing microvise opening. As the microvise opening increases, a larger volume of droplet material is deformed and the shear traction at the contact interface becomes increasingly more uniform as shown in Fig. 3.11, resulting in higher overall load at onset.

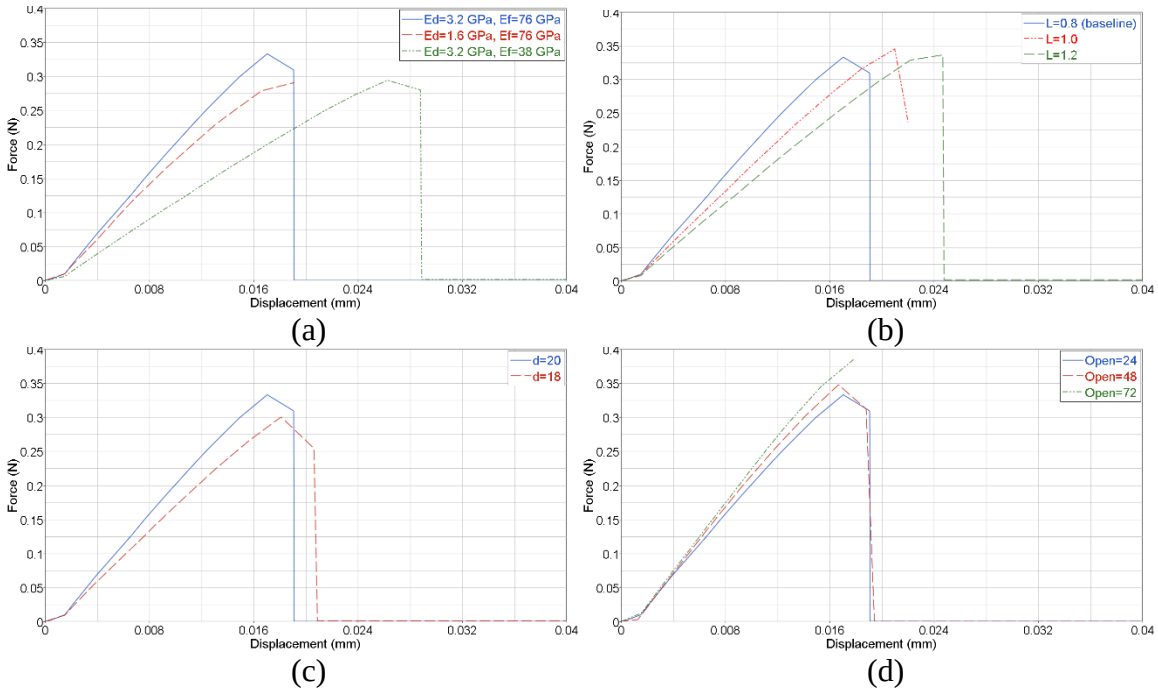

Fig. 3.10. *F*-δ curves obtained by varying (a) fiber and droplet elastic moduli, (b) fiber free length, (c) fiber diameter, and (d) microvise opening.

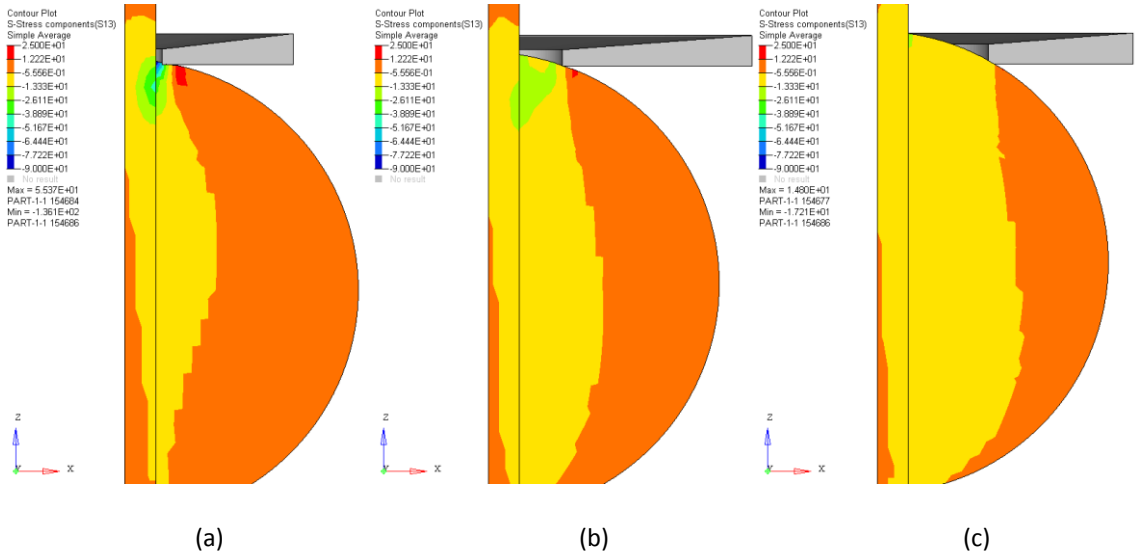

Fig. 3.11. Shear stress (σ_{rz}) stress contours for microvise opening (a) *w*=24 μm (baseline), (b) *w*=48 μm, and (c) *w*=72 μm

3.4 Development of the Axisymmetric Microdroplet Model

The axisymmetric microdroplet model used in this study (shown in Fig. 3.12) is adapted from the 3D quarter-symmetric FE model. The axisymmetric model approximates the geometry and nominal features of the microdroplet test reported in [5, 27]. The glass fiber diameter is 20 µm, the fiber-droplet interface length is 136 µm, and the droplet diameter is 136 µm. The glass fiber free length is 0.8 mm. Model convergence, measured as a maximum difference in reaction force being less than 2% between meshes with characteristic lengths of 1 µm and 0.5 µm, is achieved using linear, axisymmetric continuum elements. The droplet mesh is comprised of 34048 linear, axisymmetric continuum elements with a characteristic length of 0.5 µm. The fiber mesh is comprised on 11500 linear, axisymmetric continuum elements. The microvise is modeled as a rigid body and has an opening diameter of 30 µm; due to the model being axisymmetric, the microvise in the model is an annulus and not an opposing set of prismatic blades. The fiber nodes along the top edge are prescribed to have equal vertical displacement. In order to capture the initial slope of the experimentally measured load-displacement curve, it is necessary to include a spring element with a stiffness of 18 kN/m in the model between the virtual ground (‘X’ in Fig. 3.12) and the centerline node along the top edge of the fiber free length. The spring element represents the test apparatus compliance and is added to match the reported initial slope of the experimental force-displacement responses in [10, 27]. A residual stress due to curing of the epoxy droplet is developed by prescribing a temperature drop of 125 °C from the stress free temperature of 150 °C (the epoxy cure temperature) to 25 °C (ambient temperature) [24].

Table 3.4. Cohesive parameter values for microdroplet model parametric study

Simulation	1	2	3	4	5	6	7	8	9	10	11	12	13	14	15	16	17	18	19
K_n (10^{14} Pa/m)	1	***0.5***	1	***0.5***	***2***	1	***2***	1	1	1	1	1	1	1	1	1	1	1	1
K_s	1	1	***0.5***	***0.5***	1	***2***	***2***	1	1	1	1	1	1	1	1	1	1	1	1
N (MPa)	60	60	60	60	60	60	60	***30***	60	***30***	***90***	60	***90***	60	60	60	60	60	60
S	60	60	60	60	60	60	60	60	***30***	***30***	60	***90***	***90***	60	60	60	60	60	60
G_n (kJ/m^2)	1	1	1	1	1	1	1	1	1	1	1	1	1	***0.5***	1	***0.5***	***2***	1	***2***
G_s	1	1	1	1	1	1	1	1	1	1	1	1	1	1	***0.5***	***0.5***	1	***2***	***2***

This residual stress produces the interface tractions shown in Fig. 3.13 for temperature independent elastic parameters. The droplet is sheared from the fiber by downward motion of the microvise at a rate of 1 µm/sec. The mechanical properties for the glass fiber and epoxy droplet are the same used in the quarter-symmetric FE model (see Table 3.1). A mesh convergence study is conducted by refining the droplet mesh using three different meshed sizes with characteristic lengths h = 2, 1, and 0.5 µm and aspect ratios of approximately one. Convergence is achieved in terms of maximum load, steady-state pullout load, and radial force at the end of the thermal preload with maximum differences being less than 1% as shown in Fig. 3.14. A droplet mesh with characteristic length of 0.5 µm is used in the following simulations.

The axisymmetric FE model is used to predict the microdroplet force-displacement response for an assumed fiber topography, i.e. surface roughness, in the next chapter. However, to understand the influence of individual cohesive parameters on the microdroplet force-displacement response, a parametric study is conducted where the values for the cohesive normal strength, shear strength, normal fracture toughness, and shear fracture toughness are systematically varied. It is usually recommended that the

stiffness of the cohesive interface be sufficiently high such that the cohesive behavior has an insignificant effect on the initial response of the system [25, 28]. Consequently, a cohesive stiffness of 10^6 N/mm^3 (10^{15} Pa/m) is recommended in [28] when simulating the delamination of composite substrates. A preliminary study of the microdroplet FE model showed that a cohesive stiffness of 10^{14} Pa/m meets this criterion and this value was

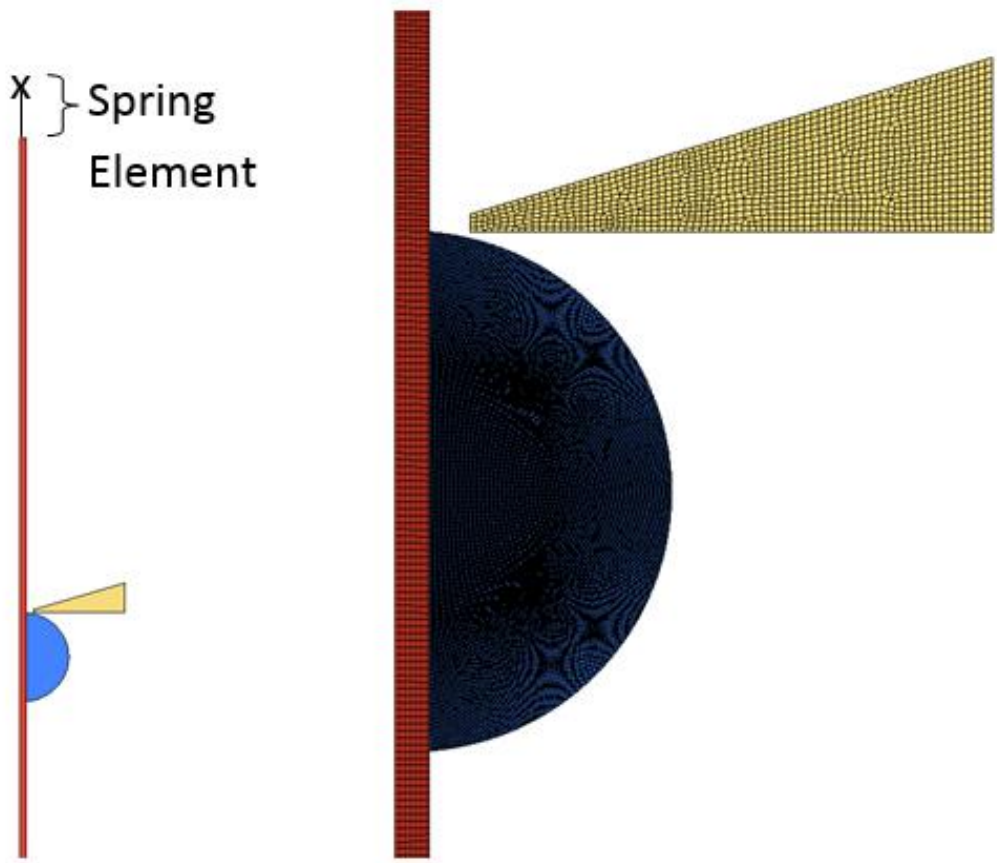

(a) (b)

Fig. 3.12. Axisymmetric (a) microdroplet model and (b) close-up of interface and mesh.

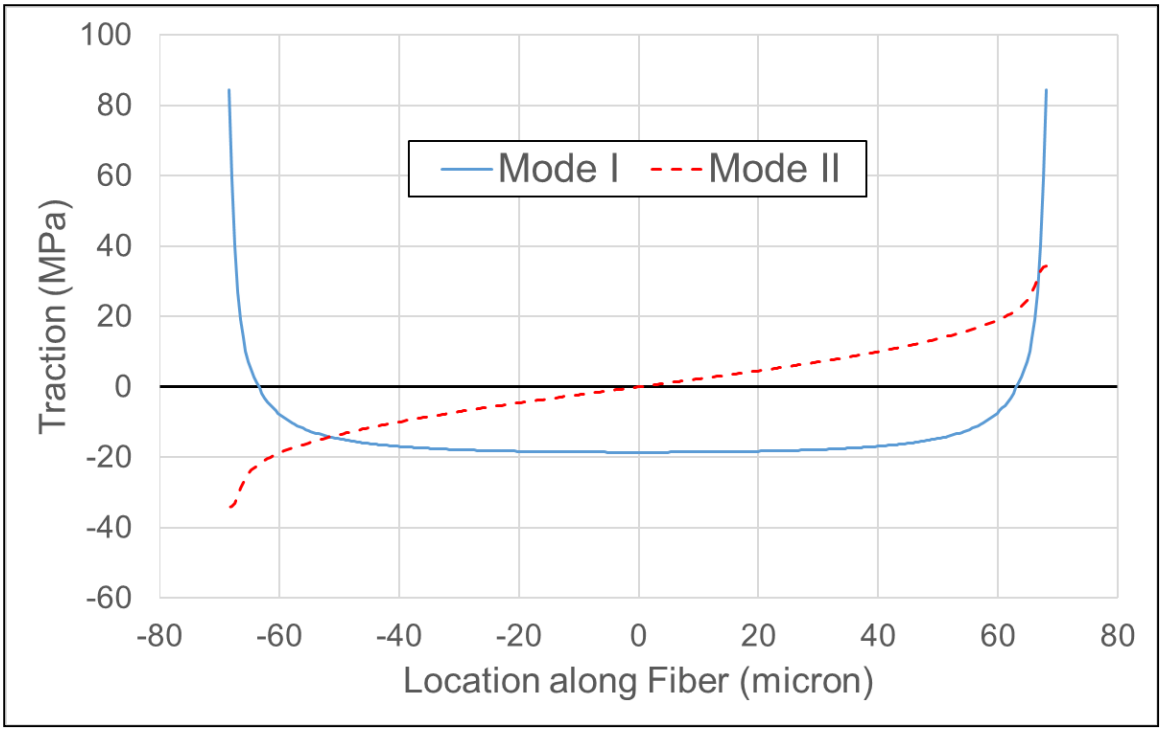

Fig. 3.13. Fiber-droplet interface traction distribution arising from thermal preload.

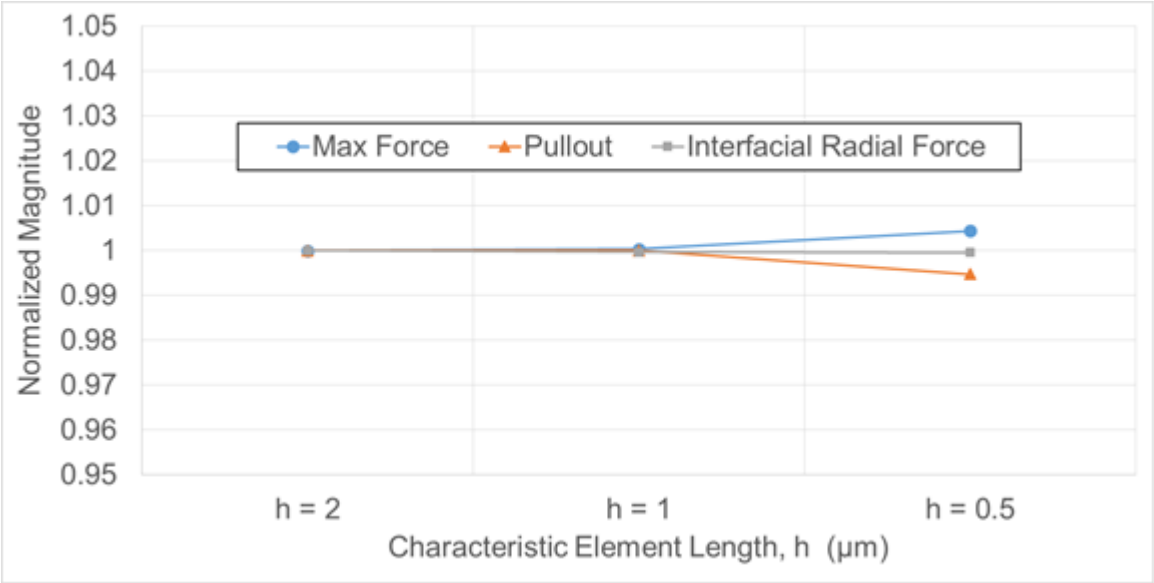

Fig. 3.14. FE model convergence study results.

therefore selected as the nominal cohesive stiffness for the parametric study. Additionally, we selected 60 MPa as the nominal cohesive strength and 1000 J/m^2 as the nominal cohesive fracture toughness. To stabilize the solution while satisfying the requirement that $\eta << \Delta t$ with the time increment (~1 sec) we chose a constant cohesive viscous regularization coefficient η of 10^{-4} sec. The additional cohesive parameter values used in the parametric model study are shown in Table 3.4.

A maximum stress criterion (Eq. (3.3)) is used to define damage initiation and a "power law" (Eq. (3.11)) with $n = 1$ is used to define the damage evolution in the cohesive interface. The microdroplet force-displacement behaviors resulting from the cohesive definitions listed in Table 3.4 are shown in Fig. 3.15. The following observations are made from these results:

- The normal cohesive stiffness has no significant effect on the force response. However, a lower cohesive shear stiffness (simulations 3 and 4) corresponds to a slightly greater displacement before sudden loss of load.

- The cohesive normal strength has no significant effect on the force response as shown by the results of Simulation 1, 8, and 11. The cohesive shear strength determines the microdroplet maximum force as well as the location on force curve where softening (due to debonding) starts. Also, we observe that a low cohesive shear strength and a relatively high cohesive toughness effectively loads the interface near the microvise up to yield where it then slowly softens (due to progressive damage). Therefore this combination more uniformly distributes the load over the interface resulting in the relatively long period of force decay for Simulations 9-10 in Fig. 3.15(b) and Simulations 18-19 in Fig. 3.15(c).

- The normal cohesive toughness has no significant effect on the force response (simulations 1, 14, and 17 are identical). However, we observe that the cohesive shear cohesive toughness affects both the maximum force and the post-maximum force behavior with increasing cohesive toughness resulting in greater maximum forces and longer periods of force decay.

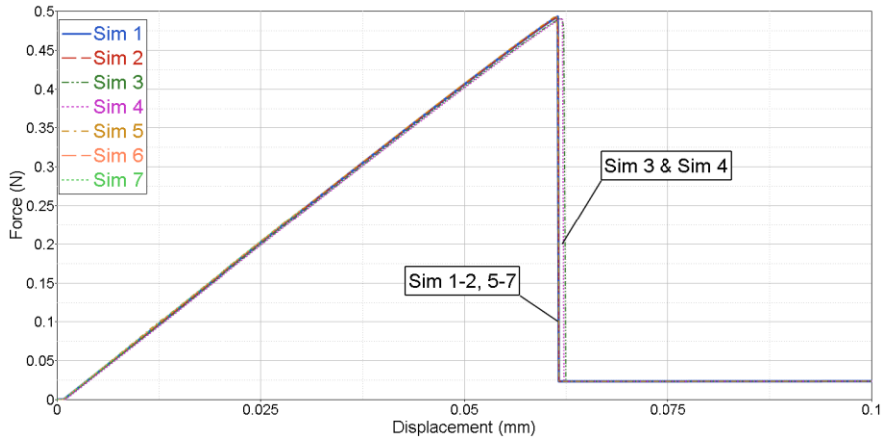

(a)

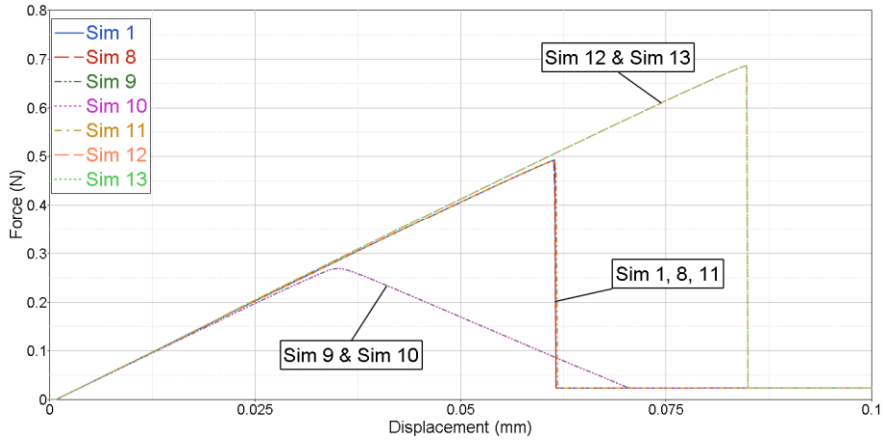

(b)

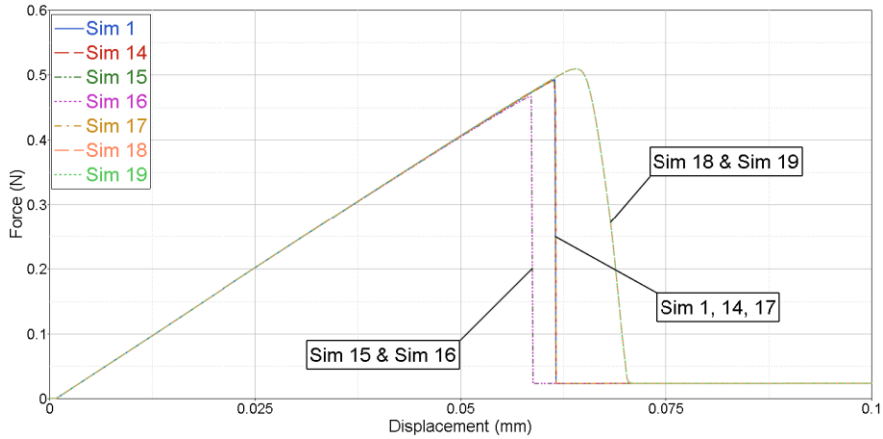

(c)

Fig. 3.15. Force responses for the microdroplet model parametric analyses showing the effect of cohesive (a) stiffness (simulations 1-7), (b) strength (simulations 1, 8-13), and (c) toughness (simulations 1, 14-19).

3.5 Summary

Cohesive contact surfaces are used to model the progressive damage along the fiber-droplet interface during the microdroplet test. Both the debond strength and the maximum force observed in a typical microdroplet test are shown to depend on fiber and droplet material elastic properties, the cohesive contact interfacial properties, and test conditions, i.e. test specimen geometry. The results from this study indicate that these properties and conditions need to be measured and controlled in order to better understand and interpret the microdroplet test data. Further, we have shown that the slope of the corrected F-δ curve is strongly influenced by the fiber free length and material properties and may be used to estimate the fiber free length.

The simulated traction profiles along the fiber-droplet interface after damage initiation are not uniform. Therefore assuming a uniform traction, such as used in the typical shear-lag analysis, underestimates the true IFSS. However, we believe that using the microdroplet test to measure the fiber-droplet interfacial shear strength is a relevant test of shear strength since the results show that the failure mode is predominantly Mode II at finite length cracks.

Finally, the axisymmetric FE model is computationally efficient compared to the quarter-symmetric, 3D FE model. The parametric analysis of the axisymmetric model indicates that the force-displacement response is dominated by shear direction cohesive parameters and is less affected by the out-of-plane, i.e. normal, cohesive parameters. The axisymmetric model is used in the next chapter as part of a multiscale modeling approach to estimate the force-displacement response of hypothetical fiber topography systems.

REFERENCES

1. Miller B, Muri P, Rebenfeld L. A microbond method for determination of the shear strength of a fiber/resin interface. Compos Sci Technol 1987;28:17–32.

2. Gaur U, Miller B. Microbond method for determination of the shear strength of a fiber/resin interface: Evaluation of experimental parameters. Compos Sci Technol 1989;34:35–51.

3. Miller B, Gaur U, Hirt D. Measurement and mechanical aspects of the microbond pull-out technique for obtaining fiber/resin interfacial shear strength. Compos Sci Technol 1991;42:207–19.

4. Zhandarov S., Mader E. Characterization of fiber/matrix interface strength: applicability of different tests, approaches and parameters. Compos Sci Technol 2005; 65:149-160.

5. Gao X, Jensen RE, Li W, Deitzel J, McKnight SH, Gillespie Jr JW. Effect of fiber surface texture created from island blends on the strength and energy absorption of the glass fiber/epoxy interphase. J. Compos Mats 2008; 42(5):513-22.

6. Pisanova E, Zhandarov S, Mader E. How can adhesion be determined from micromechanical tests? Composites: Part A 2001; 32:425-34.

7. Liu CH, Nairn JA. Analytical and experimental methods for a fracture mechanics interpretation of the microbond test including the effects of friction and thermal stresses. Intl. J. of Adhesion & Adhesives 1999; 19:59-70.

8. Day RJ, Rodrigez JV. Investigation of the micromechanics of the microbond test. Compos Sci Technol 1998; 58:907-914.

9. Kang SK, Lee DB, Choi NS. Fiber/epoxy interfacial shear strength measured by the microdroplet test. Compos Sci Technol 2009; 69:245-251.

10. Gao X, Jensen RE, Li W, Deitzel J, McKnight SH, Gillespie Jr JW. Effect of fiber surface texture created from silane blends on the strength and energy absorption of the glass fiber/epoxy interphase, J. Compos. Mats., 2008, 513-534.

11. Gao X, Jensen RE, McKnight SH, Gillespie Jr JW. Effect of colloidal silica on the strength and energy absorption of glass fiber/epoxy interphases. Compos. A, Appl. Sci. Manuf., 2011; 42(11): 1738–47.

12. Jensen RE and McKnight SH. Inorganic-organic fiber sizings for enhanced energy absorption in glass fiber-reinforced composites intended for structural applications. Compos. Sci. Technol., 2006; 66:503-521.

13. Yang L, Thomason JL. Interface strength in glass fibre–polypropylene measured using the fibre pull-out and microbond methods. Compos A., 2010; 41(9):1077–83.

14. Park JM, Kim DS, Kong JW, Kim M., Kim W., Park IS. Interfacial adhesion and microfailure modes of electrodeposited carbon fiber/epoxy-PEI composites by microdroplet and surface wetability tests. J. Colloid and Interface Sci., 2002; 249:62-77.

15. Pisanova E, Zhandarov S, Mader E, Ahmad I, Young RJ. Three techniques of interfacial bond strength estimation from direct observation of crack initiation and propagation in polymer–fibre systems. Composites: Part A, 2001; 32(3–4): 435–43.

16. Zhandarov SF, Pisanova EV. The local bond strength and its determination by fragmentation and pull-out tests. Compos Sci Technol., 1997; 57(8): 957–64.

17. Zhandarov S and Mader E, Characterization of fiber/matrix interface strength: applicability of different tests, approaches and parameters. Compos. Sci. Technol., 2005; 65:149-160.

18. Ash JT, Cross WM, Svalstad D, Kellar JJ, and Kjerengtroen L. Finite element evaluation of the microbond test:meniscus effect, interphase region, and vise angle. Compos Sci Technol 2003; 63:641-651.

19. Park JM, Kim DS, Kong JW, Kim M., Kim W., Park IS. Interfacial adhesion and microfailure modes of electrodeposited carbon fiber/epoxy-PEI composites by microdroplet and surface wetability tests. J. Colloid and Interface Sci 2002; 249:62-77.

20. Day RJ, Rodrigez JV. Investigation of the micromechanics of the microbond test. Compos Sci Technol., 1998; 58:907-914.

21. Pandey G, Kareliya CH, Singh RP. A study of the effect of experimental test parameters on data scatter in microbond testing. J Composite Materials, 2012; 46:275-284.

22. Kang SK, Lee DB, Choi NS. Fiber/epoxy interfacial shear strength measured by the microdroplet test. Compos Sci Technol., 2009; 69:245-251.

23. Minnicino MA, Santare MH. Modeling the progressive damage of the microdroplet test using contact surfaces with cohesive behavior. Compos Sci Technol 2012; 72(16): 2024–31.

24. Sockalingam S., Dey M, Gillespie Jr JW, Keefe M., Finite element analysis of the microdroplet test method using cohesive zone model of the fiber/matrix interface. Composites: Part A., 2014; 56:239-247.

25. Dassault Systemes Simulia Corp. ABAQUS ANALYSIS USER'S MANUAL, Ver. 6.9 2009. Providence, RI, USA.

26. Camanho P.P., Davila C.G., and Moura M.F., Numerical Simulation of Mixed-mode Progressive Delamination in Composite Materials. J. Compos Mats 2003; 37(16):1415-24.

27. Gao X. *Tailored Interphase Structure for Improved Strength and Energy Absorption of Composites*, Ph.D. Thesis, University of Delaware, USA. Spring 2006.

28. Turon A, Davila CG, Camanho PP, and Costa J, An engineering solution for mesh size effects in the simulation of delamination using cohesive zone models, Engineering Fracture Mechanics 74(2007) 1665-1682.

Chapter 4

ESTIMATING THE COHESIVE BEHAVIOR FROM FIBER TOPOLOGY

The use of cohesive contact behavior in a structural finite element model requires the specification of three parameters: stiffness, strength, and fracture toughness. In the preceeding chapter, a microscale FE microdroplet model with cohesive-based contact between the fiber and the droplet was detailed. The cohesive parameters were selected so that the simulated microdroplet response fits a particular experimental response. The objective in this chapter is to develop a method to predict the microscale cohesive parameters based on the nanoscale fiber surface topology. This objective is achieved by the development of an axisymmetric, nanoscale finite element model that represents the fiber-droplet interface mechanics including the fiber surface topology as well as the presence of an interphase. The nanoscale interface model is used to characterize the interfacial constitutive behavior and is, in turn, is used to estimate the effective cohesive contact behavior. The process of translating the nanoscale model results into the microscale cohesive contact definition is detailed in this chapter.

4.1 The Fiber-Droplet Interface

Scanning-electron microscopy (SEM) images of fiber surfaces with compatible GPS fiber sizing and a blended GPS-TEOS fiber sizing are shown in Fig. 4.1 (copied

with permission from [1]). The GPS-sizing surface topology appears relatively smooth and has an average absolute surface roughness of R_a = 6.4 nm. The blended fiber sizing possesses larger variations in surface topology and has an average absolute surface roughness R_a = 26.5 nm. Microdroplet experiments presented in [1-3] have determined that the IFSS and debond energy generally increases with surface roughness as shown in Fig. 4.2. A nanoscale finite element (FE) interface model is created to study the effect of the surface topography in combination with the interphase, on the effective microscale structural behavior.

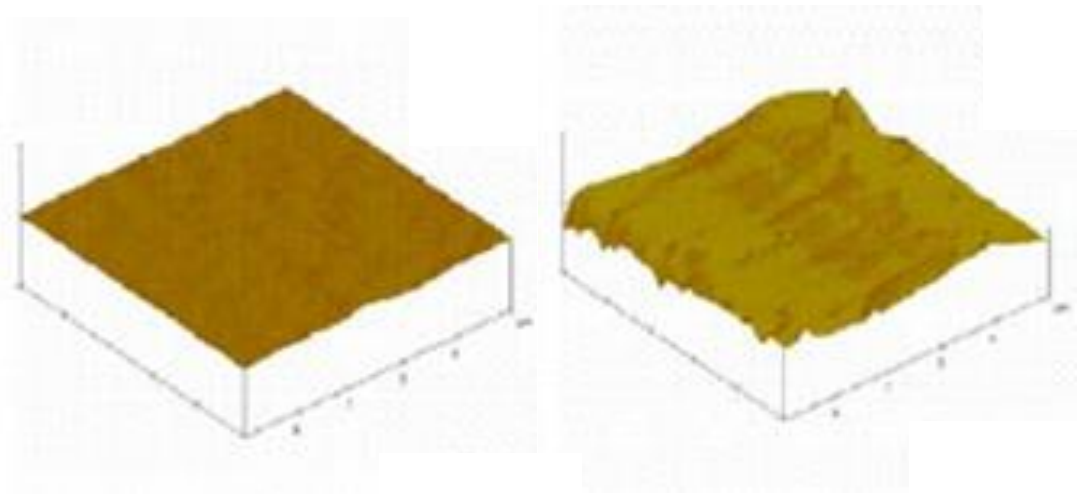

(a) (b)

Fig. 4.1. SEM images fiber surface with (a) 1% GPS sizing (R_a = 6.4 nm) and (b) 1% GT31 sizing (R_a = 26.5 nm). (images copied with permission from [1]).

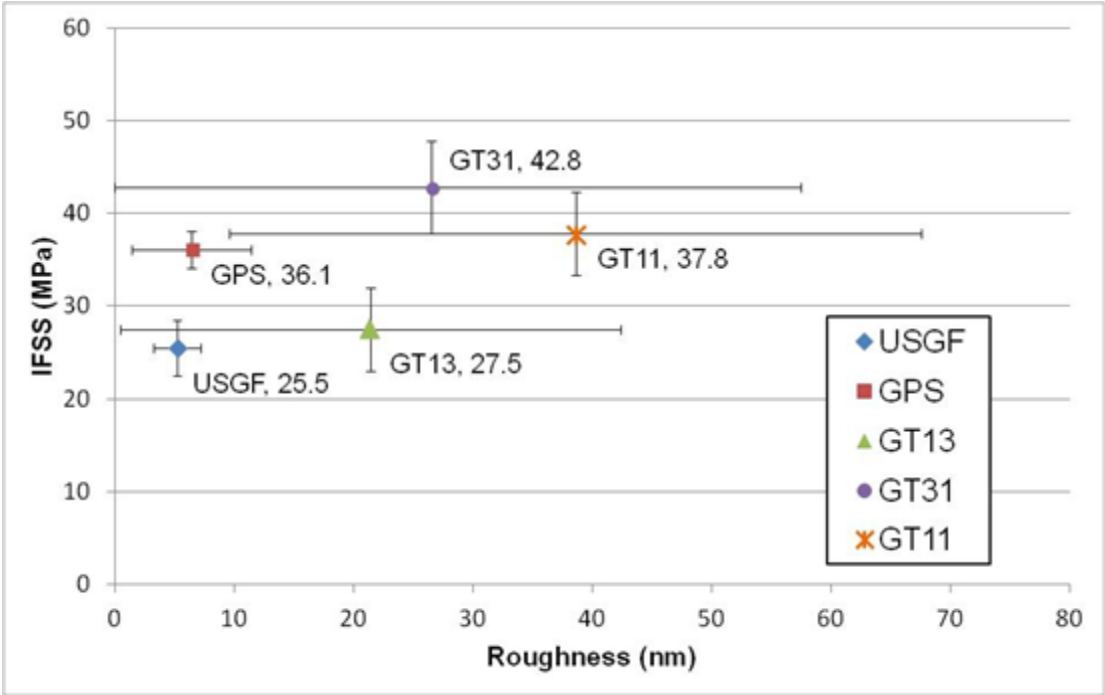

(a)

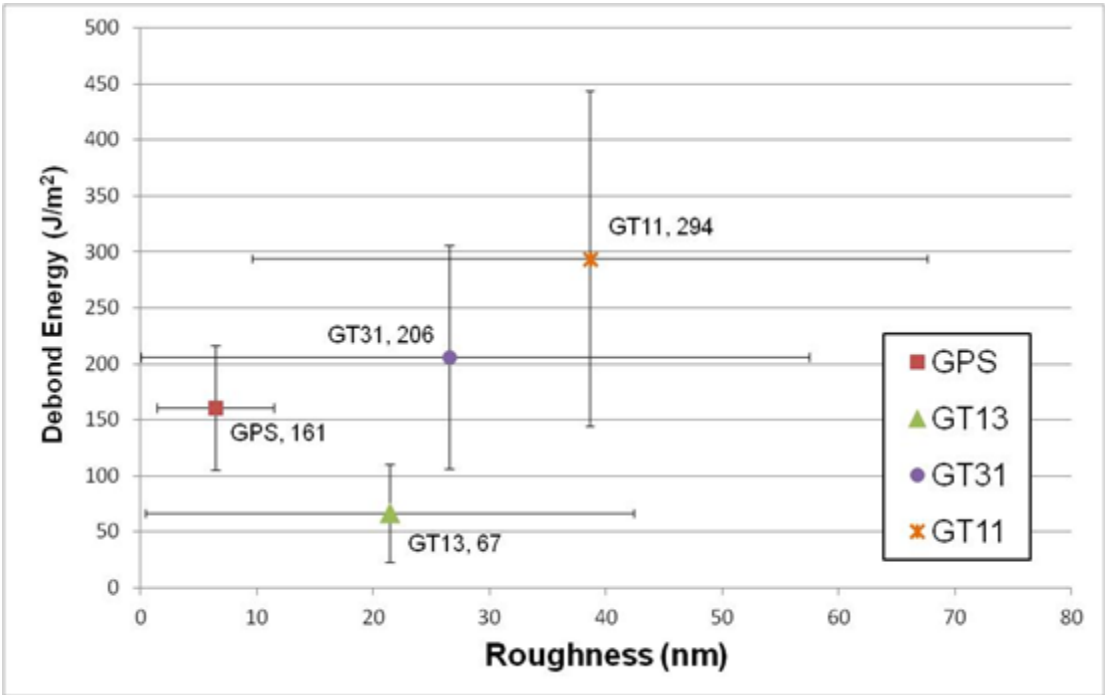

(b)

Fig. 4.2 Summary of (a) IFSS and (b) specific debonding energy results [1-3] for glass/epoxy microdroplet specimens with different fiber sizings (debond energy for unsized glass fiber (USGF) not reported).

4.2 The Nanoscale Interface FE Model

A microdroplet fiber-matrix FE model is developed to represent a characteristic segment of the interface with an estimated or assumed surface topography, i.e. surface roughness. The model's characteristic length scale is sub-micron and therefore it is referred to as the "nanoscale" interface model in the following. The nanoscale models investigated herein have an overall length along the fiber of 0.5 μm and 1.0 μm in the radial direction as shown in Fig. 4.3. Notice that only the outermost half micron of the glass fiber is modeled. This modeling approximation presumes that the center of the glass fiber undergoes uniform axial deformation during the microdroplet test, which is a reasonable approximation in the present case, since the elastic modulus of the glass fiber is an order of magnitude greater than the interphase and matrix elastic moduli.

In this study, the surface asperities on the fiber are modeled by the inclusion of a representative asperity that is securely bonded to the fiber. In practice, these asperities may be produced intentionally through mixing of fiber sizings [2] or by incorporating silica nanoparticles into the fiber sizing [3]. It may also be possible to achieve highly-engineered and precise fiber topography by embossing the fiber by passing it through a rotating die following the drawing of the fiber during its fabrication process. The glass fiber is modeled as an isotropic material with elastic parameters as shown in Table 4.1.

Different fiber topographies are investigated and are grouped herein as smooth, sinusoid, triangle, and rectangle. With the exception of the smooth fiber, each fiber topography type has two surface variants that are characterized by their maximum height, small (corresponding to 40 nm) and large (corresponding to 80 nm). The nanoscale,

axisymmetric models of the fiber topographies are shown in Fig. 4.4. The asperities are modeled as isotropic with elastic behavior similar to that of silica nanoparticles [3] as shown in Table 4.1.

In addition to the different fiber topographies, the influence of the interphase is studied by varying both its elastic modulus and thickness. In this work we prescribe either a compliant (E_i=2200 MPa) or stiff (E_i=4400 MPa) interphase elastic modulus relative to the bulk epoxy matrix (E_i=3200 MPa). Additionally, the interphase is assumed to be elastic-perfectly plastic with yield strength of 50 MPa. (The actual elastic modulus and yield behavior of the interphase is difficult to measure [4-10] so we use the stated numbers as representative values for this portion of the study.) The epoxy bulk matrix

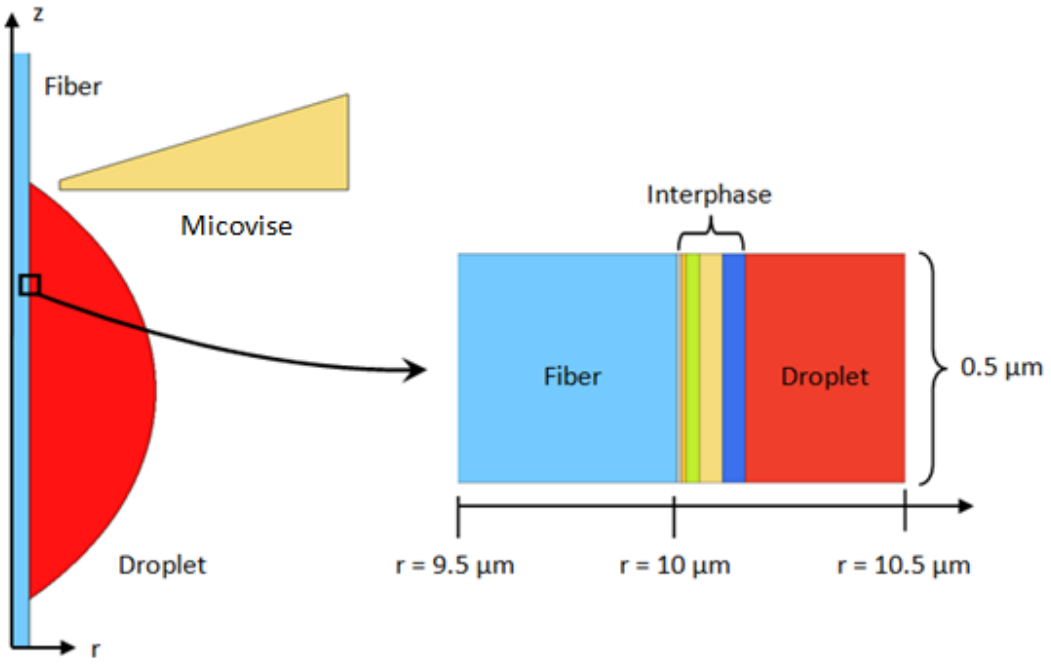

Fig.4.3. Microscale microdroplet model (left) of fiber-droplet interface and representative nanoscale model (right) of the fiber-droplet interface including the presence of an interphase.

and the interphase are assumed to be isotropic with elastic parameters shown in Table 4.1.

In this work we investigate four interphase thicknesses: 0 nm (i.e. interphase not present), 20 nm, 50 nm, and 200 nm, as shown in Fig. 4.5. The 20 nm interphase is comprised of the first two discrete bands of material adjacent to the fiber. Consequently, the matrix material is specified for the remaining bands. Similarly, the 50 nm interphase is comprised of the first three bands adjacent to the fiber and the 200 nm interphase is comprised of all five bands. The 20 nm and 50 nm interphases are conformal with the fiber-asperity while the thicker, 200 nm interphase, is assumed to be large enough to produce a constant radius interface with the bulk matrix.

The left edge of the nanoscale model is fixed in the both radial and axial directions for all analyses. The top and bottom edges of the nanoscale model have prescribed periodic boundary conditions so that the model simulates a representative segment of the interface, sufficiently far away from the top or bottom of the microdroplet,

$$u_x(r, z = 0\mu m) = u_x(r, z = 0.5\mu m) \tag{4.1}$$

$$u_z(r, z = 0\mu m) = u_z(r, z = 0.5\mu m)\ . \tag{4.2}$$

The interface properties in both tension and shear need to be specified, since the actual failure will be a combination of both modes [11-15]. The tensile behavior of the interface is modeled by pulling the outer, radial edge of the droplet in the radial direction (horizontally in Fig. 4.4) and constraining the axial (vertical) displacement of the outer, radial edge to be zero, i.e. $u_x(r_o = 10.5\mu m, z) = \alpha$ and $u_z(r_o = 10.5\mu m, z) = 0$ where α is the prescribed radial displacement. Although this is not a realistic mode of deformation

in an axisymmetric system, it is used to characterize the tensile properties of the particular fiber-interphase-matrix system on the nanoscale. This differs in comparison to the multi-axis loading produced during the microdroplet test where radial tensile and shear stresses develop along the fiber-matrix interface during the microdroplet test. Pisanova et al. [13] developed a tensile radial, i.e. "adhesional pressure," criterion for this multi-axis loading condition that relates the tensile radial stress magnitude to crack initiation using the variational mechanics solutions of Sheer and Nairn [14]. The shearing deformation behavior is simulated by pulling the outer, radial edge of the droplet in the axial direction (vertically in Fig. 4.4) and constraining the radial (horizontal) displacement of the outer edge, i.e. $u_x(r_o, z) = 0$ and $u_z(r_o, z) = \lambda$ where λ is the prescribed axial displacement.

Table 4.1. Elastic properties used in microdroplet and nanoscale models.

Component	Elastic Modulus (MPa)	Poisson's Ratio (-)	Yield Strength (MPa)
Glass Fiber	76000	0.22	
Asperity	80000	0.18	
Bulk Matrix	3200	0.35	50*
Interphase			
Stiff	4200	0.35	50
Compliant	2200	0.35	50

(* indicates yield strength of matrix when interphase is not present).

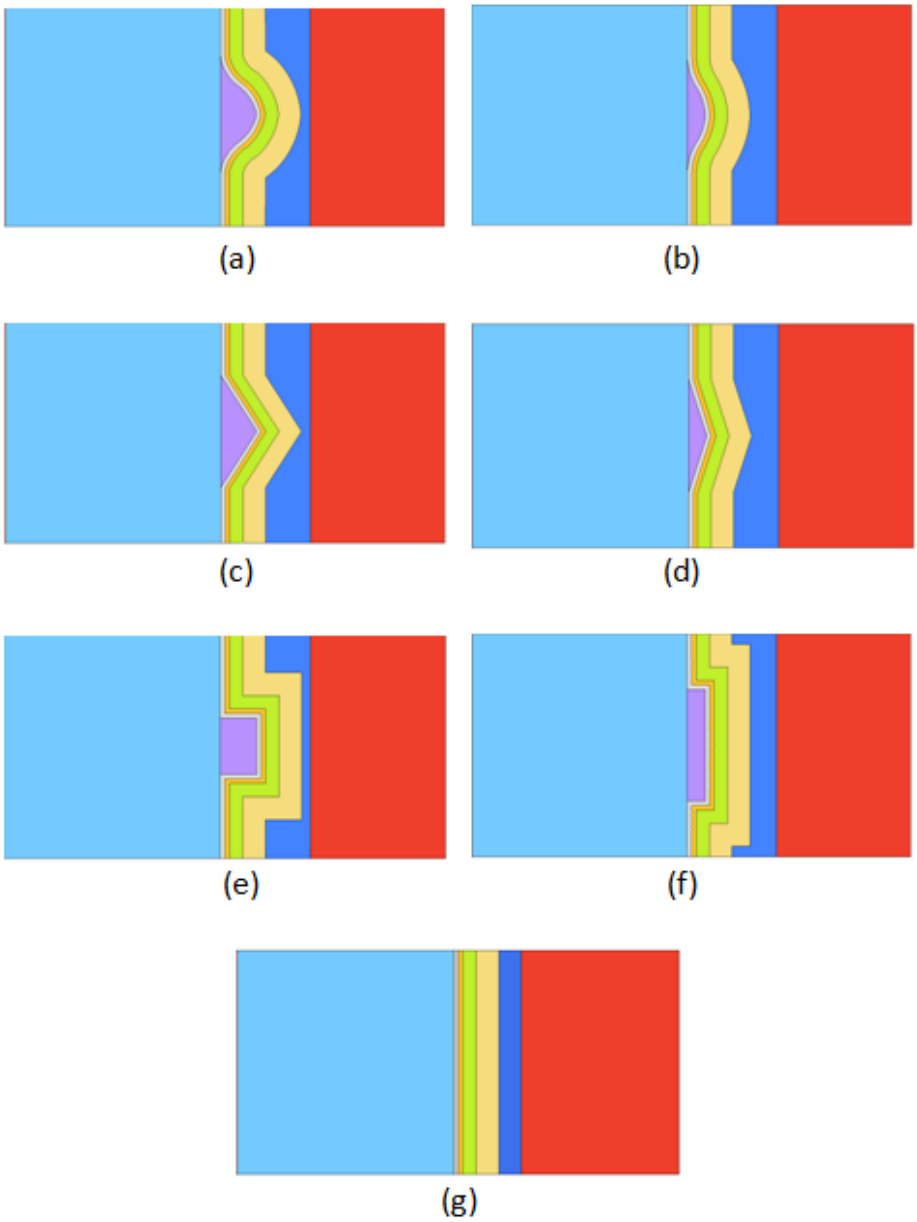

Fig. 4.4. Axisymmetric nanoscale interface models organized by their fiber topographies (a) large sinusoid and (b) small sinusoid, (c) large triangle and (d) small triangle, (e) large rectangle and (f) small rectangle, and (g) smooth fiber textures.

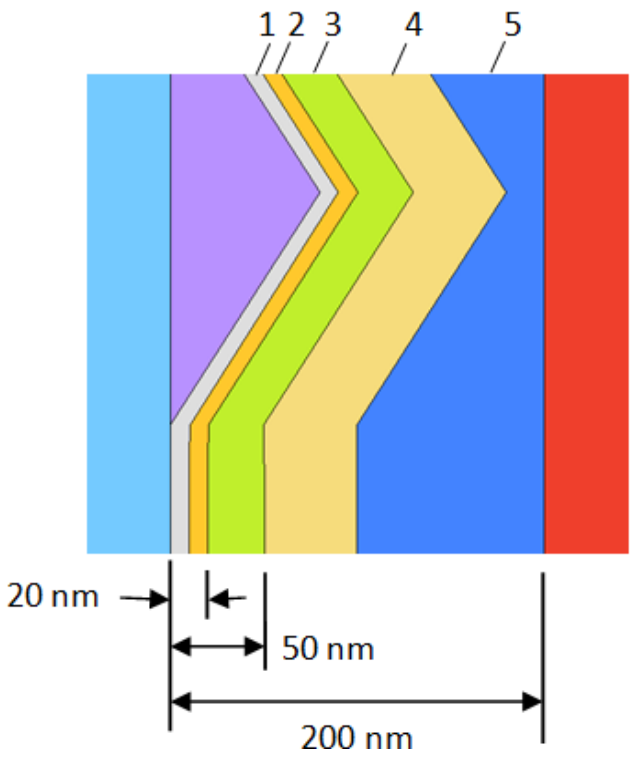

Fig. 4.5. Nanoscale model interphase systems. The 20 nm thick (bands 1-2) interphase and 50 nm thick (bands 1-3) interphase are conformal with the asperity (triangular shown) and the 200 nm thick (bands 1-5) interphase forms a constant radius boundary with the matrix.

4.3 Nanoscale Interface Model Results

Prescribing the appropriate boundary conditions on the nanoscale models as described previously in Section 4.2, the (reaction) force-displacement curves from these models are used to assess the effective structural behavior. As a representative example, the normal and shear force-displacement histories of the large sinusoid asperity model are shown in Fig. 4.6. Fig. 4.6(a) shows that the normal tensile response experiences only marginal softening post-yield; this is due to the periodic boundary conditions prescribed along the top and bottom edges of the nanoscale model that prevent the interphase and

bulk matrix materials from constricting in the fiber direction, (i.e. the Poison's effect, keeps the material in hydrostatic tension). Additionally, the normal tensile response is stiffer for both thinner interphases and larger interphase elastic moduli. Conversely, the shear response is not strongly dependent on the interphase elastic modulus as seen in Fig. 4.6(b). However, there is a distinct dependence of the shear response on the interphase thickness where thicker interphases effectively soften at lower applied shear forces.

Material failure is not included in the nanoscale model because the post-failure interactions between the newly created surfaces cannot be accounted for within the context of this model, i.e. the creation of new surfaces due to material failure is commonly achieved through element deletion resulting in a gap between the newly created surfaces which prevents load transfer by pressure and friction. Therefore in this study, failure is assumed when a continuous region of 2% equivalent plastic strain (or greater) has traversed the axial dimension of the nanoscale model. Other strain thresholds could be used as well, the choice of which will have an effect on the cohesive parameters. In this study, 2% is chosen since it is representative of strain to failure for neat epoxy [1]. Further, the path of the continuous equivalent plastic strain region is assumed to approximate the failure surface. As an example, the equivalent plastic strain contours for the large bump nanoscale models with compliant interphase (E_i=2200 MPa), are shown in Fig. 4.7. The left column shows tensile response, the right column shear, with the progressively thicker interphases shown moving down the column. The predicted failure surface profile is shown overlaid on the equivalent strain field from Fig.

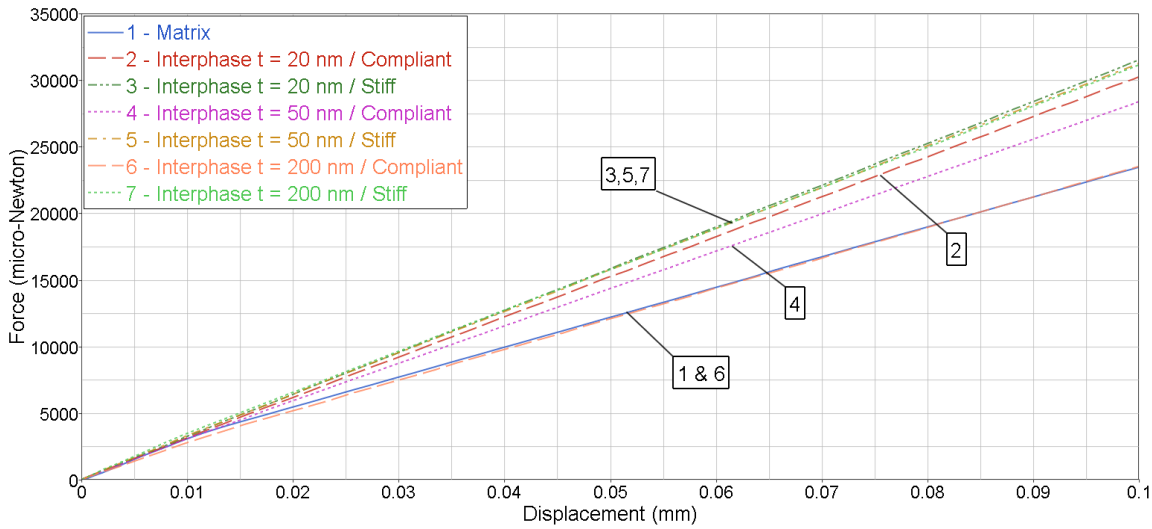

(a)

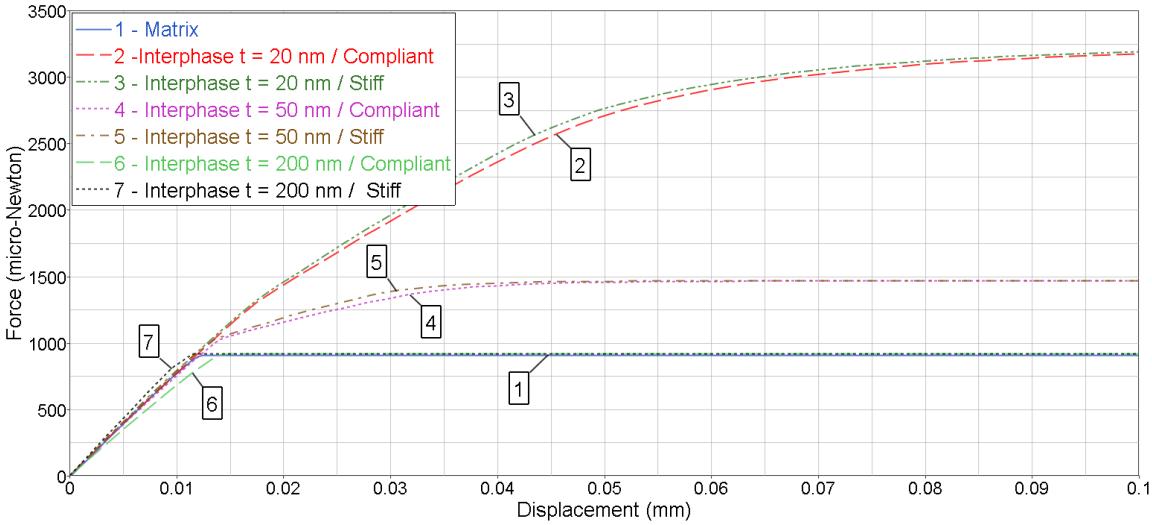

(b)

Fig. 4.6. Nanoscale interface model with large sinusoid asperity force-displacement histories for (a) normal deformation and (b) shear deformation.

4.7(d), in Fig. 4.8. The force magnitude at failure (shown in Fig. 4.8) depends on the choice of threshold strain and is taken as the critical force for the representative fiber segment in the model. The critical forces corresponding to this failure for the different systems tested at the 2% equivalent plastic strain threshold are summarized in Fig 4.9. An example of a failure surface profile is shown in Fig. 4.10. Analytically, the surface area S associated with this profile is estimated by integrating the surface of revolution via

$$S = 2\pi \int r(z)\sqrt{1+[r'(z)]}dz \tag{4.3}$$

where r is the radial position which is a function of the axial position z and the prime denotes the spatial derivative with respect to the axial coordinate z. The failure surface is numerically approximated by the nodal positions associated with the failure surface profile at the time of failure as

$$S \approx 2\pi \sum_{i=2}^{n} \frac{r_i - r_{i-1}}{2} \sqrt{1+\left[\frac{r_i - r_{i-1}}{z_i - z_{i-1}}\right]^2} (z_i - z_{i-1}) \tag{4.4}$$

where r_i and z_i are the radial and axial positions of node i, respectively. The failure surface areas for the different systems are computed for the different combinations of surface topography, interphase thicknesses, and interphase elastic moduli and will be used to interpret the nanoscale interface model results in the next section. Lastly, the nanoscale model results indicated that the strain fields were nearly identical for nanoscale systems that differed in interphase elastic modulus only. Consequently, the fracture surface areas predicted by Eq. (4.4) depend primarily on the fiber topography and the interphase thickness.

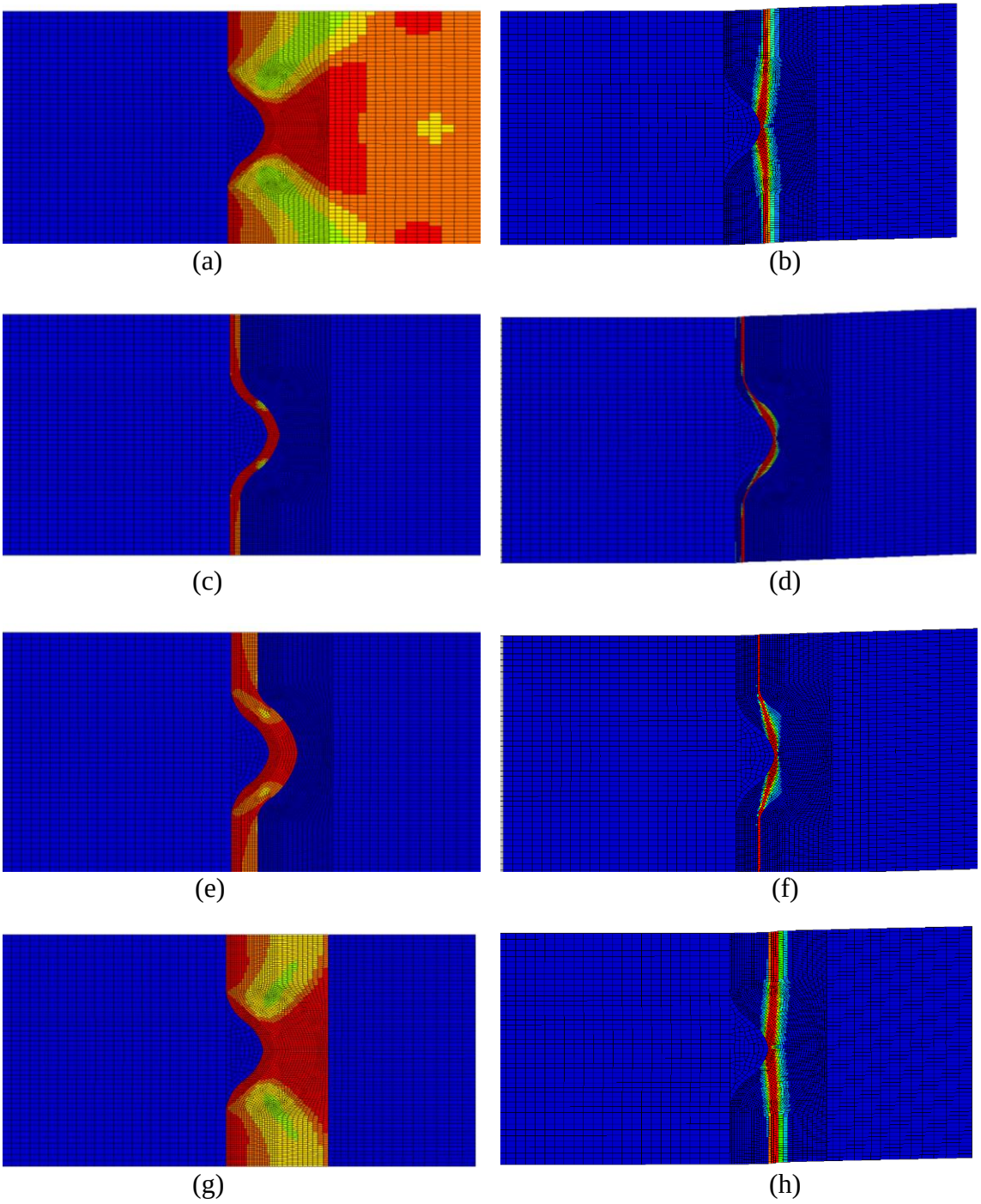

Fig. 4.7. Equivalent plastic strain fields for large bump topography nanoscale interface model with soft interphase. Normal tensile behavior (left column) and shear behavior (right column) (Interphase thickness t_i for a,b = t_i = 0 µm matrix only; c,d = t_i =0.020 µm; e,f = t_i =0.050 µm; g,h = t_i =0.200 µm).

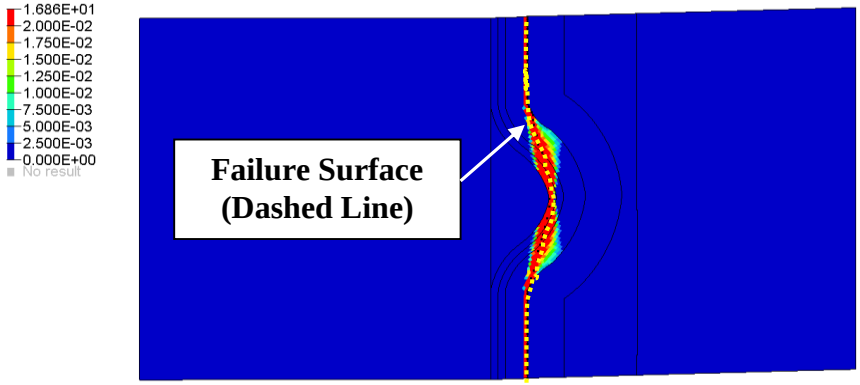

Fig. 4.8. Equivalent plastic strain contour plot of nanoscale interface model of large sinusoid fiber topography illustrating path of localized plastic strain and probable failure surface.

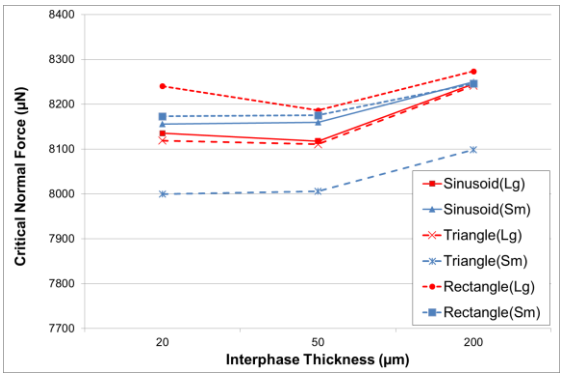

(a)

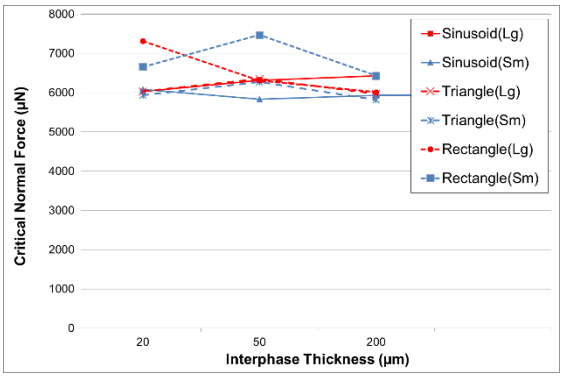

(b)

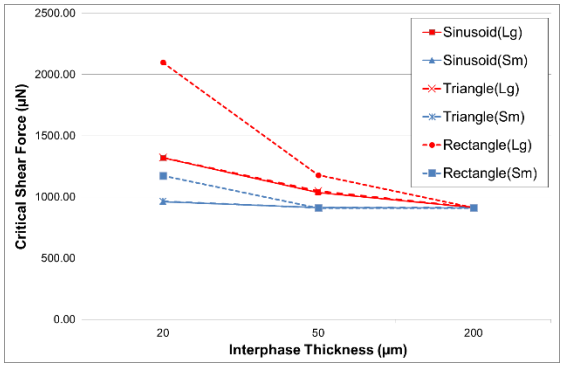

(b)

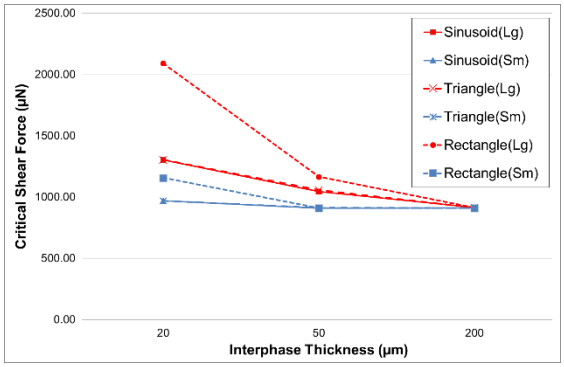

(d)

Fig. 4.9. Nanoscale critical force magnitudes for normal loading with (a) stiff interphase (b) compliant interphase, and shear loading with (c) stiff interphase and (d) compliant interphase.

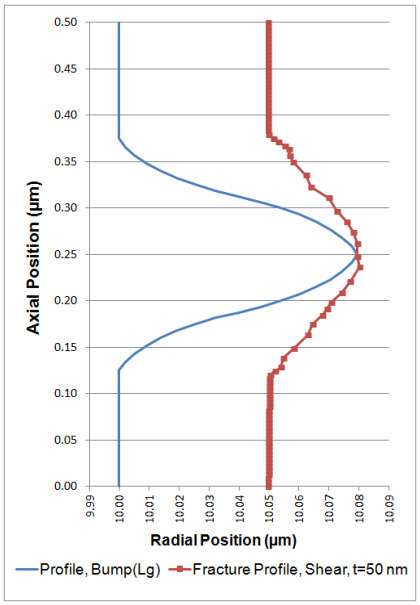

Fig. 4.10. Profile of large sinusoid asperity in comparison of estimate fracture surface profile for 50 nm thick, compliant interphase nanoscale interface model.

4.4 Nanoscale to Microscale Translation

The cohesive contact surface used in the microscale finite element model of the microdroplet is defined using a traction-separation behavior, which is illustrated in Fig. 4.11 for a single mode, i.e. normal or shear. The figure shows a schematic of the three critical parameters needed to fully define the cohesive element; stiffness K, strength σ, and toughness G. Values for each of these microscale cohesive parameters are estimated from the nanoscale model results summarized in Section 4.3 using the approach detailed in the following Subsections 4.4.1-4.4.3. In particular, the approach uses the critical force and displacement (shown in Fig. 4.12) corresponding to failure at the chosen threshold equivalent plastic strain and the estimated failure surface area as calculated by Eq. (4.4).

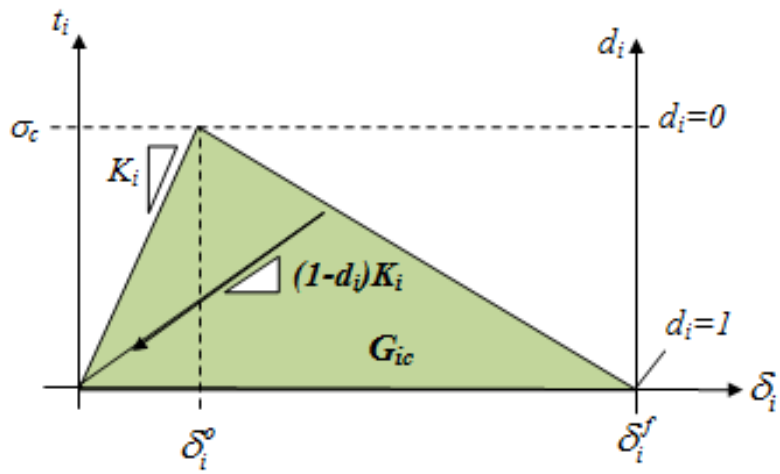

Fig. 4.11. Cohesive traction-separation (a) model for a single mode

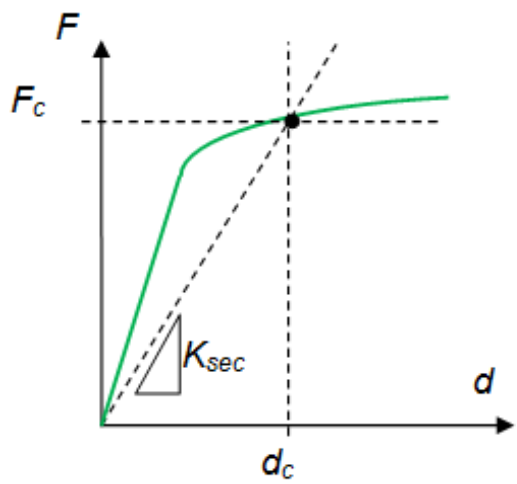

Fig. 4.12. Generic (absolute value) force-displacement history data from nanoscale interface model.

4.4.1 Cohesive Strength

As described in the previous sections, the interface in the nanoscale finite element model is assumed to have failed completely when a series of adjacent elements spanning the model have attained the threshold equivalent plastic strain value (2% or greater in the current study). Therefore the load magnitude in the normal or shear directions

corresponding to this state represents the critical normal or shear load, respectively. The effective strength is estimated by dividing the critical load by the surface area of the fiber segment in the FE model, i.e.

$$\bar{\sigma}_n = \frac{F_{cn}}{A} = \frac{F_{cn}}{\pi r_f l_c} \tag{4.5}$$

$$\bar{\sigma}_t = \frac{F_{ct}}{A} = \frac{F_{ct}}{\pi r_f l_c} \tag{4.6}$$

where $\bar{\sigma}$ is the average stress magnitude, F_c is the nanoscale model critical force, A is the base area, r_f is the fiber radius, l_r is the representative length of nanoscale model (i.e. 0.5 μm), and the subscripts n and t denote normal and shear directions, respectively. Note that the force is divided by the "neat" fiber surface area because the estimated effective strengths are a characteristic of the microscale microdroplet model which does not explicitly model fiber topography. The normal and shear cohesive strengths for the various fiber topographies with the elastically stiff interphase are shown as a function of interphase thickness in Fig. 4.13(a) and Fig. 4.13(b), respectively. Similarly, the normal and shear cohesive strengths for the elastically compliant interphase are shown in Fig. 4.14. The normal cohesive strengths are large due to the imposed periodic boundary conditions as explained previously. Even though the normal loading is not a realistic type of loading, the periodic boundary condition would be applicable at the interior of the droplet and become increasingly less valid as the volume under consideration approaches a free surface, i.e. where the fiber enters or exits the droplet.

For the elastically stiff interphase, the normal cohesive strength range is 255-265 MPa and is only slightly sensitive to the asperity geometry where taller asperities (those with greater height relative to the fiber surface) produce marginally larger normal cohesive strengths as shown in Fig. 4.13(a). For the elastically compliant interphase, the normal cohesive strengths range from 185-240 MPa and exhibit more scatter as a function of asperity geometry and interphase thickness as shown in Fig. 4.14(a). The normal cohesive strengths resulting from the compliant interphase are smaller compared to the strengths produced by the elastically stiff interphase. The shear cohesive strengths are range is 30-65 MPa and are nearly identical for both elastically stiff (Fig. 4.13(b)) and compliant (Fig. 4.14(b)) interphases. Additionally, the asperity geometry has an effect on the cohesive shear strength where the taller asperity geometries, relative to the interphase thickness produce increased strengths. This effect diminishes as the interphase thickness increases.

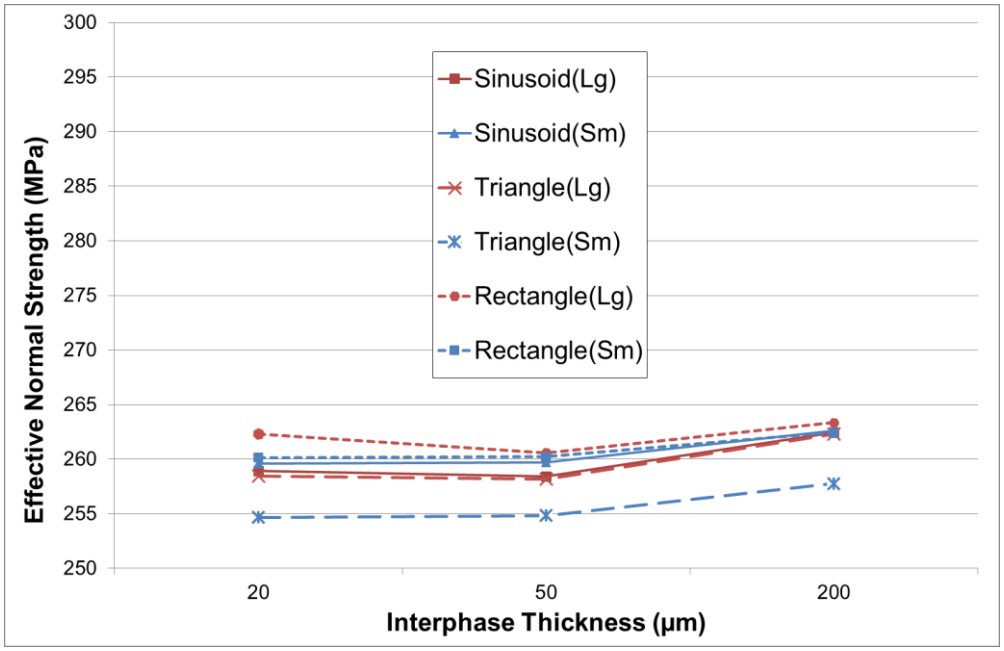

(a)

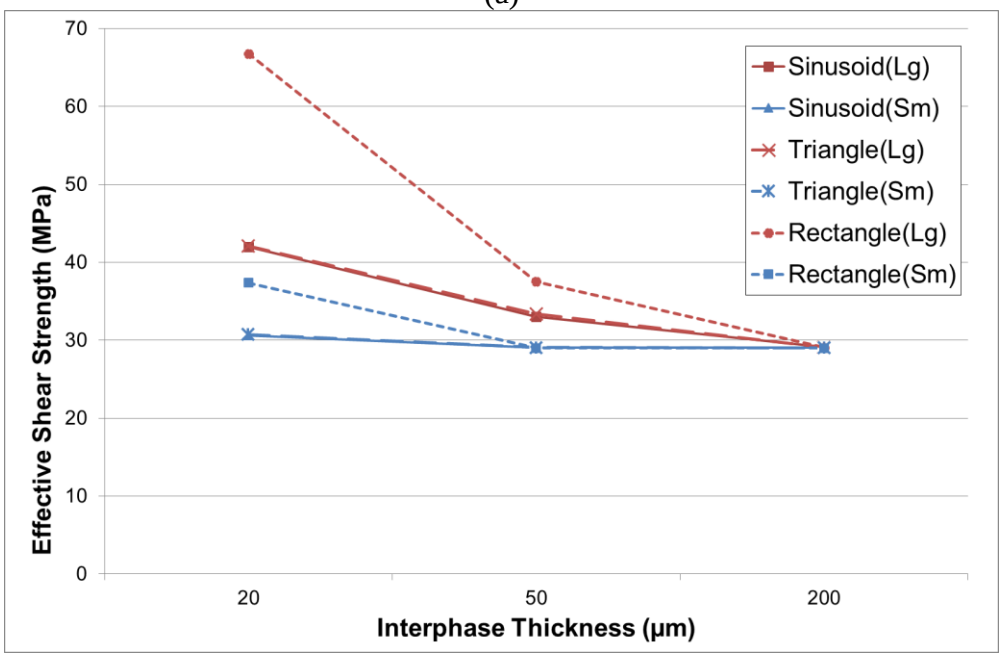

(b)

Fig. 4.13. The predicted cohesive strengths for the stiff interphase (E_i =4200 MPa) in the (a) normal and (b) shear directions for the different fiber topographies as a function of interphase thicknesses.

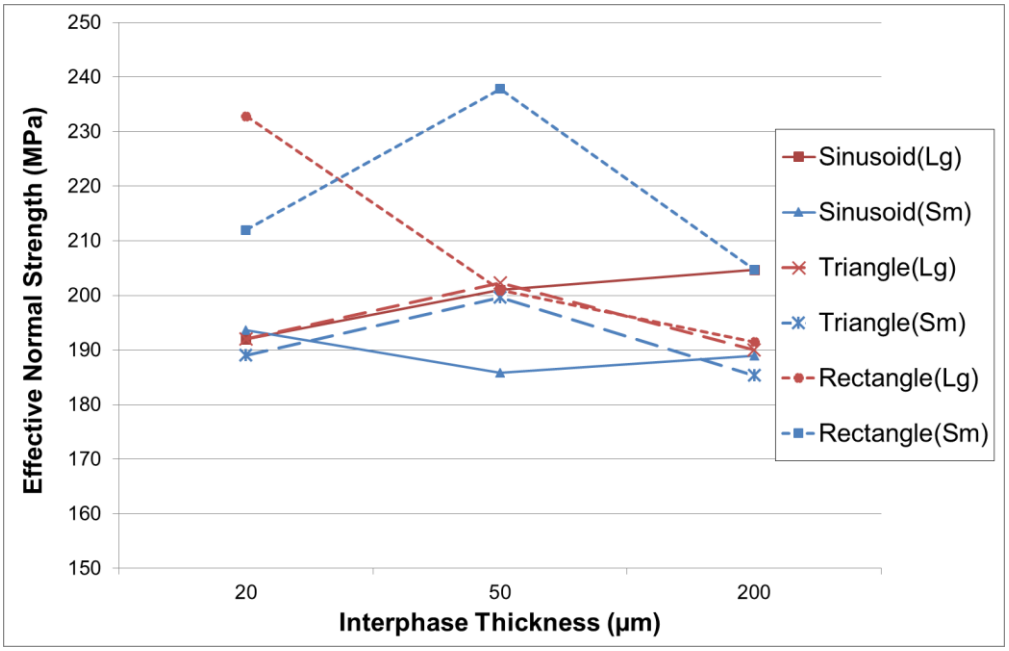

(a)

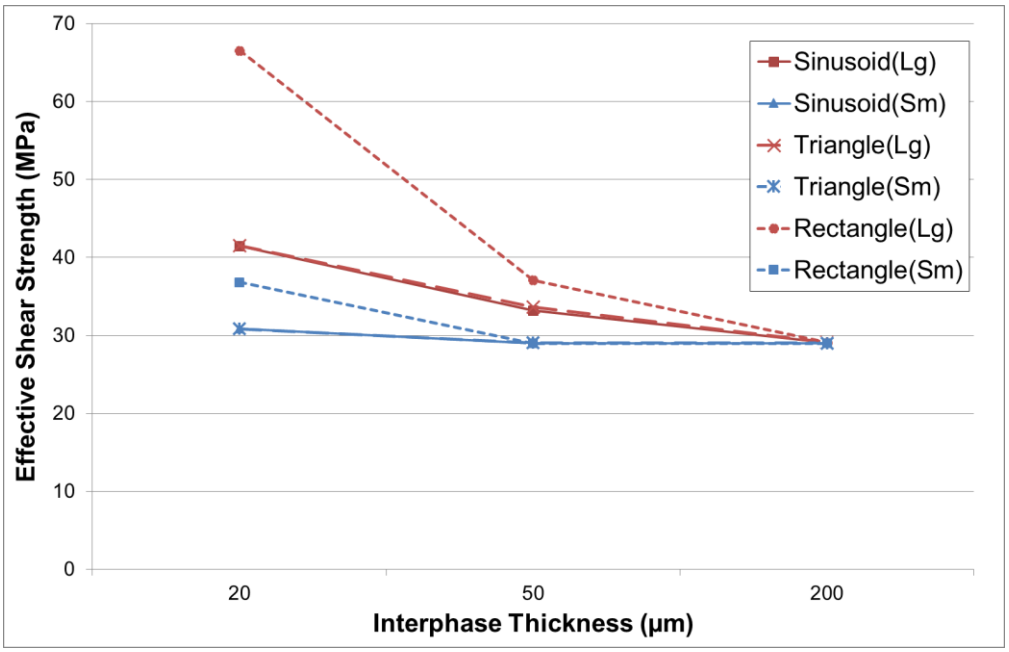

(b)

Fig. 4.14. The predicted cohesive strengths for the compliant interphase (E_i =2200 MPa) in the (a) normal and (b) shear directions for the different fiber topographies as a function of interphase thicknesses.

4.4.2 Cohesive Stiffness

The cohesive interface stiffness values for the cohesive zone in both the normal and shear directions can also be estimated using the nanoscale model. These stiffness values need to be sufficiently large to prevent an artificially softened response of the structure [17-18] and a value of 10^6 N/mm^3 (10^{15} Pa/m) is suggested in [18]. The nanoscale model is used to estimate the normal and shear behavior of the various fiber topographies and interphase definitions. The effective microdroplet model cohesive stiffness is expressed in terms of normal or shear stress per unit relative displacement between the matrix and fiber contact surfaces. The effective cohesive stiffness can be estimated by taking the secant modulus of the force-displacement curve, shown in Fig. 4.12, derived from the nanoscale model. The secant is taken to the load-displacement point corresponding to the normal or shear critical load and subsequently dividing by the fiber surface area, i.e.

$$K = \frac{1}{2\pi r_f l_r} \frac{F_c}{d_c} \tag{4.7}$$

where K is the cohesive stiffness in the normal or shear direction, r_f is the fiber radius, l_r is the representative length of nanoscale model (i.e. 0.5 μm), F_c is the critical force in the normal or shear direction and d_c is its corresponding displacement. The normal and shear cohesive stiffness values for the various fiber topographies with the elastically stiff interphase are shown as a function of interphase thickness in Fig. 4.15(a) and Fig. 4.15(b), respectively. Similarly, the normal and shear cohesive stiffness values for the elastically compliant interphase are shown in Fig. 4.16. The normal direction cohesive

stiffness values are 10.0-11.0 x 10^{15} Pa/m for the elastically stiff interphase and are insensitive to the interphase thickness. The cohesive shear stiffness values for the elastically stiff interphase range from approximately 8.0-10.0 x 10^{15} Pa/m and decrease as the interphase thickness increases as shown in Fig. 15(b). Lastly, the asperity geometry does not have a significant effect on the cohesive stiffness values when embedded in an elastically stiff interphase as the curves shown in Fig. 15 are approximately equivalent.

For the elastically compliant interphase, the normal cohesive stiffness values exhibit more scatter as a function of asperity geometry and interphase thickness and range in magnitude from 2.1-2.5 x 10^{15} Pa/m as shown in Fig. 4.16(a). However, the normal and shear cohesive stiffness values resulting from the compliant interphase are smaller than the stiffness values for the elastically stiff interphase. Additionally, the asperity geometry has an effect on the shear stiffness where the taller asperity geometries, relative to the interphase thickness, produce higher shear stiffness as shown in Fig. 4.16(b). The effect of the asperity geometry is seen to diminish as the interphase thickness increases resulting in a decreases in shear stiffness.

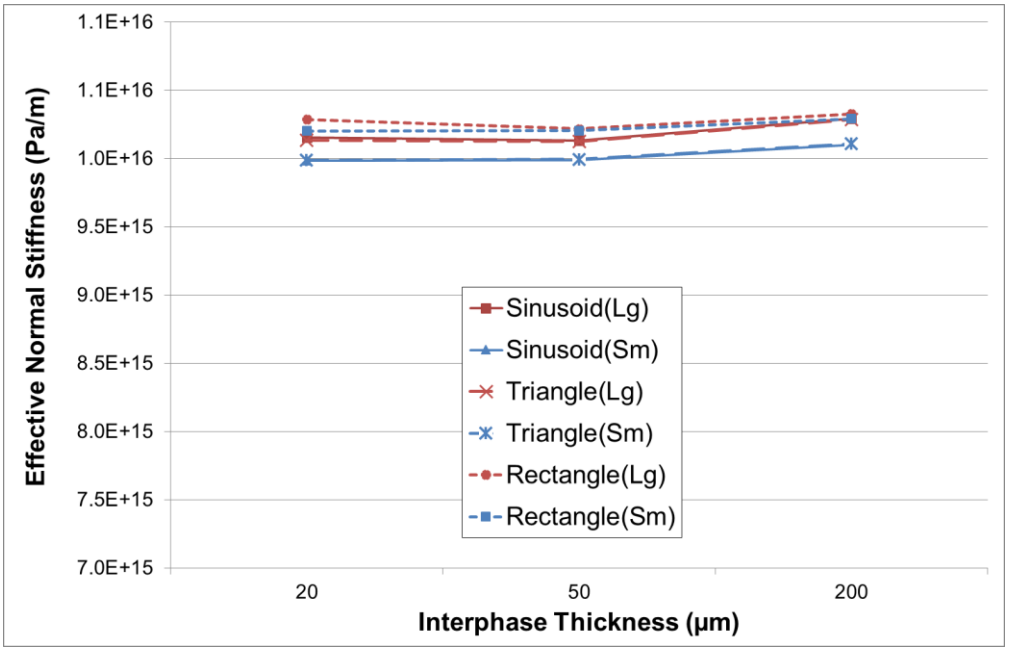

(a)

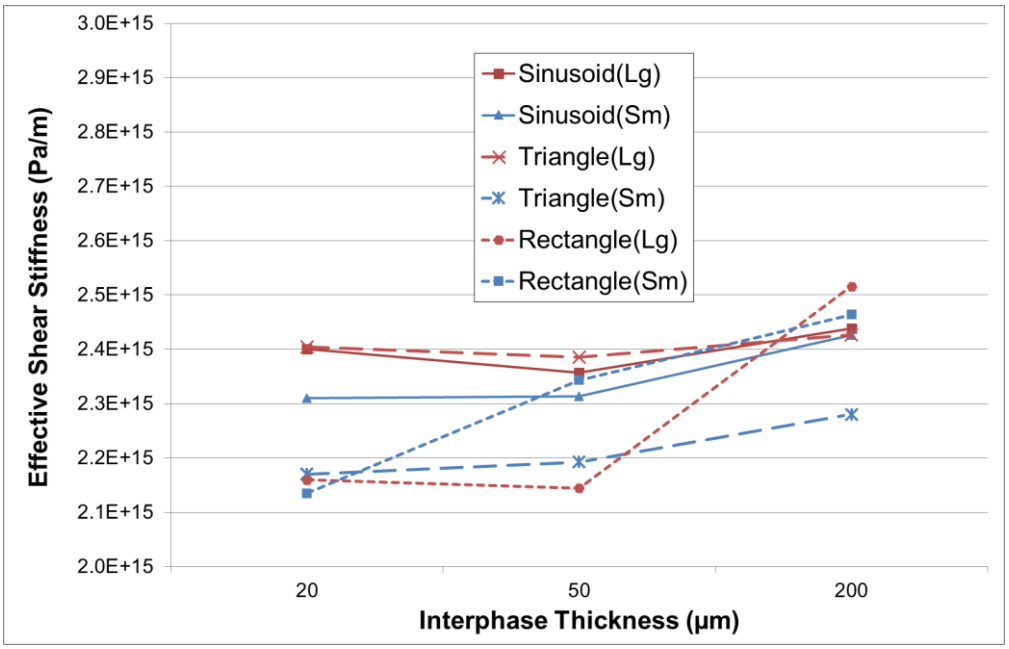

(b)

Fig. 4.15. The predicted cohesive stiffness values for the stiff interphase (E_i =4200 MPa) in the (a) normal and (b) shear directions for the different fiber topographies as a function of interphase thicknesses.

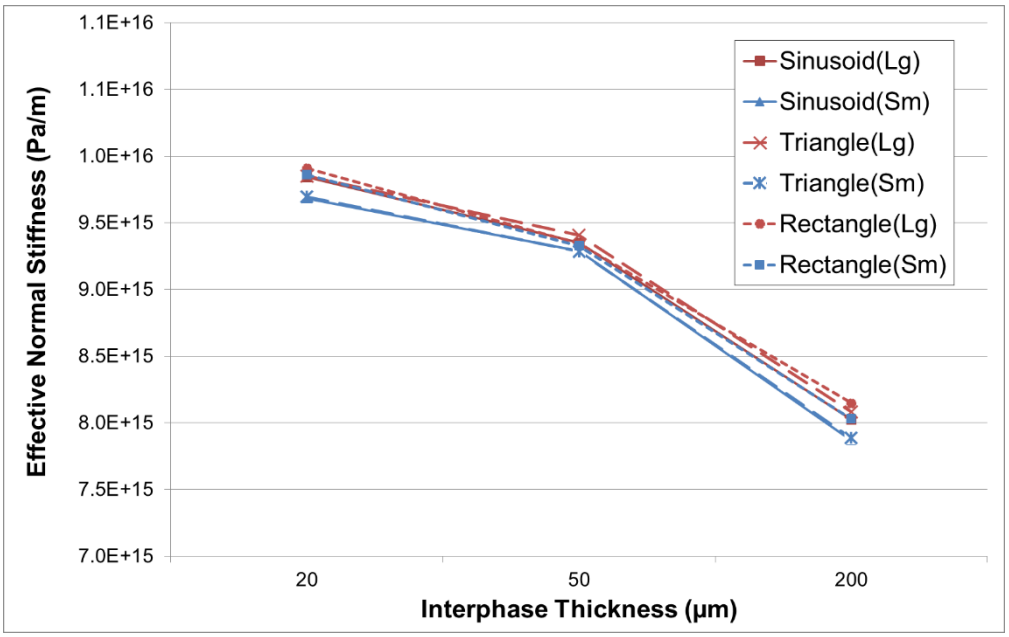

(a)

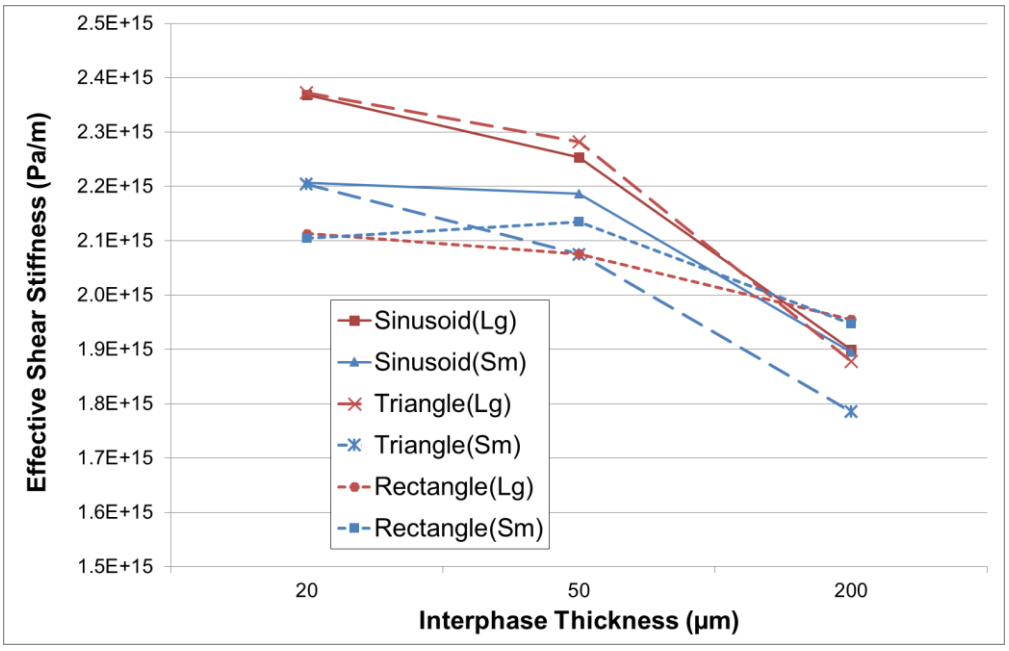

(b)

Fig. 4.16. The predicted cohesive stiffness values for the compliant interphase (E_i =2200 MPa) in the (a) normal and (b) shear directions for the different fiber topographies as a function of interphase thicknesses.

4.4.3 Cohesive Toughness

The third parameter needed for the cohesive definition in the microdroplet model is the fracture toughness. The fracture toughness or the fracture energy release rate is the energy dissipated per unit area of newly created fracture surface. Consequently, to characterize toughness on the size scale of the interface, we use the fracture surface area predicted by the nanoscale model. The effective fracture toughness of the interface in the microdroplet model is estimated by scaling the assumed fracture toughness of the interphase material (used in the nanoscale simulation) by the area of the failure surface calculated from the nanoscale simulation (Eq. (4.4)) normalized by the fiber surface area. For example, we assume that the fracture energy of both the matrix and the interphase materials used in the nanoscale model is 180 J/m^2 in both normal and shear directions, i.e. the assumed fracture energy is the same for Mode I and Mode II. The effective fracture toughness is then the product of the assumed nanoscale fracture energy and the predicted fracture surface area normalized by the fiber surface area. This is computed as

$$\overline{G} = G_0 \frac{S}{S_o} = G_0 \frac{S}{2\pi r_f l_r} \tag{4.8}$$

where S is the area of the revolved fracture surface (from Eq. (4.4)), r_f is the fiber radius, l_r is the nanoscale model representative length (0.5 μm), and G_0 is the assumed fracture toughness of the material in the nanoscale model (G_0=180 J/m^2). Our results show that the failure surface profile is independent of the interphase elastic modulus.

Consequently, for a given asperity geometry, the predicted cohesive fracture toughness values are the same for either an elastically stiff or compliant interphase.

The normal and shear cohesive toughness values for the various fiber topographies are shown as a function of interphase thickness in Fig. 4.17(a) and Fig. 4.17(b), respectively. The normal direction cohesive toughness values are 188-245 J/m^2 and the shear direction cohesive toughness values are 181-194 J/m^2. The normal direction cohesive toughness generally increases as the interphase thickness increases and the asperity height, increases. Conversely, the shear direction cohesive toughness decreases with increasing interphase thickness. Lastly, the asperity geometry contributes to the shear direction cohesive toughness where taller asperity geometries, produce greater fracture toughness values, particularly for thin interphase thicknesses. However, the actual shape of the asperity is less significant as the three taller (h=80 nm) asperity geometries generate approximately the same fracture toughness, and similarly, the three shorter (h=40 nm) asperity geometries generate nearly the same fracture toughness.

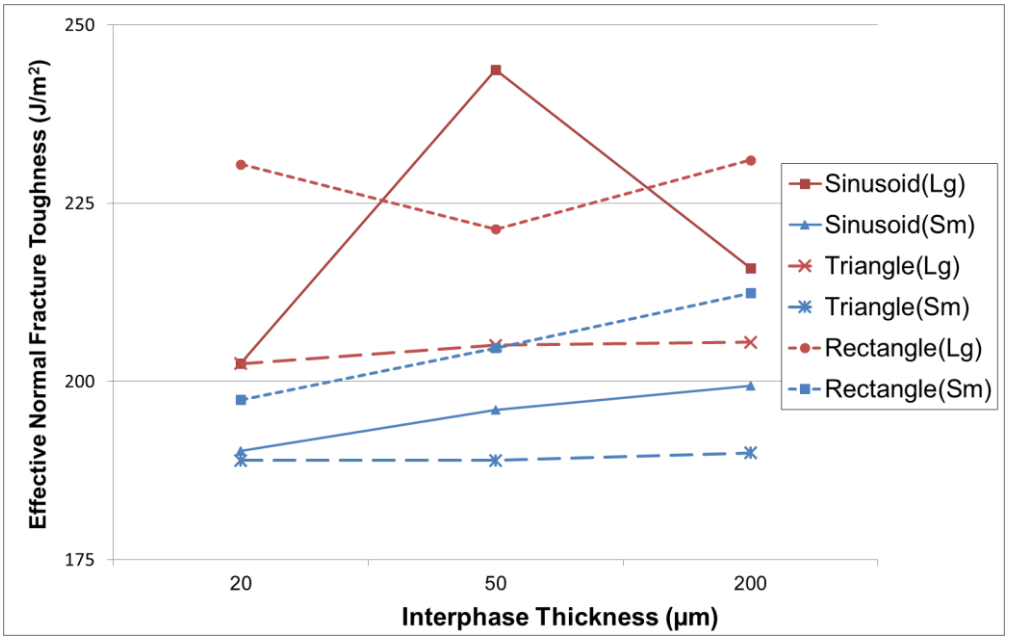

(a)

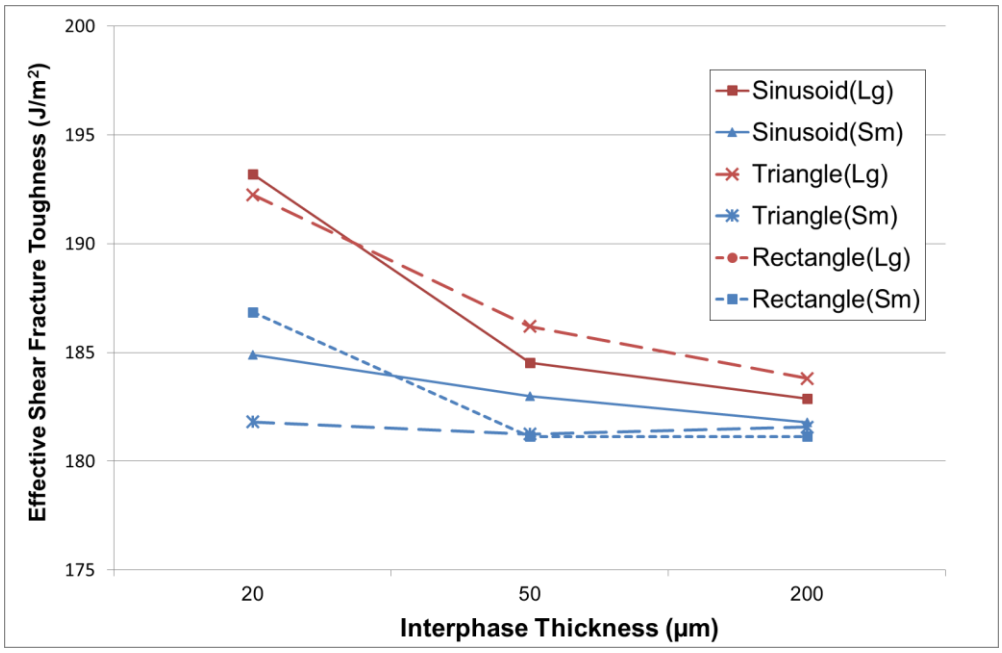

(b)

Fig. 4.17. The predicted cohesive fracture toughness values in the (a) normal and (b) shear directions for the different fiber topographies as a function of interphase thickness.

The process for converting the nanoscale model results to microscale cohesive parameters presented in this section is shown graphically in Fig. 4.18. Using this process, the predicted microdroplet model cohesive parameters for the various fiber topographies and interphase definitions are summarized in Fig. 4.13-4.17. The following trends are noted:

- The normal mode strength is significantly greater than the 50 MPa yield stress assumed in the nanoscale model and this increase is due to the periodic boundary conditions applied in the nanoscale model.
- The interphase thickness has little influence on the normal mode strength but significant influence on the shear mode strength. The thinner the interphase, the greater the effective shear mode strength.
- The interphase elastic modulus has a significant effect on the normal mode strength but very little effect on shear mode strength.
- The fiber topography has little influence on the normal mode strength but it has considerable influence on the shear mode strength. A greater asperity height correlates to greater shear mode strength.
- The effective normal mode stiffness shows a dependence on the interphase thickness and modulus. The dependence decreases as the interphase thickness decreases. The effective shear mode stiffness is not strongly influenced by the interphase thickness or the modulus of the interphase for interphase thicknesses less than the asperity height.
- The effective toughness increases with increasing asperity maximum height, particularly in the normal mode. Less than 10% increase in shear mode toughness is seen for the different fiber topographies and interphase definitions studied.

Nanoscale Interface Model

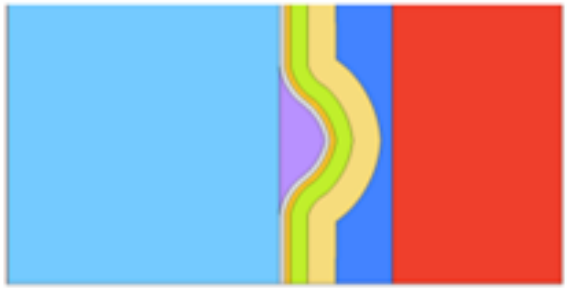

Nanoscale Interface Model Parameters

Interphase Elastic Modulus E_i

Interphase Yield Strength Y_i

Interphase Failure Plastic Strain ε^{pl}

Interphase Thickness t_i

Asperity Geometry

FE Analysis

Equivalent Plastic Strain Field

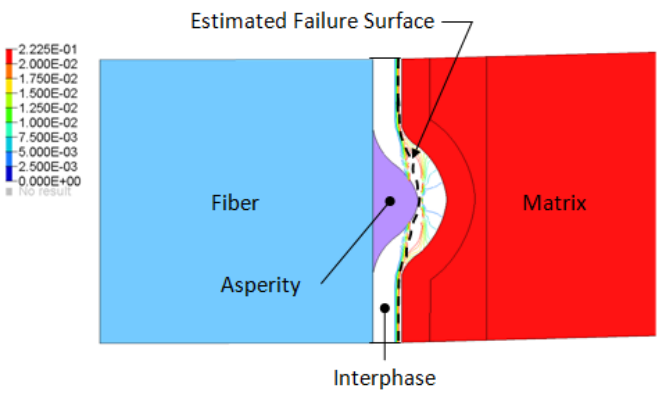

Force-Displacement Response

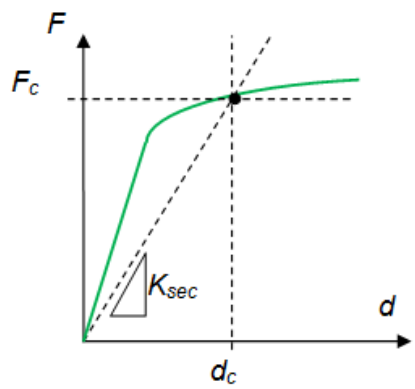

Critical displacement d_c and force F_c correspond to point when equivalent plastic strain field traverses nanoscale model with a magnitude equal to the threshold failure strain. The area of failure surface is approximated using

Failure Surface $$S \approx 2\pi \sum_{i=1}^{n} \frac{(r_i + r_{i-1})}{2} \sqrt{1 + [r'(z)]^2}\, \Delta z_i$$

The microdroplet cohesive parameters are estimated by

Cohesive Stiffness $$K = \frac{1}{2\pi r_f l_r} \frac{F_c}{d_c}$$

Cohesive Strength $$\bar{\sigma} = \frac{F_c}{A} = \frac{F_c}{2\pi r_f l_e}$$

Cohesive Fracture Toughness $$\bar{G} = G_0 \frac{S}{S_o} = G_0 \frac{S}{2\pi r_f l_r}$$

Fig 4.18. Summary of nanoscale-to-microscale translation process to estimate cohesive parameters.

4.5 Microdroplet Response with Predicted Cohesive Behavior

The cohesive strength, stiffness, and toughness values predicted using the nanoscale model are used to specify the cohesive behavior parameters in the axisymmetric microdroplet model detailed in Chapter 3 with the exception that the fiber embedded length and droplet diameter is 150 μm (rather than 136 μm as reported in Chapter 3). The microdroplet simulations are used to assess the effect of the cohesive behavior on the overall force-displacement behavior. The force-displacement responses for simulations 1 and 2 of Table 4.2 which examine the effect of asperity size are shown in Fig. 4.19(a).The simulation shows that larger asperity geometries relative to the interphase thickness produces greater peak force. However, the magnitude of the peak force decreases as the interphase thickness is increases as shown in Fig. 4.19(b). These show that the cohesive definitions associated with the non-smooth fibers result in increased loads in the microdroplet test; in agreement with published experimental results [2-3]. Additionally, the microdroplet simulations indicate that the range of cohesive stiffness values investigated herein has little effect on the microdroplet force-displacement behavior as evidenced by the family of sinusoid asperity curves; the initial slope of the force-displacement curves are nearly identical regardless of asperity type and size, and regardless of interphase thickness and interphase stiffness. It was expected that the interphase elastic modulus would have an effect on the microdroplet model since it has been shown to have an effect on the structural behavior of composites [6, 10, 16]. However, unlike in the reference [10] where the interphase elastic modulus varied by an order of magnitude, the interphase modulus used in the nanoscale models here, differed

by less than 32% and the corresponding cohesive stiffness values (which represent the interphase's elastic modulus in the microdroplet model) varied by less than 25%, accounting for fiber topography, interphase elastic modulus, and interphase thickness.

The effects of thermally induced residual stress for the cohesive behaviors defined in Table 4.2 are presented in Fig. 4.20. A radial compressive residual stress is produced in the model by prescribing a change in temperature of -125 °C and defining a fiber coefficient of expansion of 8.8×10^{-6} m/m-°C and a droplet coefficient of expansion of 55.0×10^{-6} m/m-°C which are comparable to the values used in earlier numerical modeling of glass fibers and epoxy droplets [5, 11, 13, 15]. As shown in Fig. 4.20, residual stress increases the magnitude of the post-failure, steady-state pullout load. Comparison of Fig. 4.19 and Fig. 4.20 reveals that the for the cohesive behaviors defined in Table 4.2 and the defined microdroplet geometry, residual stress has little effect on force response when the size of the asperity is smaller than the interphase thickness. The residual stress reduces the peak load sustained during the microdroplet test when the size of the asperity geometry the is larger than the interphase thickness which produces a significantly larger residual stress in the interphase material that brings it closer to yield at the beginning of the analysis.

Table 4.2. Cohesive behavior parameter sets used in the microdroplet model

Simulation	Interface Asperity(Size)/Modulus/Thickness	S_n (MPa)	S_t (MPa)	K_n (10^{15} Pa/m)	K_t (10^{15} Pa/m)	G_n (J/m^2)	G_t (J/m^2)
1	Sinusoid(Lg) / t=20 nm	192	41	9.84	2.37	202.5	193.2
2	Sinusoid(Sm) / t=20 nm	194	31	9.68	2.21	190.3	181.8
3	Sinusoid(Lg) / t=200 nm	205	29	8.03	1.90	215.9	182.9

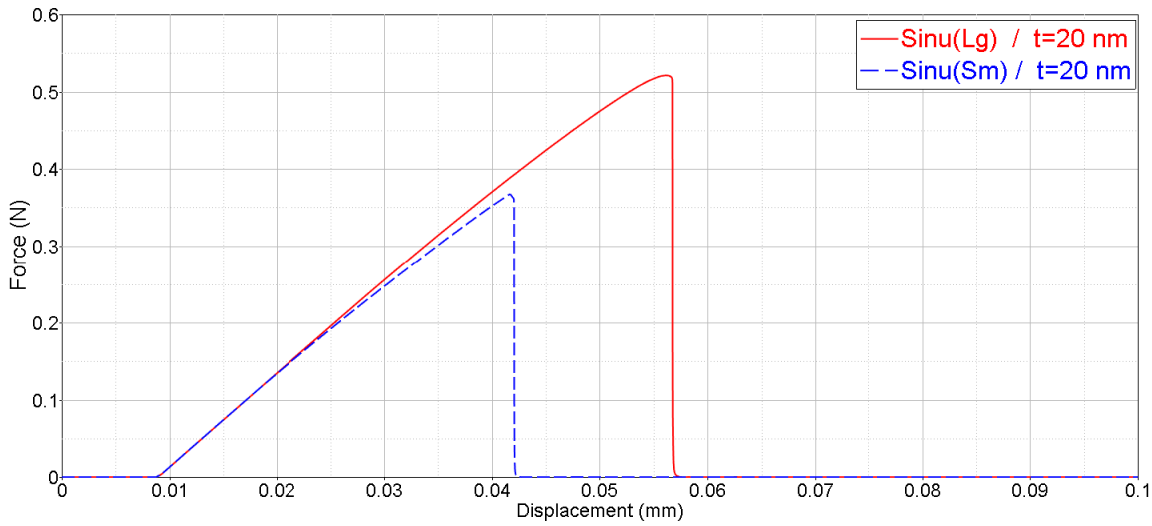

(a)

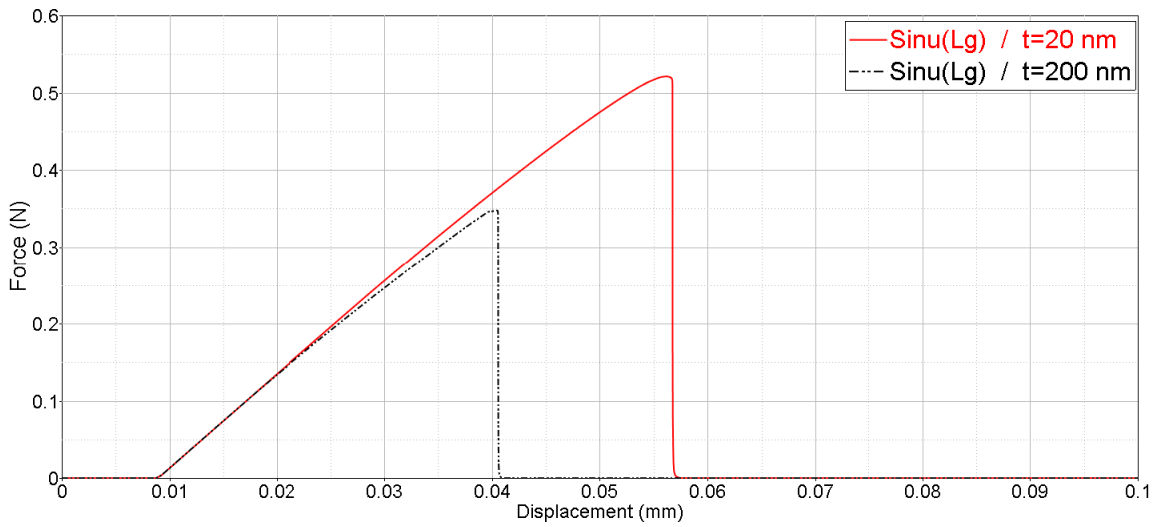

(b)

Fig. 4.19. Microdroplet force-displacement responses without thermal residual stress and (a) large and small sinusoid asperity geometries with thin (t=20 nm) interphase thickness and (b) large sinusoid asperity geometry for thin (t=20 nm) and thick (t=200 nm) interphase thicknesses.

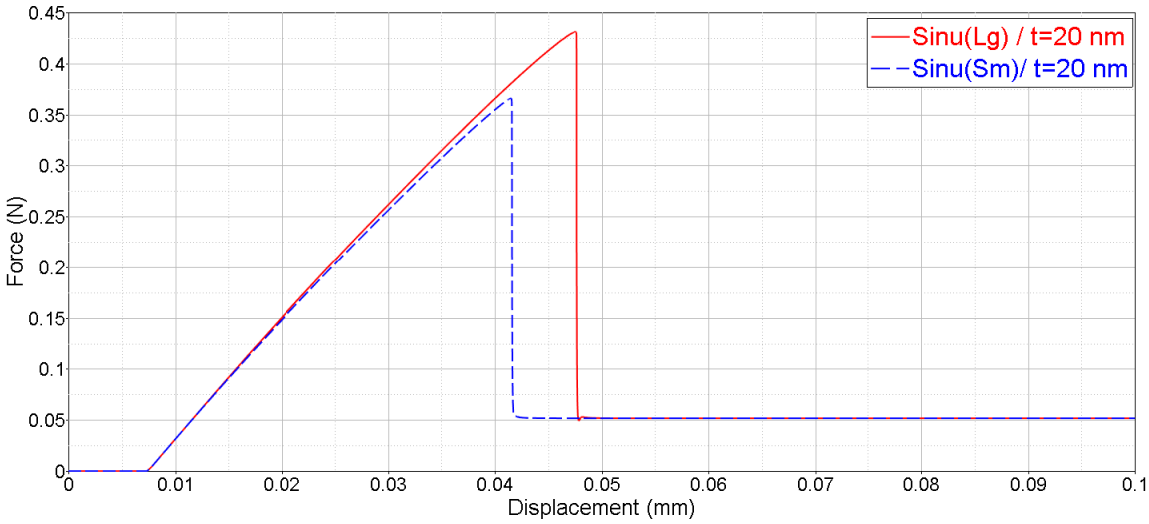

(a)

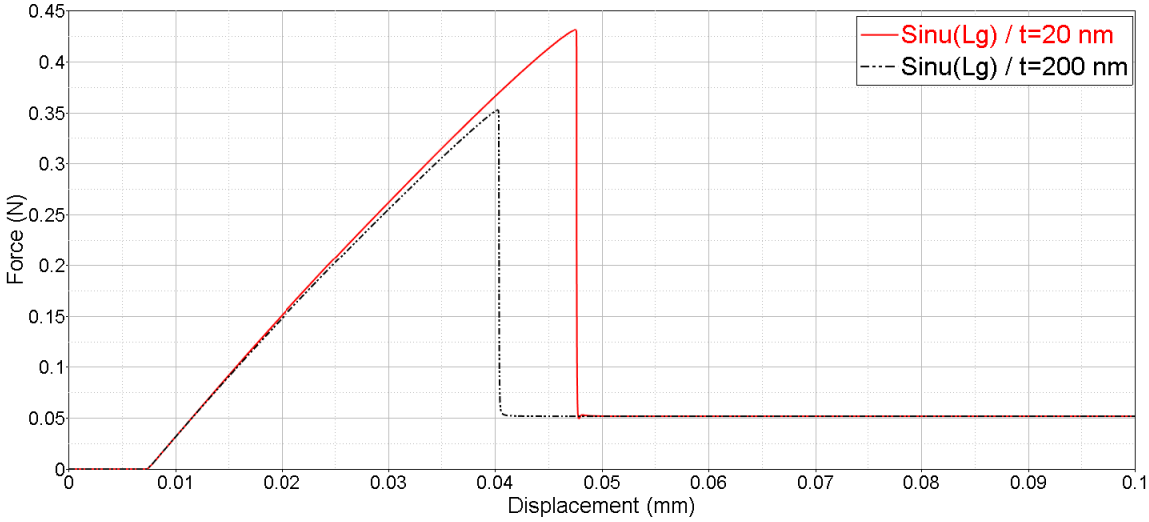

(b)

Fig. 4.20. Microdroplet force-displacement responses with thermal residual stress and (a) large and small sinusoid asperity geometries with thin (t=20 nm) interphase thickness and (b) large sinusoid asperity geometry for thin (t=20 nm) and thick (t=200 nm) interphase thicknesses.

4.6. Summary

A nanoscale model of the fiber-interphase-matrix system with various fiber sizing topographies, modeled as an asperity fixed to the fiber, shows that the asperity height relative to the interphase thickness affects the predicted cohesive behavior. The effects of the interphase thickness and elastic modulus are studied and the nanoscale model indicates that the interphase elastic modulus is the dominant parameter affecting the normal direction interfacial behavior and that the interphase thickness, in combination with the fiber topography, i.e. height, has a significant effect on the shear mode behavior.

Additionally, a process to estimate the effective parameter values needed to define the cohesive contact behavior (stiffness, strength, and fracture toughness) for a microscale, microdroplet model, is developed using the critical nanoscale model force-displacement results and the predicted fracture surface. The nanoscale model predicts that the fiber topography has little influence on the normal mode cohesive strength and stiffness parameters. However, the topography does affect the deformation behavior and therefore the plastic strain and hence, the fracture energy as it is estimated in this work. Since the microdroplet test is dominated by the fiber-droplet shear response, the fiber topography has a large influence on its force response. As the fiber topography roughness increases, i.e. larger asperity heights, its effective shear strength, stiffness, and fracture toughness increase, consistent with experimental results seen in the literature [1-3]. Conversely, the cohesive parameters, particularly the shear direction parameters, generally decrease with increasing interphase thickness for a given asperity geometry and interphase elastic modulus.

REFERENCES

1. Gao X. *Tailored Interphase Structure for Improved Strength and Energy Absorption of Composites*, Ph.D. Thesis, University of Delaware, USA. Spring 2006.

2. Gao X., Jensen RE, Li W., Deitzel, McKnight SH, Gillespie Jr JW. Effect of fiber surface texture created from silane blends on the strength and energy absorption of the glass fiber/epoxy interphase, J. Compos Mats, 2008, 513-534.

3. Gao X, Jensen RE, McKnight SH, Gillespie Jr JW. Effect of colloidal silica on the strength and energy absorption of glass fiber/epoxy interphases. Compos A, Appl Sci Manuf 2011; 42(11): 1738–47.

4. Tanoglu M, Ziaee S, McKnight SH, Palmese GR, Gillespie Jr JW. Investigation of properties of fiber/matrix interphase formed due to the glass fiber sizing. J. Mat Sci., 2001; 26:3041-3053.

5. Maligno AR, Warrior NA, Long AC. Effects of interphase material properties in unidirectional fibre reinforced composites. Compos Sci Technol., 2010; 70:36-44.

6. Dharan C.K.H., Lin CL. Longitudinal Compressive Strength of Continuous Fiber Composites. J. Compos Mats 2007: 41(11): 1389-1417.

7. Subramanian S, Lesko JJ, Reifsnider KL, Stinchcomb WW. Characterization of the fiber–matrix interphase and its influence on mechanical properties of unidirectional composites. J Compos Mater, 1996; 30:309–32.

8. Jancar J, Review of the role of the interphase in the control of composite performance on micro- and nano-length scales. J Mater Sci 2008; 43:6747-6757.

9. Moon CK. Study on the interfacial properties of three-dimensionally arranged glass fiber/epoxy resin model composites. J. Appl. Polym Sci. 2010; 116:1483-1490.

10. Gao SL and Mader E, Characterisation of interphase nanoscale property variations in glass fiber reinforced polypropylene and epoxy resin composites, Composites: Part A, 2002; 33:559-576.

11. Sockalingam S., Dey M, Gillespie Jr JW, Keefe M., Finite element analysis of the microdroplet test method using cohesive zone model of the fiber/matrix interface. Composites: Part A., 2014; 56:239-247.

12. Minnicino MA, Santare MH. Modeling the progressive damage of the microdroplet test using contact surfaces with cohesive behavior. Compos Sci Technol 2012; 72(16): 2024–31.

13. Pisanova E, Zhandarov S, and Mader E, How can adhesion be determined from micromechanical tests? Composites: Part A, 2001; 32:425-434.

14. Sheer RJ, Nairn JA. A comparison of several fracture mechanics methods for measuring interfacial toughness with microbond tests. J. of Adhesion 1995; 53: 45-68.

15. Zhandarov S, Gorbatkina Y, and Mader E. Adhesional pressure as a criterion for interfacial failure in fibrous microcomposites and its determination using a microbond test. Compos Sci Technol. 2006; 66: 2610-28.

16. Pisanova E, Zhandarov S, Mäder E, Ahmad I, Young RJ. Three techniques of interfacial bond strength estimation from direct observation of crack initiation and propagation in polymer–fibre systems. Composites: Part A, 2001; 32(3–4): 435–43.

17. Camanho P.P., Davila C.G., and Moura M.F., Numerical Simulation of Mixed-mode Progressive Delamination in Composite Materials. J. Compos Mats., 2003; 37(16):1415-24.

18. Turon A, Davila CG, Camaho PP, Costa J. An engineering solution for mesh size effects in the simulation of delamination using cohesive zone models. Engineering Fracture Mech., 2007; 10:1665–82.

Chapter 5

A MULTISCALE MODELING APPROACH TO PREDICT THE EFFECT OF FIBER TOPOGRAPHY ON THE MICRODROPLET RESPONSE

To determine the effect of different fiber surface topographies on the microdroplet test response currently requires making fibers of varying surface topographies, fabricating these fibers into test specimens, testing the specimens, and analyzing the experimental data. This is a costly and time-consuming approach and it provides no insight into the mechanics of the interfacial system and little guidance on how to tailor the fiber topography to produce a desired structural response. It is therefore highly desirable to create a numerical method to estimate the change in the microdroplet response due to changes in fiber topography. This chapter presents such a method.

In Chapter 3 the effect of fiber topography on the microdroplet force-displacement response is determined by the microdroplet FE model where the fiber-droplet interface is represented by a contact surface with cohesive behavior. In contrast to Chapter 3, where the cohesive parameters were chosen arbitrarily from a range of reported values, in this chapter, the cohesive behavior is estimated *a priori* using the nanoscale interface FE model developed in Chapter 4. This procedure, along with the nanoscale-to-microscale translation process to calculate the effective cohesive behavior parameters from the nanoscale interface model results, is summarized graphically in Fig.

5.1. The nanoscale-to-microscale estimation process requires an initial calibration of the nanoscale interface model material parameters using known experimental data in order to be used in a predictive manner. Once calibrated, the nanoscale interface material parameters are held constant and used in nanoscale interface models of other topographies to predict their cohesive parameters. These cohesive parameters are subsequently used in the microdroplet model to estimate the effect of the fiber topography on the microdroplet response. The effectiveness of this process is evaluated using the experimental data of two glass fiber-epoxy droplet systems with similar material properties but distinctly different fiber surface roughness reported in [1-2]. The experimental response of the first fiber system is used to calibrate the nanoscale interface model parameters (listed in Fig. 5.1). Once calibrated, the nanoscale interface model material parameters are held constant and are used in a second nanoscale interface model that represents the topography of the fiber-droplet interface of the second experimental system. This nanoscale interface model is then used to predict the cohesive parameters needed to simulate the microdroplet force response for the second fiber system. The simulated response is then compared to the second experimental response to evaluate the effectiveness of this approach.

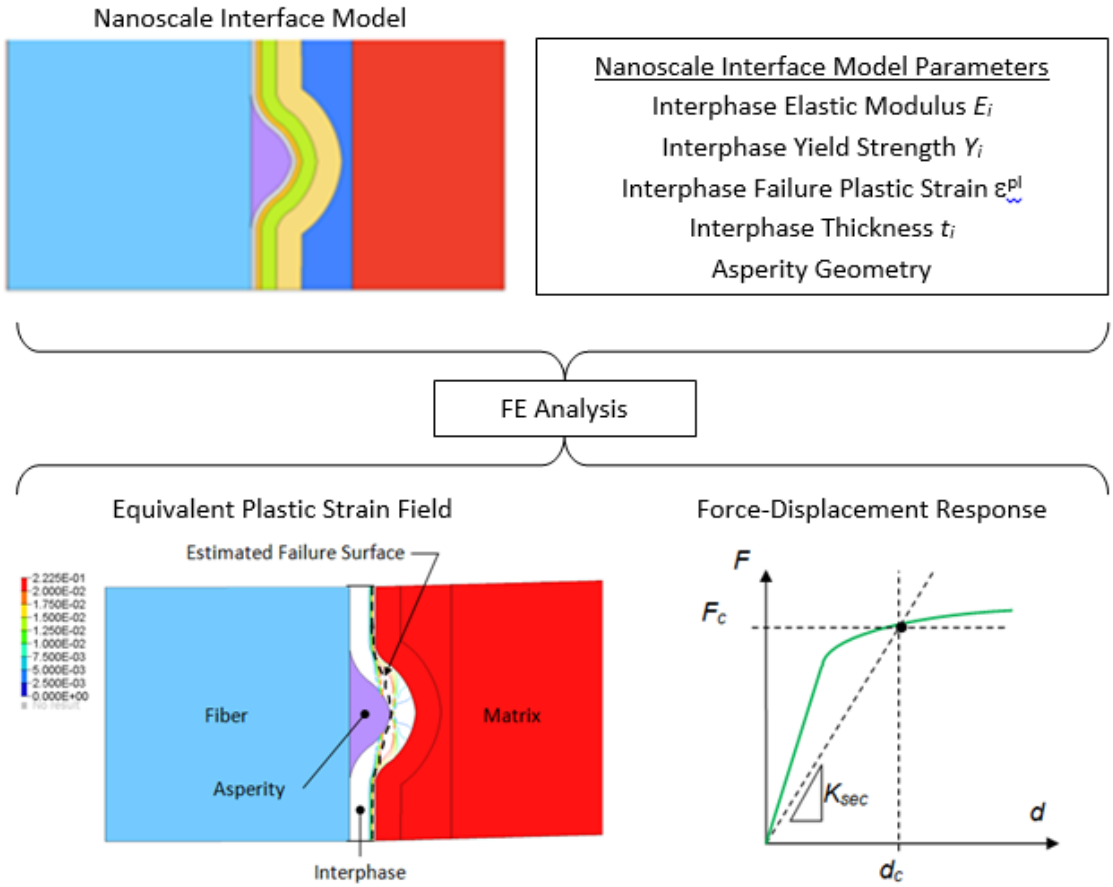

Critical displacement d_c and force F_c correspond to point when equivalent plastic strain field traverses nanoscale model with a magnitude equal to the threshold failure strain.

The area of failure surface is approximated using

Failure Surface Area $$S \approx 2\pi \sum_{i=1}^{n} \frac{(r_i + r_{i-1})}{2} \sqrt{1 + [r'(z)]^2}\, \Delta z_i$$

The microdroplet cohesive parameters are estimated by

Cohesive Stiffness $$K = \frac{1}{2\pi r_f l_r} \frac{F_c}{d_c}$$

Cohesive Strength $$\bar{\sigma} = \frac{F_c}{A} = \frac{F_c}{2\pi r_f l_e}$$

Cohesive Fracture Toughness $$\bar{G} = G_0 \frac{S}{S_o} = G_0 \frac{S}{2\pi r_f l_r}$$

Fig. 5.1. Illustrative summary of the process used to translate the nanoscale interface modeling results into the microdroplet model cohesive parameters.

5.1 Numerical Approach

Accuracy of the predicted microdroplet force response requires that the calculation of the cohesive parameters from the nanonscale interface model be based on a constant and *calibrated* set of nanoscale interface material parameters for the fiber systems with varying topographies. In the following discussion, the terms *tune* and *calibrate* are used to identify two different, specific processes in the approach presented. The term *Tune,* refers to the iterative process of adjusting the microdroplet FE model cohesive parameters to match a known microdroplet experimental response. The term *Calibrate* refers to the separate iterative process of adjusting the nanoscale interface model parameters to yield the set of *tuned* cohesive parameters using the nanoscale-to-microscale translation process detailed in Chapter 4.

This modeling approach is divided into four steps (Tuning, Calibration, Cohesive Behavior Estimation, and Force Prediction) and is shown in Fig. 5.2. Step 1 of the process is to use the microdroplet FE model to *tune* a set of baseline cohesive parameters needed to approximate a known experimental force-displacement response for a glass fiber-epoxy droplet system with known surface roughness. The microdroplet model with the *tuned* cohesive behavior is the baseline microdroplet FE model. Step 2 of the process involves developing and *calibrating* the nanoscale interface FE model of the fiber-matrix interface corresponding to the baseline roughness microdroplet system. Using the cohesive parameter calculations detailed in Chapter 4 and summarized in Fig. 5.1, the nanoscale interface model parameters are iteratively adjusted until they yield the *tuned* cohesive parameters determined in Step 1. The *calibration* of the nanoscale interface

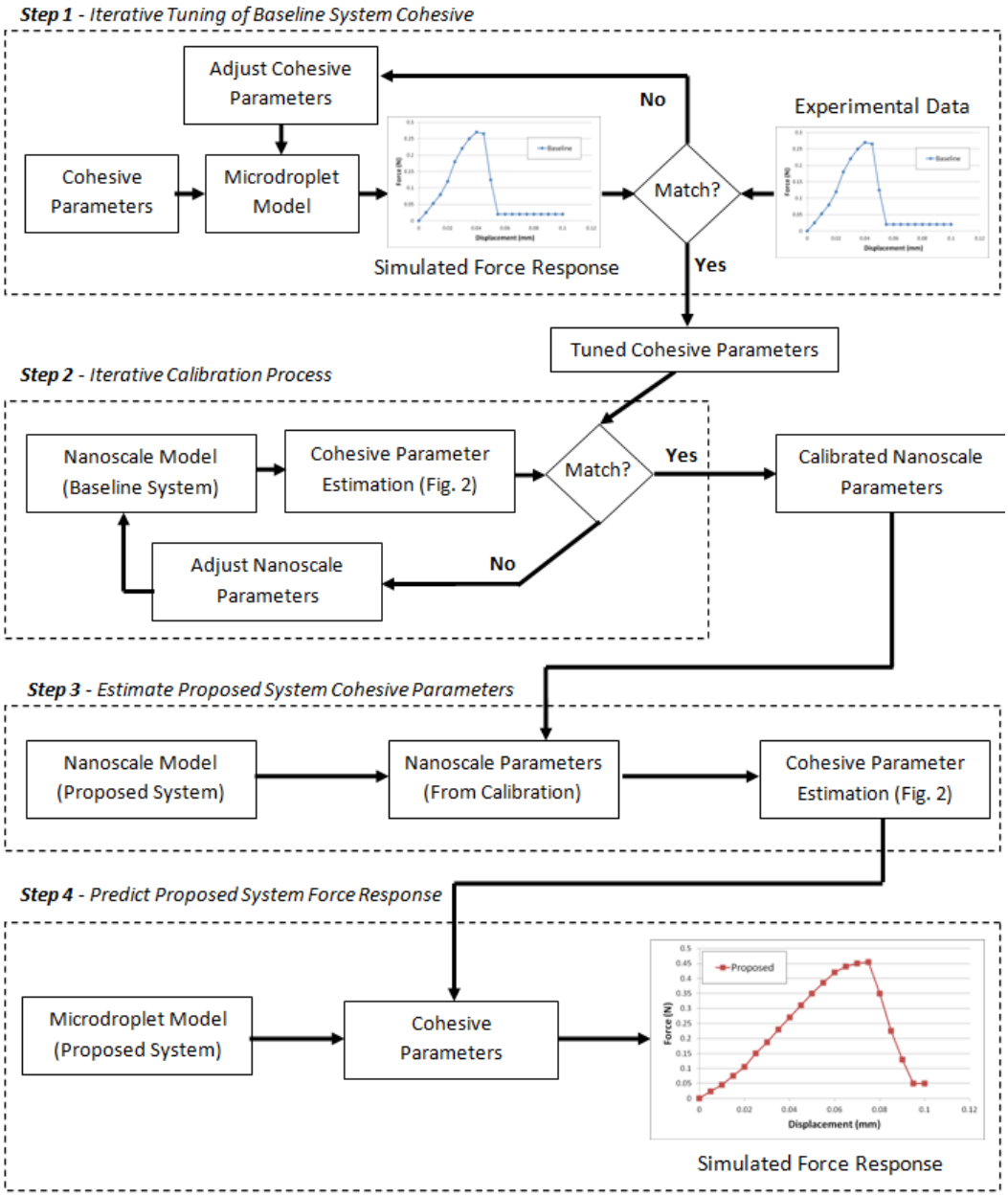

Fig. 5.2. Modeling approach to calibrate nanoscale parameters needed to determine microdroplet cohesive definition for proposed microdroplet system comprised of variable fiber surface roughness.

model defines the nanoscale model material parameters (i.e. interphase elastic modulus, yield strength, and threshold equivalent plastic strain) needed to describe the effective fiber/interphase/matrix response in the microdroplet FE model using a cohesive interface. Ideally, the interphase thickness, and asperity geometry needed for the nanoscale model would be determined from separate, independent measurements. Using this process, the nanoscale interface parameters that produce the tuned cohesive parameters are thus *calibrated* and are assumed not to change with changes in fiber surface topography for a particular material system, (e.g. glass fiber/sizing/epoxy). The *calibration* of the nanoscale interface model parameters (Step 2) enables us to predict the cohesive behavior of a similar microdroplet system with a different fiber surface topography. Step 3 involves the development of a second nanoscale interface FE model that represents this different surface roughness microdroplet system in order to calculate the cohesive parameters for this system via the same nanoscale-to-microscale translation process (See Fig. 5.2). The last step of the process, Step 4, is the simulated prediction of the microdroplet force response for the second surface roughness fiber.

This modeling approach is demonstrated by looking at a known fiber-matrix material system (glass fiber/fiber sizing/epoxy) with two fiber surfaces of different roughness values. The baseline, low roughness (R_a = 5 nm), surface is used to calibrate the nanoscale interface model parameters. Once calibrated, these nanoscale interface model parameters are used in the second nanoscale interface model with larger asperity height corresponding to the higher surface roughness (R_a = 25 nm) fiber system. The cohesive parameters for this, higher-roughness system are thus calculated and used in a

subsequent microdroplet simulation to predict its force response. The predicted force-displacement response is normalized and compared the normalized experimental response to evaluate the effectiveness of this approach.

Typical experimental force-displacement responses from the microdroplet testing reported in [1-2] are shown in Fig. 5.3. These curves are estimated from figures in [1-2] and represent two fiber surface roughness values, R_a=5 nm and R_a=25 nm, produced by the application of blended GPS and TEOS fiber sizing in 1:0 (GPS only) and 3:1 (GT31) ratios, respectively. The force responses shown in Fig. 5.3 represent an individual experiment from a set of thirty experiments for each fiber sizing formulation. Further, the surface roughness varied greatly for fiber sizing formulation, e.g. the mean fiber surface roughness values for GT31 was 25 nm and the reported standard deviation was approximately 32 nm [1-2]. Gao et al. [3] noted that the degree of chemical bonding of blended compatible and incompatible fiber sizings initially increases with increasing content (i.e. wt.% GPS) of compatible sizing but reaches a plateau at approximately a 1:1 ratio. Therefore in this work it is assumed the material properties and chemical adhesion of the two systems are identical so that the only difference is the fiber topography.

The surface of the baseline fiber, i.e. low surface roughness fiber, presented in [1-2] appears smooth and relatively featureless (see Fig. 4.1). The topographic features of the high surface roughness fiber appear stochastic in nature and resemble randomly organized frustums that are attached to the fiber surface (see Fig. 4.1). We note that the nanoscale FE model used here is intended to characterize the average fiber surface roughness and its average mechanical response. However, due to axisymmetry, the

nanoscale interface FE model represents a periodic array of rings around the fiber in the microdroplet system rather than a random collection of frustum-like asperities.

The microscale microdroplet model used in this work is presented in Section 5.2 and tuned in Section 5.3 (Step 1 of Fig. 5.2). The nanoscale interface model is presented and calibrated in Section 5.4 (Steps 2 of Fig. 5.2). The cohesive parameters for the proposed system are identified in Section 5.5 (Step 3 of Fig. 5.2) and used to predict the microdroplet response in Section 5.6 (Step 4 of Fig. 5.2) to assess the effectiveness of this approach.

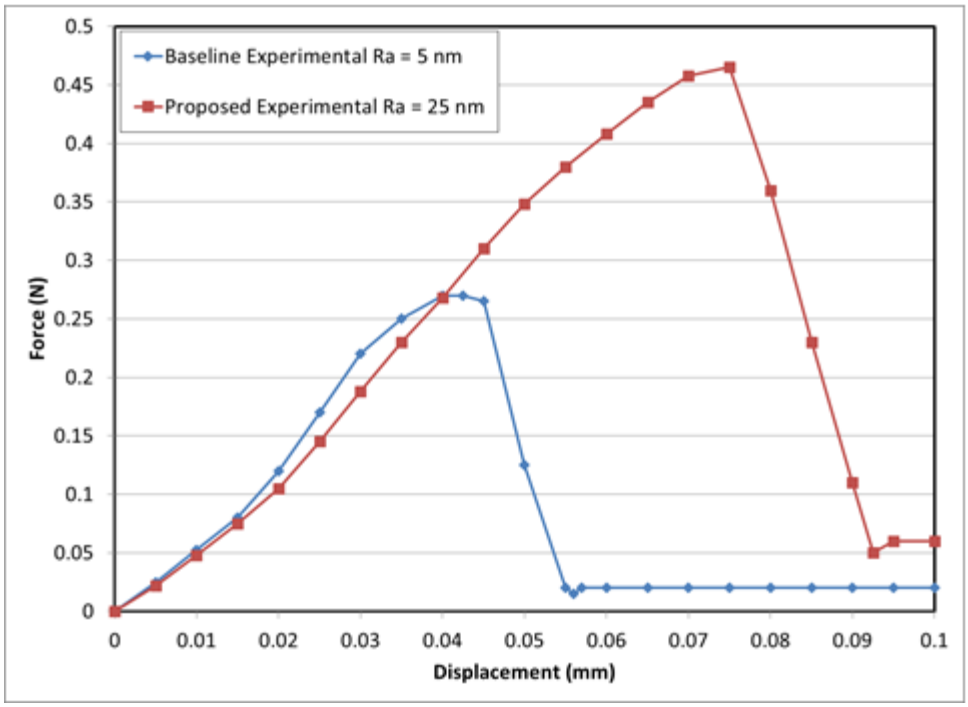

Fig. 5.3. Measured microdroplet force-displacement response for baseline (R_a~5 nm) and proposed (R_a~25 nm) fiber systems [2].

5.2 The Microdroplet Model

A computationally efficient axisymmetric FE model is created for the purpose studying the effect of individual cohesive parameters on the microdroplet force response. The microscale axisymmetric microdroplet model used in this study is similar to the model presented in Chapter 3 and is shown in Fig. 5.4. The geometry of the axisymmetric model more closely approximates the nominal dimensions of the microdroplet experiment in [1-2], particularly the reported average embedded length. The axisymmetric model is created from a 2D-slice of the 3D quarter-symmetric FE model and the droplet mesh scaled so that the embedded length L_e = 136 µm. The glass fiber diameter is 20 µm, and the droplet diameter is 136 µm. The glass fiber free length is 0.8 mm. Model convergence, defined as a maximum difference in reaction force being less than 2% between meshes, with characteristic lengths of 1 µm and 0.5 µm, is achieved using linear, axisymmetric continuum elements. The droplet mesh is comprised of 34048 linear, axisymmetric continuum elements with a 0.5 µm characteristic length and the fiber mesh is comprised on 11500 linear, axisymmetric continuum elements. The microvise is modeled as a rigid body and has an opening diameter of 30 µm; due to the model being axisymmetric, the microvise in the model is an annulus and not an opposing set of prismatic blades. The fiber nodes along the top edge are prescribed to have equal vertical displacement and the centerline node is attached to a spring element that represents the test apparatus compliance and is added to match the initial slope of the experimental force-displacement responses shown in Fig. 5.3. Recall that the experimental force response curves were modified using the process defined in [2] to

account for the test apparatus compliance in order to be compared to the 3D quarter-symmetric model's force response. In the axisymmetric model, the spring element is defined to have a stiffness of 18 kN/m and is located between the virtual ground ('x' in Fig. 5.4) and the top edge of the fiber free length. Lastly, to stabilize the solution while satisfying the requirement that $\eta << \Delta t$ with the time increment (~1 sec) we chose a constant cohesive viscous regularization coefficient η of 10^{-4} sec.

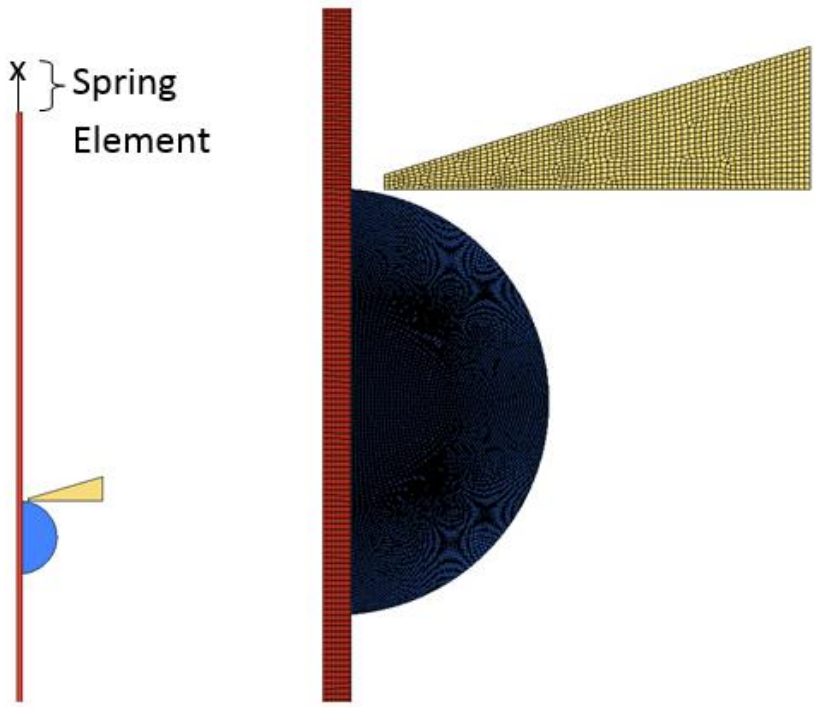

(a) (b)

Fig. 5.4. Axisymmetric (a) microdroplet model and (b) close-up of interface and mesh.

A residual stress due to curing of the epoxy droplet is developed by prescribing a temperature drop from the stress free temperature of 150 °C (the epoxy cure temperature) to 25 °C (ambient temperature) [1, 4]. This residual stress produces the interface tractions shown in Fig. 5.6 for temperature independent elastic parameters. The droplet is sheared from the fiber by downward motion of the microvise relative to ground. The mechanical properties for the glass fiber and epoxy droplet are shown in Table 5.1.

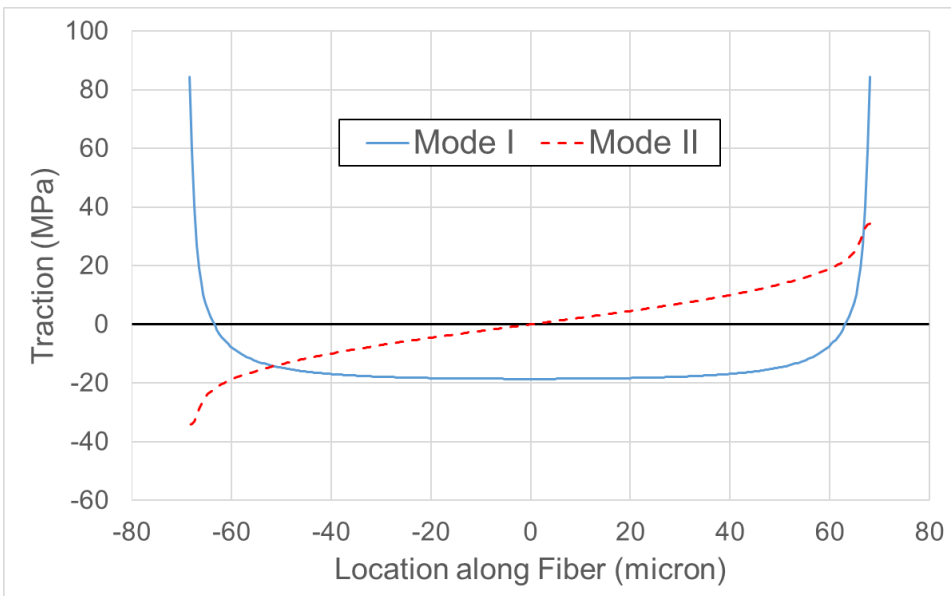

Fig. 5.5. Fiber-droplet interface traction arising from thermal preload.

In the model, a maximum stress criterion is used to define damage initiation and a "power law" (n=1) is used to define the damage evolution in the cohesive interface. The maximum stress criterion for damage initiation is

$$\max\left\{\left(\frac{<\sigma>}{N}\right),\left(\frac{\tau}{S}\right)\right\}=1 \tag{5.1}$$

where σ is the contact surface normal traction, τ is the shear traction, *N* and *S* are the cohesive strengths in the normal and shear directions, respectively, and the < > brackets are Macaulay brackets which indicate that compressive normal stress does not initiate damage. Complete failure of the interface is given by

$$\left(\frac{G_n}{G_n^C}\right)^n + \left(\frac{G_s}{G_s^C}\right)^n = 1. \tag{5.2}$$

where G_n and G_s denote the fracture energy in the normal and shear mode, respectively, and the superscript '*C*' refers to the critical fracture energy required for complete failure in a particular mode.

Table 5.1. Material properties used in the microdroplet and nanoscale interface models

Component	Glass Fiber	Epoxy Droplet	Interphase*
Elastic Modulus E [MPa]	72000	3200	2200
Poisson's Ratio υ	0.22	0.35	0.35
Yield Strength [MPa]	-	-	35
CTE (ppm/°C)	8.8	55	55

(*Nanoscale Model Only)

5.3 Tuning the Baseline Cohesive Behavior

As explained earlier, the calibration of the nanoscale interface parameters to a microdroplet response for a known fiber topography is required to predict the microdroplet response using fibers of different topographies. The first step of this process is to tune the microdroplet cohesive properties to yield a simulated response that compares well to the experimental microdroplet response. In this section, we focus on

tuning the baseline system cohesive parameters of the microdroplet FE model to match the experimental response of the low surface roughness microdroplet system, Step 1 in Fig. 5.2.

In order to *tune* the cohesive parameters so that the microdroplet FE model response matches the experimental response of the baseline system it is necessary to understand the influence of the individual cohesive parameters on the microdroplet response. This was the objective of the parametric study conducted in Chapter 3. Additionally, the comparison between the simulated response and the experimental response may differ due to the high degree of variation in the test setup from sample to sample since the exact geometry (fiber free length, embedded fiber length, droplet diameter, microvise opening, etc.) for each individual experiment is not reported. The force-displacement responses are therefore expected to show some deviation. Therefore for comparison, the interfacial shear strength (IFSS) is computed by dividing the maximum force by the interface area, i.e.

$$IFSS = \bar{\tau} = \frac{F_{peak}}{\pi d_f l_e} \tag{5.3}$$

where F_{peak} is the maximum force of the force-displacement response, d_f is the fiber diameter, l_e is the embedded fiber length, and $\bar{\tau}$ is the shear traction where the subscript bar denotes the average. The IFSS is the most frequently reported result from microdroplet testing and therefore it is important that the prediction process be able to accurately estimate the IFSS. Because there are several adjustable parameters, there may be more than one set that match the simulation results to the experiment. However, the

observations from the parametric study discussed earlier serve as a guide for the ranges and adjustment of the cohesive parameters. The set of cohesive parameters chosen, which produces the force response associated with the *low surface roughness* fiber are N=251 MPa, S = 34.3 MPa, K_n = 8.8x10^{15} Pa/m, K_s = 2.0x10^{15} Pa/m, G_{IC} =G_n= 755 J/m^2, and G_{IIC} =G_s= 775 J/m^2. It is noted that the cohesive stiffness values estimated by this method are of the same magnitude, i.e. 10^6 N/mm^3 (10^{15} Pa/m), as suggested by [5]. The normal strength and fracture energy are the least influential parameters on the microdroplet force response as determined by the parametric study detailed in Chapter 3; this observation is also noted in [4]. Therefore the normal direction cohesive strength and fracture toughness are chosen *a priori* to be relatively large in order to be of the same magnitude as the normal direction cohesive parameters estimated by the calibration of the nanoscale interface model. In particular, the relatively large normal strength arises due to the periodic boundary conditions along the edges of the nanoscale interface model during calibration as explained in the Chapter 4. A constant friction coefficient of μ=0.22 between the fiber and droplet is prescribed to capture the approximately constant shear traction of 2.8 MPa characterizing the post-failure steady state sliding of the droplet relative to the fiber. Using these numerical parameters, the interfacial shear stress-normalized displacement curve of the microdroplet simulation approximates the experimental curve as shown in Fig. 5.6. The simulated response is horizontally offset to match the slope during the linear portion of the experimental response, after the nonlinear stiffening at the beginning of the response and before the nonlinear softening due to debonding and other nonlinearities near the maximum force. These differences may arise

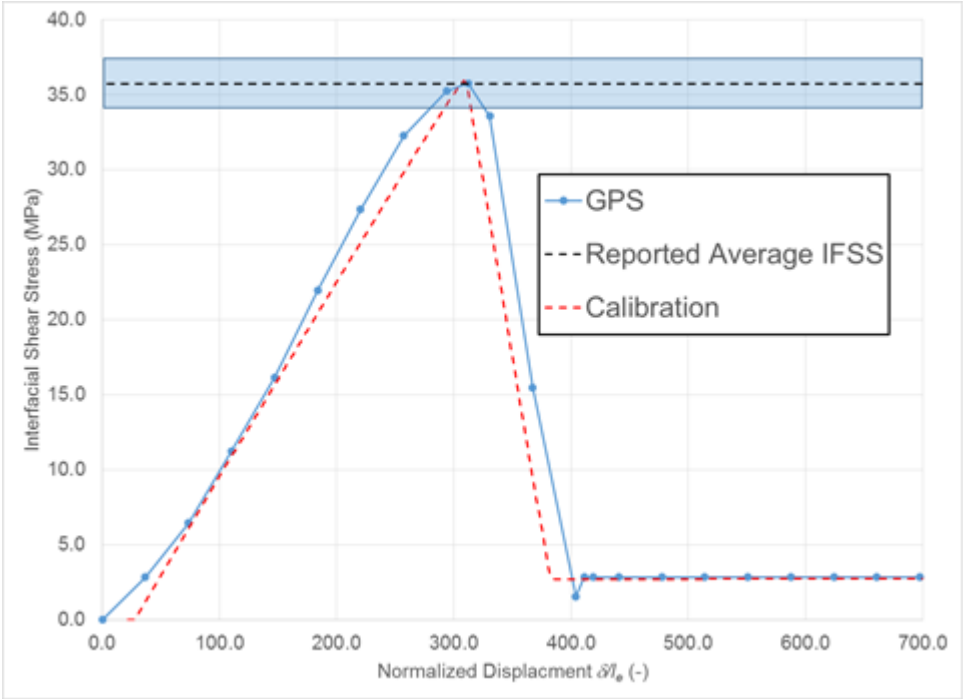

Fig. 5.6. Comparison of experimental and simulated microdroplet interfacial shear stress-normalized displacement responses for low roughness system to reported IFSS average and standard deviation.

due to nonlinearities in the fixture used in the experiment. Overall, the simulated response compares well to the experimental response.

5.4 Calibration of Nanoscale Interface Model

In this section, the nanoscale interface model representing the baseline, low surface roughness fiber system is calibrated to yield the cohesive parameters of the microdroplet model that were identified in the previous section. This is Step 2 of Fig. 5.2. The nanoscale interface model represents a segment of the fiber-droplet interface as shown in Fig. 5.7. The baseline (low roughness) fiber system is reported to have a fiber roughness characterized by a R_a = 5 nm [1-2]. Similar to the nanoscale interface models detailed in

the Chapter 4, this nanoscale interface model is created with a surface roughness of R_a = 5 nm and is shown in Figure 5.7(b) where a triangular asperity is fixed to the neat fiber surface to give an approximation to the textured fiber surface topography. Note that only the outermost micron of the fiber is included and therefore the model presumes that the axial deformation gradient in the core of the fiber is small during the microdroplet test. This is a reasonable approximation since the elastic modulus of the glass fiber is an order of magnitude greater than that of the interphase and matrix.

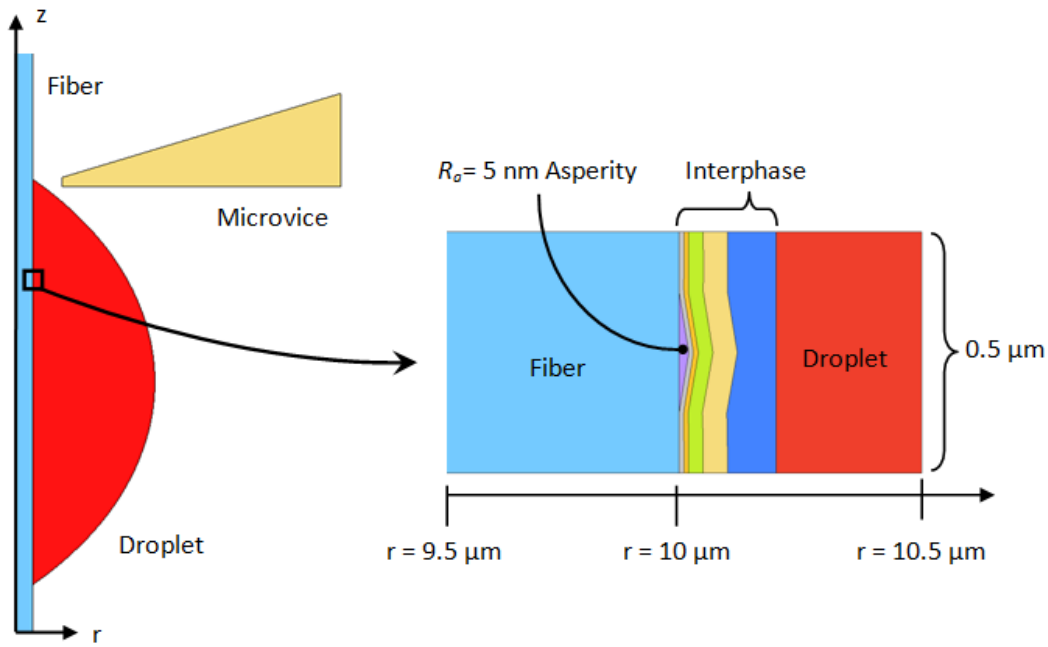

(a) (b)

Fig. 5.7. Axisymmetric (a) finite element microdroplet model and (b) nanoscale interface model of low-roughness fiber system.

The nanoscale interface model boundary conditions are the same as presented in Chapter 4, namely the periodic boundary conditions expressed by

$$u_x(r, z = 0\mu m) = u_x(r, z = 0.5\mu m) \tag{5.3}$$

$$u_z(r, z = 0\mu m) = u_z(r, z = 0.5\mu m)\,. \tag{5.4}$$

Additionally, residual stress due to curing of the droplet on the fiber is included in the same manner described in the axisymmetric microdroplet model in Chapter 3.

The interface properties need to be evaluated in both tension and shear, since the actual failure is a combination of both modes [1-4, 6-7]. The tensile behavior of the interface is evaluated by displacing the outer, radial edge of the droplet in the radial direction (horizontally in Fig. 5.7(b)) and constraining the axial (vertical) displacement of the outer, radial edge to be zero, i.e. $u_x(r_o = 10.5\mu m, z) = \alpha$ and $u_z(r_o = 10.5\mu m, z) = 0$ where α is the prescribed radial displacement. Although this is not a realistic mode of deformation in an axisymmetric system, it is imposed to characterize the tensile properties of the particular fiber-interphase-matrix system at the nanoscale. The shearing deformation behavior is simulated by displacing the outer, radial edge of the droplet in the axial direction (vertically in Fig. 5.7(b)) and constraining the radial (horizontal) displacement, i.e. $u_x(r_o, z) = 0$ and $u_z(r_o, z) = \lambda$ where λ is the prescribed axial displacement.

The topographic features of the fibers presented in [1-2] were characterized by the arithmetic average of absolute surface roughness values, i.e.

$$R_a = \frac{1}{L}\int_0^L |h(x)|dx \approx \frac{1}{N}\sum_i |h_i| \tag{5.5}$$

where *h(x)* is the absolute height of the surface relative to the reference surface height, *L* is the length of the measured surface, and *N* is the number of discrete samples. Consequently, the triangular asperity height and width for the R_a = 5 nm surface roughness fiber are 20 nm and 250 nm, respectively. Further, the nanoscale interface model is constructed to have a series of conformal, stratified layers adjacent to the fiber and asperity so that systems of differing interphases thicknesses and mechanical properties can be simulated using the same FE geometry file.

The material parameters for the nanoscale model interface (namely interphase elastic modulus, interphase yield strength, and failure strain) are set such that the nanoscale interface model reproduces the baseline microdroplet model cohesive behavior parameters determined in the previous section using the process detailed in the Chapter 4 and summarized Fig. 5.1. Additionally, the interphase thickness and elastic modulus may to be determined in a more direct manner using methods similar to [8-10] but are estimated in this step using an iterative process. The nanoscale interface model parameters that correspond to the tuned cohesive parameter values in this example are: interphase material elastic modulus of 2200 MPa and yield stress of 59.5 MPa, critical equivalent plastic strain of 2%, and a conformal interphase thickness of 75 nm. As mentioned earlier, other sets of interphase parameters may also result in a reasonable approximation to the baseline cohesive behavior.

5.5 Cohesive Parameter Prediction

Using the calibrated nanoscale interface model parameters defined in the previous section, a second nanoscale interface model representing the geometry of the higher surface roughness fiber is analyzed. From this second nanoscale model, a new set of cohesive parameters are determined and used in the microdroplet model to assess the effect of the fiber topography on the microdroplet response. This is *Step 3* of Fig. 5.2. The higher-roughness fiber has a surface roughness of R_a = 25 nm. A definitive description of the topography of the fiber surface is difficult to establish from the images reported in [2] and therefore we have developed three nanoscale interface models all with roughness of R_a = 25 nm but with different asperity geometries. These three nanoscale interface models are shown in Fig. 5.8 and are identified by their asperity: tall rectangle, short rectangle, and sinusoid. A set of cohesive parameters for each of the nanoscale interface models is estimated using the process shown in Fig. 5.1 and the results are listed in Table 5.2. Additionally, the coefficient of friction (μ=0.22) identified during the tuning of the microdroplet model (Step 1 of Fig. 5.2) is used to predict the microdroplet response produced using the R_a =25 nm fiber.

Table 5.2. Estimated cohesive parameters used in microdroplet model

Asperity Geometry	Stiffness [10^{15} Pa/m]		Strength [MPa]		Fracture Toughness [J/m^2]		Friction Coefficient
	K_n	K_s	N	S	G_I	G_{II}	
Baseline	8.8	2.0	251.0	34.3	754.0	775.0	0.22
Rectangle, Tall	9.0	2.2	292.5	39.5	942.0	781.0	0.22
Rectangle, Short	9.1	2.1	288.1	34.4	855.0	777.0	0.22
Sinusoid	9.3	2.4	256.9	39.0	847.0	786.0	0.22

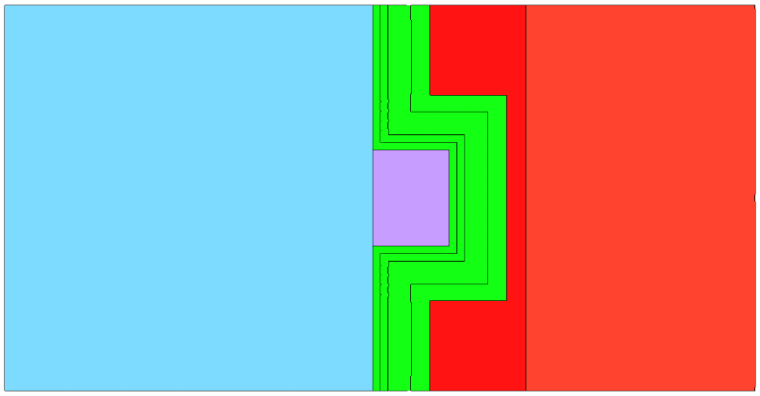

(a)

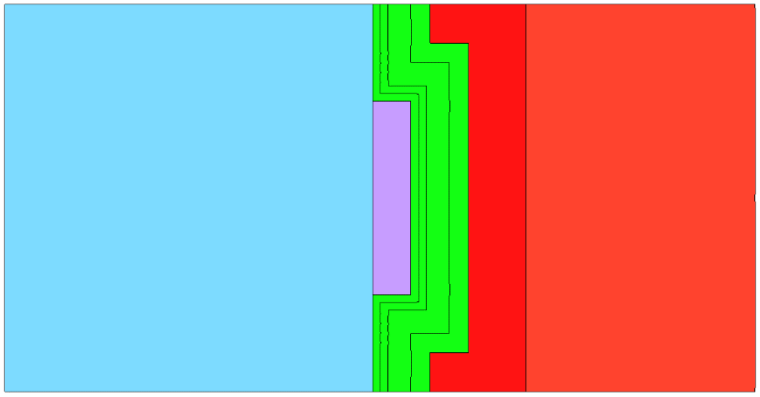

(b)

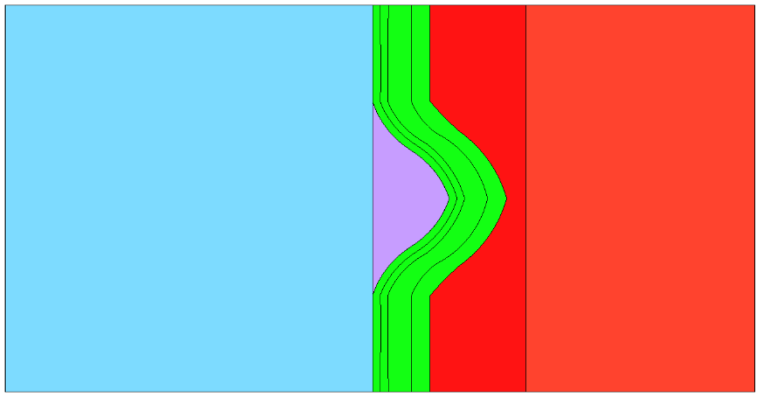

(c)

Fig. 5.8. Nanoscale interface models of the high-roughness R_a=25 nm systems (a) tall rectangle asperity, (b) short rectangle asperity, and (c) sinusoid asperity with 75 nm thick conformal interphase.

5.6 Predicted Microdroplet Responses

The simulated microdroplet interfacial shear stress-normalized displacement responses for the R_a=25 nm systems are shown in Fig. 5.9 with the normalized experimental response and reported average IFSS measured by Gao et al. [1-2] for comparison. The simulated responses use the cohesive contact parameter sets determined using the nanoscale interface model listed in Table 5.2 (Step 4 of Fig. 5.2.). The most obvious difference is in the peak interfacial shear stress magnitude with the largest simulated peak corresponding to the tall rectangle and sinusoid asperity geometries and the short rectangle asperity geometry corresponding to the lower peak interfacial shear stress magnitude. The approximately equivalent responses of the sinusoid and tall rectangle simulations is expected since their cohesive parameters are nearly equivalent. This is due, in part, because the interphase thickness (75 nm) in both cases is similar to the asperity height (100 nm). The lower interfacial shear stress response of the short rectangle is due to its lower asperity height (50 nm). The peak shear stress magnitudes are slightly lower than the experimental average IFSS but are within the standard deviation of IFSS reported in [1-2]. However, the experimental steady-state pullout shear stress magnitude is underestimated by the simulations with μ=0.22.

The higher coefficient of friction in the higher-roughness fiber system can be attributed to a change in the failure path [1-2]. Gao et al. notes that the interfacial failure mode changes from a predominantly <u>adhesive</u> mode at the fiber-interphase interface for the R_a = 5 nm surface roughness fiber system to a predominantly <u>cohesive</u> mode for the R_a = 25 nm surface roughness fiber system [1-2]. Consequently, the increase in the

effective coefficient of friction is likely due to the change in failure mode since the coefficient of friction between the fiber and interphase materials (adhesive failure mode) is expected to be less than the coefficient of friction between the interphase and itself (cohesive failure mode). The increased coefficient of friction is not captured by the nanoscale interface model and additional study of friction's dependence on the failure mode is warranted. Accounting for the increased effective coefficient of friction by setting the coefficient of friction to $\mu = 0.4$ results in a more accurate simulated response in terms of peak interfacial shear stress, i.e. IFSS per Eq. (5.3), and steady-state pullout interfacial shear stress as shown in Figure 5.10. The simulated response compares well with the experimental response up to peak load and during the steady-state pull-out. However, the simulated responses show a sudden drop in interfacial shear stress after the peak for the tall rectangle and sinusoid asperity geometry simulations and a slightly more gradual reduction in interfacial shear stress magnitude for the short rectangle asperity geometry simulation. In view of the parametric study (Chapter 3), this indicates that the fracture toughness used in these simulations is too low and is due to the change in interfacial failure mode from a predominantly lower fracture toughness failure mode (adhesive mode) to a predominantly higher fracture toughness failure mode (cohesive mode). All of the simulated force-displacement responses are nearly linear up to peak force and do not exhibit the nonlinear behavior observed in the experimental curve. As mentioned previously, this nonlinearity may be due to a nonlinear elastic response of the fixture. Further, the comparison could be improved by modeling the exact geometry of the microdroplet experiment as well as

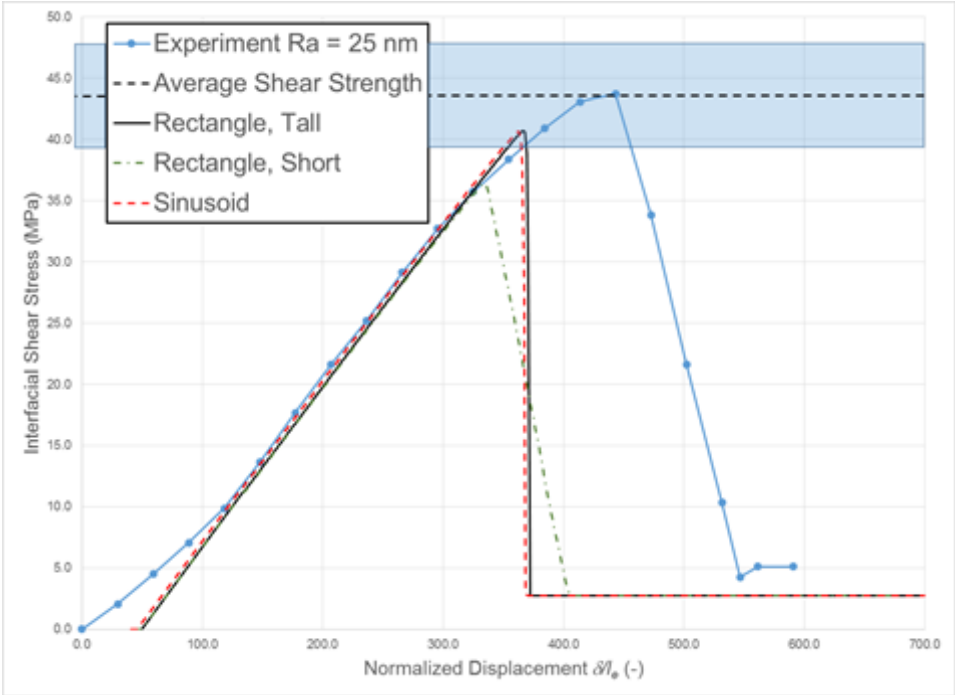

Fig.5.9. Comparison of experimental to simulated interfacial shear stress-normalized displacement response using cohesive contact parameters listed in Table 5.2.

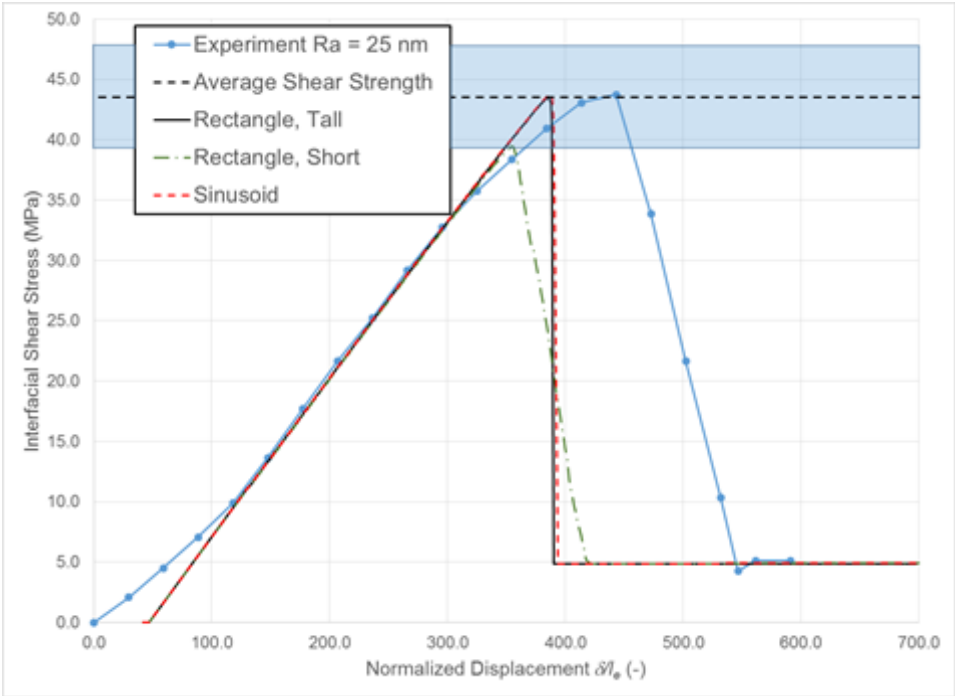

Fig.5.10. Comparison of experimental to simulated interfacial shear stress-normalized displacement response using the estimated cohesive contact parameters listed in Table 5.2 with increased coefficient of friction, μ= 0.4.

obtaining more accurate estimates of the cohesive parameters from a 3D nanoscale interface model that better represents the actual surface topography of the fiber.

5.7 Summary

The simulated responses produced by the approach presented in this work compare fairly well to the experimental response up to peak load. This modeling approach has value in its simplicity and its ability to be used as a design tool in the engineering of advanced fiber systems for tailored strength and toughness. Differences between the predicted responses and experimental responses are likely due to differences in the microdroplet specimen geometry including microvise opening, potential damage of the bulk epoxy droplet at locations near the microvise contact zone, apparatus compliance, and thermally induced residual stress. These features can be accounted for in the microdroplet simulation provided that they can be experimentally measured.

Additionally, differences in the predicted and experimental response may be due to the estimation of the cohesive parameters from an axisymmetric, nanoscale model when the fiber topography is best represented by a 3D nanoscale model. The simulation results also indicate that the arithmetic average of absolute values for surface roughness, R_a, may not be sufficient to characterize the fiber surface using this approach since it is shown that three different fiber asperities geometries (Sinusoid, Tall Rectangle, Short Rectangle) having R_a = 25 nm produced two distinct cohesive contact definitions and that these unique cohesive contact behaviors yielded drastically different simulated microdroplet response predictions for two of the three simulations. Consequently, a more

robust measure of surface roughness such as the root-mean-squared surface roughness, R_{rms}, may be required in the employment of this approach. Lastly, the higher coefficient of friction and higher fracture toughness in the higher-roughness fiber system can be attributed to a change in the interfacial failure mode changes from a predominantly adhesive mode at the fiber-interphase interface for the R_a = 5 nm surface roughness fiber system to a predominantly cohesive mode for the R_a = 25 nm surface roughness fiber system.

REFERNCES

1. Gao X, Jensen RE, Li W, Deitzel J, McKnight SH, Gillespie Jr JW. Effect of fiber surface texture created from silane blends on the strength and energy absorption of the glass fiber/epoxy interphase, J. Compos. Mats., 2008, 513-534.

2. Gao X. *Tailored Interphase Structure for Improved Strength and Energy Absorption of Composites*, Ph.D. Thesis, University of Delaware, USA. Spring 2006.

3. Gao X, Jensen RE, McKnight SH, Gillespie Jr JW. Effect of colloidal silica on the strength and energy absorption of glass fiber/epoxy interphases. Compos. A, Appl. Sci. Manuf., 2011; 42(11): 1738–47.

4. Sockalingam S., Dey M, Gillespie Jr JW, Keefe M., Finite element analysis of the microdroplet test method using cohesive zone model of the fiber/matrix interface. Composites: Part A., 2014; 56:239-247.

5. Camanho PP, Da´vila CG, de Moura MF. Numerical simulation of mixed-mode progressive delamination in composite materials. J Compos Mater 2003;37(16):1415–38.

6. Pisanova E, Zhandarov S, and Mader E, How can adhesion be determined from micromechanical tests? Composites: Part A, 2001; 32:425-434.

7. Liu CH and Nairn JA. Analytical and experimental methods for a fracture mechanics interpretation of the microbond test including the effects of friction and thermal stresses. Intl. J. of Adhesion & Adhesives 1999; 19:59-70.

8. Pompe G, Mader E. Experimental detection of a transcrystalline interphase in glass-fibre/polypropylene composites. Compos. Sci. and Technol., 2000; 60: 2159-2167.

9. Mader E, Mai K, and Pisanova E. Interphase Characterization in Polymer Composites – Monitoring of Interphasial Behavior in Dependence on the Mode of Loading, Composite Interfaces, 2000; 7(3): 133–147.

10. Gao SL and Mader E. Characterisation of interphase nanoscale property variations in glass fiber reinforced polypropylene and epoxy resin composites, Composites: Part A, 2002; 33:559-576.

Chapter 6

CONCLUSIONS AND FUTURE WORK

6.1. Conclusions

This research provides a new multiscale modeling methodology to determine the microdroplet force-displacement response due to changes in the fiber surface roughness. The multiscale modeling approach uses a nanoscale FE model that is constructed to represent the interface of a known fiber-droplet system with assumed or characteristic fiber surface roughness, interphase thickness, etc. The structural behavior of the nanoscale interface model is characterized in tension and in shear in order to estimate the microscale cohesive contact parameters for the particular material system. These *a priori* predicted cohesive parameters are subsequently used in the microdroplet FE model to predict the effect of different fiber topography on the microdroplet structural response. This research has shown that this approach predicts the microdroplet response reasonably well, particularly the interfacial shear strength (IFSS), which is the most significant and frequently reported data from these tests.

This research has also successfully demonstrated the use of cohesive contact to simulate the progressive fiber-droplet interface failure that occurs during the microdroplet test. This flexible surface-based modeling approach is beginning to be used by other

researchers to simulate the progressive debonding that occurs during the microdroplet test and other single-fiber test methods [1-3].

6.2 Contributions

Research into the formation, structure, and elastic behavior of the interphase continues to increase; however there is little control over the interphase structure and elastic behavior. Further, direct evaluation of the interphase is difficult due to its nanoscale characteristic length. The current trial-and-error development of sizings is a laborious task to create, apply, and test fibers with novel fiber sizings; further, the task is made more arduous by the number of samples needed to correlate experimentally derived composite, macrocomposite or microcomposite, structural properties, to the designed fiber sizing formulation. Lastly, as research of the structural significance of interphase increases, there is little research, experimental or numerical, that examines the role of mechanically interlocked fiber/interphase/matrix interfaces excluding the experimental efforts presented in [10-12]. Although seminal experimental efforts [9-12] indicated that increased fiber surface roughness leads to mechanically interlocked fiber/interphase /matrix interfaces that produced enhanced strength and energy absorbing composites, the strength and energy absorption enhancement mechanisms provided by the increased fiber surface roughness is inferred by the experimental data. These mechanisms need to be numerically studied in order to develop understanding of, and the ability to predict, how fiber surface roughness and interphase can be manipulated to produce composite material properties by design, i.e. a bottom-up design approach.

The unique contributions of this research include the development of a simulation approach to model the progressive damage of the fiber-droplet interface of a microdroplet specimen in order to simulate the entire test. It is noted that this simulation approach can be applied to any single fiber test, e.g. fiber push-out or fiber fragmentation tests. Another unique contribution is that this the first research to model the microdroplet system's structural response at the level of the nanoscale fiber topography. Lastly, this research presents a unique multiscale modeling technique that is used to estimate microscale simulation cohesive parameters from nanoscale simulation results.

6.3 Future Work

Suggestions for future efforts are grouped into a) modifications to the experimental procedures made evident from this computational work and b) improvements to the computational methodology itself. Microdroplet test specimens are difficult to fabricate uniformly and test consistently due to their miniature size; however, data reporting of key test parameters, e.g. fiber free length, fiber embedded length, microvise opening, etc., is needed so that these experiments can be more accurately modeled. For this reason, in future testing it is suggested that prismatic microvises with adjustable blade openings be replaced with an annular disk with a fixed-diameter hole and narrow radial slit for fiber pass-through. The benefits of an annular disk microvise include: increased structural stiffness of the test apparatus, removal of microvise opening variability, and easier and more efficient simulation using axisymmetric models. Another experimental modification is to report the way raw force-displacement data because very

often the data is reported in a summarized form such as IFSS with no description of the force-displacement curve shape or its associated interfacial area.

Another suggestion for improvement of experimental research is better characterization of the fiber surface topography. The fiber surface is currently characterized by the absolute arithmetic average R_a. It was shown in Chapter 5 that significantly different fiber topographies can be constructed to have the same R_a-value yet produce different microdroplet structural responses. It is suggested that the root-mean-square surface roughness R_{rms} be used to more accurately characterize the fiber surface topography.

The primary effort needed for the future computational work is improvement of the nanoscale-to-microscale translation process. The nanoscale interface model represents the characteristic microdroplet fiber-droplet interface and it is characterized separately in tension and in shear in order to determine the cohesive parameters using the process detailed in Chapter 4. This nanoscale-to-microscale translation process implicitly assumes that these deformation modes (tension and shear) are independent and ignores the effects of multi-axis loading. A more tightly-coupled nanoscale-to-microscale translation process would be better. A true multiscale modeling tool for structural applications such as MultiMech [4] is a possible solution to this issue. In multiscale modeling software, the constitutive law of the each parent (larger scale) *element* is tightly coupled to the structural response of the child (smaller scale) *model* defined with its associated structural and material behaviors. This is a bottom-up modeling approach that is capable of accounting for multi-axis loading effects and likely will require that the

cohesive contact traction-separation law be coupled, i.e. non-zero off-diagonal stiffness terms. This is in contrast to many structural software packages such as NASTRAN [5] and Abaqus [6] that feature a global-local modeling technique (the global-local approach is referred to as "Submodeling" in Abaqus) which is a top-down modeling approach where the local and global models share a common boundary and the local model is driven by the applied boundary conditions resulting from the global model.

The nanoscale interface model should be improved for increased simulation fidelity. Currently, the nanoscale interface model does not model crack propagation. Fiber-interphase interfacial crack propagation can be modeled using surface-based cohesive behavior as is done in the microdroplet test simulation. However, in the microdroplet test, the crack is propagated by a successive failure of the cohesive contact elements. In traditional FE modeling where the crack path is not known *a priori*, material failure, i.e. the formation of a crack, is often realized by element deletion resulting in a crack width equal to the size of the deleted element. The finite sized gap prevents load transfer across the crack interface and therefore results in an increasingly decoupled model as the crack propagates.

Rather than delete elements to model material failure, a better approach is to employ the extended finite element method (XFEM) where the conventional elements are "enriched" by additional functions using the partition of unity finite element method [7] as introduced in [8]. Essentially in XFEM, the elements are conventionally formulated with "phantom" or virtual nodes tied to the real element nodes until a crack "initiates" (in Abaqus terminology, a crack is initiated when the damage initiation criterion met), at

which time the phantom nodes and the enriched functions to capture the displacement jump discontinuity are activated and the element is partitioned into two regions where each region is composed of a combination of real and phantom nodes as shown in Fig. 6.1. The motion of the phantom nodes is governed by a traction-separation law until complete damage upon which the phantom nodes move independently relative to their real node twin.

XFEM has many advantages over other methods to model failure. The primary advantage of XFEM is that the mesh does not need to conform to the crack geometry nor require mesh refinement compared to the conventional FE method. This is in contrast the cohesive contact failure approaches where the contact surfaces used, for example, to simulate the progressive debonding between the fiber and droplet in the microdroplet test requires that the contact surface to be aligned with the element boundaries and therefore the crack path is predetermined. In XFEM the crack may initiate and propagate along an arbitrary, solution-dependent path, cutting across elements.

The primary disadvantage to the current implementation of XFEM in Abaqus is that contact is limited to a small-sliding formulation. The small-scale sliding formulation assumes that a slave node only interacts with the same local master surface throughout the entire analysis. This contact formulation for XFEM is appropriate for Mode I crack propagation; however, it is not suited for Mode II crack propagation where a finite-sliding contact formulation is required. It is likely that finite-sliding contact will be included in a future release of Abaqus.

As researchers continue to develop novel fiber topographies, including highly textured fiber surfaces, non-uniform thickness fibers, and fuzzy fibers (nanotubes grown in situ from the fiber surface), their structural performance will need to be assessed by a microscale, single-fiber test method. As the data from these microscale single fiber tests continues to increase, the research presented in this dissertation, will allow insights into the mechanics of the microscale tests that are otherwise not possible due to the small size scale of the experiments. Further, this research provides the groundwork needed for predicting a composite material's structural response across multiple length scales and provides a roadmap to optimizing the fiber topography, interphase mechanical properties, and interphase thickness to achieve an application-specific structural performance.

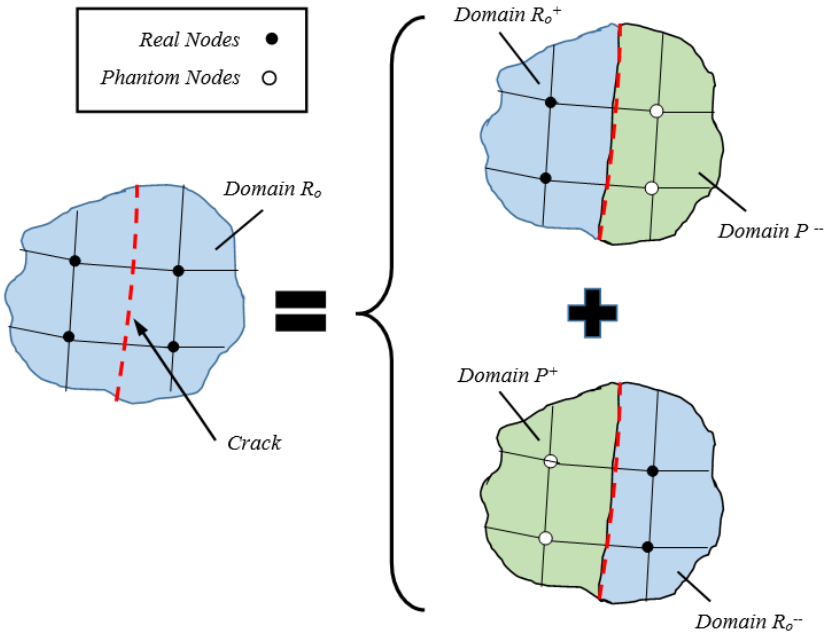

Fig. 6.1. The XFEM decomposition of a cracked element as the sum of a two regions composed of real domain R_o and phantom domain P.

REFERENCES

1. Sockalingam S., Dey M, Gillespie Jr JW, Keefe M., Finite element analysis of the microdroplet test method using cohesive zone model of the fiber/matrix interface. Composites: Part A., 2014; 56:239-247.

2. Gunawan FE, "A new approach for debonding characterization," EDP Conferences, 2014.

3. Abu Al-Rub R, Kim S-M, Bani-Hani KA, Al-Nuaimi N, and Senouci A, "Finite element simulation of single carbon nanotube pull-outs from a cementitious nanocomposite material using an elastic-plastic-damage and cohesive surface models," Int. J. Theoretical and Applied Multiscale Mechanics, Vol 3(1) 2014.

4. Souza FV, Allen DH, and Kim Y-R, "Multiscale model for predicting damage evolution in composites due to impact loading," Compos. Sci. and Technol., 68 (2008) 2624-34.

5. MSC/Nastran Desktop, MSC Software Corp., Newport Beach, CA. 2014.

6. Abaqus 6.12-1 User's Manual, Dassault Systemes, Providence, RI. 2012.

7. Melenk JM and Babuska I, "The partition of unity finite element method: basic theory and applications," Computer Methods in Applied Mechanics and Engineering, 1996; 139:289-314.

8. Belytschko T and Black T, "Elastic crack growth in finite elements with minimal remeshing," Intern. J. for Numerical Methods in Engineering, 1999; 45(5):131-150.

APPENDIX

LETTER OF PERMISSION TO USE COPYRIGHTED MATERIAL

Michael Minnicino <minnicino@gmail.com>

Dissertation Figure Use
2 messages

Michael Minnicino <minnicino@gmail.com> Mon, Jun 22, 2015 at 1:19 PM
To: xgaocomposite@gmail.com

Dr. Gao,

My name is Michael Minnicino and I am currently a PhD candidate in the Department of Mechanical Engineering at the University of Delaware. My research focuses on multiscale modeling approaches of highly textured fibers to predict their effective force response during microdroplet testing.

I would like your permission to use (SEM) figures from your dissertation that show the fiber topography in my dissertation defense. I will not use your figures in any journal manuscripts that I may submit.

May I have your permission to use the SEM figures from your Ph.D. dissertation listed below?

"Tailored Interphase Structure for Improved Strength and Energy Absorption of Composites," Xiao Gao, Spring 2006, University of Delaware, Department of Materials Science. Copyright 2006 Xiao Gao.

Thank you for your time. I look forward to your response.

Sincerely,
Mike Minnicino

xgaocomposite@gmail.com <xgaocomposite@gmail.com> Mon, Jun 22, 2015 at 3:00 PM
To: Michael Minnicino <minnicino@gmail.com>

Hi Mike,
You are welcome to use the SEM images from my dissertation and good luck with your study.
Have a great day!
Xiao

Sent from my iPhone
[Quoted text hidden]